Charge Distributions in Poly(ethylene oxide)-Based Solid Polymer Electrolytes for Lithium-Ion Batteries

Dissertation
zur Erlangung des Grades
des Doktors der Ingenieurwissenschaften
der Naturwissenschaftlich-Technischen Fakultät
der Universität des Saarlandes

von
Kapil Faliya

Saarbrücken
2022

Tag des Kolloquiums: 11. November 2022

Dekan: Prof. Dr. Ludger Santen

Berichterstatter: Prof. Dr.-Ing. Herbert Kliem
                  Prof. Dr. Carlos J.M.M. Dias

Akad. Mitarbeiter: Dr. Sukhvinder Singh

Vorsitz: Prof. Dr.-Ing. Georg Frey

Discoveries and Innovations are fruits of the tree called Curiosity

. . .

Acknowledgment

Completing this PhD thesis would not have been possible without the constant support from my family, friends, supervisor and colleagues. On this occasion, I would like to take the opportunity to express my gratitude and appreciation to all these people.

First of all, I would like to thank my supervisor Prof. Dr. -Ing. habil. Herbert Kliem. Without his constant and dedicated guidance, encouragement, help, inspiration and advice, this PhD study would not have been possible. I am very thankful to him for having taught me the principles of science.

I would also like to thank Prof. Calos Jorge Mariano Mirada Dias from Departamento de Ciencias dos Materials, Universidade Nova de Lisboa. Without his support and guidance, a smoothing-derivative algorithm developed and used in this phd study would not be possible.

I am also very thankful to my colleagues: Christian Peter, Dr. Laxman Kankate, Sujit Varakantam and Dr. Andreas Leschhorn who became very good friends during my PhD journey. They have shared with me their knowledge during our discussions and helped me with my experimental work and publications.

I would like to recognize the invaluable assistance that my friends Milena Fichtner, Jasmin Schlehofer, Nadine Schlehofer and Claire-Emeraude Filtz provided to improve the writing of this PhD thesis from the linguistic point of view.

At this occasion, I would like to say that I am very grateful to my dear elder brother Pavan Faliya for everything he has done for me. Without his effort and support, I would not have been able to pursue my studies, career and life in Germany.

I also want to thank my good and closest friend Marie-Christin Lindecke for her support during this time. Her kindness helps me to stay positive during stress and difficult times.

At this moment, it would be unthinkable not to mention Fini, a closest person to me, for our mindful conversations from time to time. I am thankful for that.

Above all, I can not express in words how grateful I am for the constant love and support from my mom and dad.

Abstract

An increasing demand of using electricity in households and in industries as well as for electric transportation motivates the development of economical, efficient and safe energy storage devices. In the category of energy storage devices, the lithium-ion battery (LIB) is the most commonly in use these days. This battery is not 100% safe to use. For example, a liquid electrolyte used in LIB raises safety issues such as leakage and combustibility. For this reason, solid polymer electrolytes (SPEs) are a possible replacement in order to overcome the safety issues related to the use of liquid electrolytes. At present, the conductivity of SPEs is not high enough to use SPEs in LIBs as an electrolyte. To improve the conductivity of this class of electrolytes, we need to study the ion/charge conduction mechanism of this material in detail. In order to understand the conduction mechanism, we need to have a closer look at the transient formation and movement of charges inside SPEs under given biased and unbiased conditions. In this regard, to facilitate the understanding of the charge formation and movement, the Kelvin probe force microscopy (KPFM) together with a reliable statistical data analysis approach has been used. As poly(ethylene oxide) (PEO) is a material used as an electrolyte in LIBs, the PEO and its salt compound with lithium perchlorate ($LiClO_4$) were investigated with this approach. An aluminum-poly (ethylene oxide)-aluminum (Al-PEO-Al) sample structure is used as a model system. Our approach for the investigation works as follows: First, the surface potential between the electrodes is measured by the KPFM under biased and unbiased conditions. Then the measured surface potential is differentiated twice by a reliable statistical smoothing-derivative algorithm with additional feedback loops. This is done in order to extract the space charge distribution according to the Poisson equation. In this study, the surface potential was measured before application of an external voltage, during application of the external voltage and after switching off the external voltage. In these three different experimental situations, the charge distributions were extracted from the measured surface potential data. In this way, the transient formation and movement of internal potential and simultaneously internal charges were investigated before, during and after switching off the external voltage. During this study, we have also used our experimental approach to investigate the PEO samples embedded with micro/nano size metal particles (i.e. Cu) to check the effect of metal particles on the formation and movement of charges inside the PEO. Our experimental method together with the statistical data analysis approach facilitates an investigation of the behavior of a zero field point inside the PEO sample. The information of the zero field point is extracted from the electric field distribution inside the PEO. The electric field distribution is calculated from the measured surface potential data according to the Poisson equation.

Zusammenfassung

Der steigende Bedarf elektrischer Energie in Haushalten, Industrie und im Transport motiviert zur Entwicklung wirtschaftlicher, effizienter und sicherer Energiespeicher. Die Lithum-Ionen-Batterie (LIB) ist heute der am häufigsten verwendete elektrische Energiespeicher. Diese Batterie birgt Gefahren. Der flüssige Elektrolyt, der in LIB's verwendet wird, kann auslaufen und sich entzünden. Eine Lösung dieses Sicherheitsproblems wäre die Verwendung von Festkörperelektrolyten. Gegenwärtig ist die Leitfähigkeit von Festkörperelektrolyten dafür nicht groß genug. Um die Leitfähigkeit dieser Klasse von Elektrolyten zu untersuchen wird der Ionen-/Ladungstransport im Detail untersucht. Die Leitfähigkeit dieser Klasse von Elektrolyten wird vor allem durch Ionenleitung bestimmt. Um den zugrundeliegenden Leitungsmechanismus genauer zu verstehen, wird die transiente Bildung und Bewegung von Ladungen innerhalb des Festkörperelektrolyten unter gegebenen elektrisch vorgespannten und unvorgespannten Bedingungen genauer untersucht. Eine Kelvinsonde (Rasterkraft-Mikroskopie) zusammen mit einer zuverlässigen Methode zur statistischen Datenanalyse bilden die Kernelemente der in dieser Arbeit verwendeten Untersuchungsmethode. Als Modellsystem wird eine Aluminium-Polyethylenoxid-Aluminium (Al-PEO-Al) Probenstruktur verwendet. PEO ist hier der zu untersuchende Elektrolyt. Zuerst wird reines PEO im Modellsystem verwendet, dann wird in einem weiteren Versuch dem PEO das Salz Lithiumperchlorat (LiClO4) hinzugefügt (Stichwort: LiClO4 doping). Die zur Untersuchung verwendete Methode funktioniert wie folgt: Zunächst wird das Oberflächenpotential zwischen den Elektroden mit der Kelvinsonde unter vorgespannten und unvorgespannten Bedingungen gemessen. Dann wird das gemessene Oberflächenpotential durch einen statistisch zuverlässigen iterativ optimierenden "Smoothing Derivative Algorithmus" zweimal differenziert und damit die Raumladungsverteilung aus der Poisson-Gleichung berechnet. Das Oberflächenpotential wird vor, während und nach dem Abschalten der externen Spannung gemessen und die jeweilige Ladungsverteilung aus den gemessenen Oberflächenpotentialdaten bestimmt. Auf diese Weise wird gleichzeitig die transiente Bildung und Bewegung des inneren Potentials und die transiente Bildung und Bewegung interner Ladungen vor dem Anlegen einer externen Spannung, während des Anlegens der externen Spannung und nach dem Abschalten der externen Spannung untersucht. Außerdem wurde der Einfluss von Kupferpartikeln mit Größe im Mikro-/Nanometer Bereich, die in PEO eingebettet sind, auf die Bildung und Bewegung von Ladungen innerhalb des PEO untersucht. Die verwendete experimentelle Methode zusammen mit der statistischen Datenanalyse ermöglichen eine Untersuchung des Verhaltens des Feldnullpunktes innerhalb der PEO-Probe. Der Feldnullpunkt wird aus der elektrischen Feldverteilung im PEO bestimmt.

Table of Contents

List of Figures

List of Tables

List of Abbreviations

LIB   Lithium-Ion Battery
SPE   Solid Polymer Electrolyte
PEO   Poly(Ethylene Oxide)
VTF   Vogel-Tamman-Fulcher
CSPE   Composite Polymer Electroyte
KPFM   Kelvin Probe Force Microscopy
AFM   Atomic Force Microscope
PEG   Polyethylene Glycol
FEM   Finite Element Method
SG   Savitzky-Golay
DPW   Data Point Window
DOP   Degree of Polynomial

Chapter 1

Introduction

During the last years, not only the production and distribution of electrical energy, but also its storage achieved increasing importance. For example, alternative energy sources, i.e. solar energy, wind power etc., need economical and high-efficient electricity storage systems because these sources have an ability to generate electricity only on an intermittent basis. In order to use electricity efficiently, the development of low-cost, safe and highly efficient energy storage devices is a very attractive subject for research nowadays. A frequently used energy storage device in our regular life is the lithium-ion battery (LIB).

The foundation of the lithium-ion battery was laid during the oil crisis in $1970s$ [1]. Stanley Whittingham was the first person who had developed the lithium-ion battery in 1976 [2]. He had invented a cathode from lithium disulphide which can intercalate lithium ions. As an anode he had used metallic lithium. His lithium-ion battery had a potential over $2V$, but as the metallic lithium is very reactive, the battery can easily catch fire. For this reason, it was not feasible to use this chemistry for practical purposes. In 1980, J. B. Goodenough and his colleagues came up with a new cathode material. J. B. Goodenough had suggested to use a metal oxide instead of a metal sulphide. He had used cobalt oxide as a cathode and metallic lithium as an anode [3]. His version of the lithium-ion battery had a potential over $4V$, but the problem of the safety was still unsolved. Five years later, in 1985, Akira Yoshino created the first prototype of a commercially feasible lithium-ion battery [4]. He used cobalt oxide as a cathode, but instead of metallic lithium as an anode, he used a carbon material which can also intercalate lithium ions like the cathode material. Based on this material combination, Sony and Asai Kasei Corporation released the first commercial lithium-ion battery in 1991. Since then, the lithium-ion batteries have revolutionized our lives. For this innovation, Stanley Whittingham, J. B. Goodenough and Akira Yoshino were awarded the novel prize in chemistry in 2019 [1].

One of the most critical components in the development of safe and efficient LIBs is the electrolyte separating the electrodes. As most of the LIBs have a liquid electrolyte, they are suffering from safety issues such as leakage, flammability and stability. Consequently, solid polymer electrolytes (SPEs) gained much attention for the development of the safe, flexible and more efficient LIBs [5, 6]. As of now, the understanding of this new class of electrolytes is not complete. In this PhD study, we have tried to reveal some characteristics of SPEs.

1.1 Research objective of this Phd study

After the investigation of the ionic conductivity of poly(ethylene oxide) (PEO) by P. V. Wright [7], M. Armand has suggested the possible use of PEO in the development of electrochemical devices [8]. As PEO shows a very good compatibility with lithium salts, it can serve as an solid state electrolyte for LIBs.

The development of high performance batteries requires a good understanding of this novel electrolyte. Several theories have been developed to describe the ion transport mechanism in SPEs. For long time, it has been considered that the ion transport in SPEs was due to the existence of an amorphous phase in the polymeric host. It was thought that a high ionic conduction can be achieved if there is a high amount of an amorphous phase in the material [9]. But Gadjourava and his co-workers have investigated experimentally and concluded that the crystalline polymer host can also support high ion conduction in SPEs [10]. The phenomenon of ion transport in crystalline and amorphous PEO is a current research topic because the understanding of it at the present time makes it difficult to optimize the ion transport without affecting other critical parameters.

In the past, some efforts have been made to understand the phenomenon of ion transportation in SPEs. The studies of temperature dependent conductivity show that polymer electrolytes exhibit two types of conduction mechanisms [11]. One is the Vogel-Tamman-Fulcher (VTF) type and the other is the Arrhenius type. The VTF type relationship between conductivity and temperature is expressed by the following equation

$$\sigma = A \cdot T^{-\frac{1}{2}} \cdot exp \left[\frac{-B}{(T - T_0)} \right] \tag{1.1}$$

and the Arrhenius type relationship is expressed by the following equation

$$\sigma = A \cdot exp \left[\frac{-E_a}{kT} \right] \tag{1.2}$$

Where, A is is the pre-exponential factor, E_a is the activation energy, k is the Boltzmann constant and B and T_0 are fitting parameters. Sometimes T_0 is identified as an equilibrium glass transition temperature. T_0 is thought of as a glass transition temperature that would occur if a cooling rate is infinitesimally small. It is related to the measured glass transition temperature T_g roughly by $T_0 \cong T_g - 50K$ [11].

The VTF type indicates a conductivity mechanism involving ionic hopping motion coupled with the relaxation/breathing and/or segmental motion of polymeric chains. The Arrhenius type indicates an ion transport through a simple hopping mechanism decoupled from the polymer-chain motion [12].

My colleagues have also proposed a three dimensional hopping model [13, 14]. In this model, single charges experience the externally applied electric field, the Coulomb fields bet-

ween the carriers and the fields between the charges in the electrolyte and the image charges in the electrodes. Charges attracted to the electrodes form with their image charges dipoles at the interface. Their fields repel further movable charges into the volume of the sample. Therefore, behind the charge layers at the electrodes a depletion zone builds up [14, 15]. This cannot be described by the continuum models [16, 17] because the role of the image charges is neglected therein. With the help of the three dimensional hopping model, the charge distribution in the electrolyte can be calculated and compared to the experimentally detected one.

So far the three dimensional model can explain some electrical and ion-transport properties of the metal/solid electrolyte/metal system [13, 14, 18, 19, 20, 21, 22, 23, 24]. However, some new phenomena related to the ion-transport in solid polymer electrolytes have been detected with a new investigating approach developed during this PhD study.

Normally, the ion-transport property is mostly characterized by considering some basic ionic parameters such as ionic conductivity, ionic mobility, mobile ion concentration, ionic drift velocity, ionic transference number etc. [12]. The conductivity is generally measured by using the impedance spectroscopy (IS) technique. The ionic mobility can be determined by using the dc polarization transient ionic current (TIC) technique [25]. The ionic transference number can be determined by using combined dc polarization and ac impedance measurements [26]. Mobile ion concentration and ionic drift velocity are generally evaluated by substituting the data obtained in the above measurements into the appropriate equations.

But none of the above mentioned measurement techniques give a clear visualization of the charge distribution inside SPEs for a better understanding of the ion-transport mechanism. This is the main reason which motivates us to look for another technique to understand charge distribution and transportation inside SPEs. For this reason, in this study, we have presented a new approach to understand the charge distribution and transport inside the volume of PEO and its salt compound under biased and unbiased conditions.

This approach is also used to see the behaviour of charge distribution in a new group of SPEs called composite polymer electrolytes (CSPEs). CSPEs are SPEs with dispersed nano/micro-sized filler particles of conducting and/or non-conducting materials [12]. It is expected that CSPEs contribute to the realization of lithium battery systems with improved safety, energy density and design flexibility. The major problem preventing the successful operation of lithium polymer batteries is the reactivity at the Li/Li+ interface and growth of a passivation layer at the Li metal surface causing an increase in the internal resistance. This could be prevented if highly stable and highly conducting SPEs are materialized. Some new investigations show that the materialized CSPEs provide not only improved electrode electrolyte compatibility but also an enhancement in morphological, electrochemical, mechanical and electrical properties as compared to conventional/gel/plasticized polymer electrolytes [27, 28, 29, 30, 31, 32]. However, it is still a mystery which role the filler particles play in promoting the ion transport. For this reason, it is worth to look at the charge distribution of CSPEs under both biased and unbiased conditions.

The approach presented in this study to investigate the charge distribution is also applied to check the theory presented by Joseph Lindmayer in 1964. In his article 'Current Transients in Insulators', he has presented his study on charge trapping and release processes in insulating materials [33]. Normally, materials, which are solid, do not have a perfect crystal structure.

There are always some trap sites. These trap sites are filled with charge carriers in thermal equilibrium and when current flows through this material, more charge carriers will be trapped on these sites. Lindmayer had given a model based on a zero field point for discharge of charge carriers from trap sites . With our proposed approach, we have investigated this model.

1.2   A proposed approach for the investigation

Our approach for the investigation is based on the Kelvin probe force microscopy (KPFM) together with a statistical analysis of noisy experimental data. As the KPFM measures the surface potential of the sample, the electric field and the charge distribution can be calculated by using the Poisson equation from the surface potential data under both biased and unbiased conditions. At the present time, only few studies are documented for extracting the electric field and the charge distribution from the surface potential measured by the KPFM [34, 35, 36]. But in these studies, the problem arisen by the noise in the surface potentail data is not taken into consideration. In our study, we have addressed the noise problem in detail.

Our approach is divided mainly into four different parts: sample preparation, measurements of the surface potential by the KPFM, an extraction of the information about the electric field and charges from the surface potentials and an analysis of results. For each part, a separate chapter is dedicated in this PhD dissertation. Before understanding the approach in detail, some background and basic information about the surface potential and its measurement is described in Chapter 2. Chapter 3 gives detailed information about the sample structure and its preparation process. The KPFM measurement technique is described in Chapter 4. Chapter 5 tells about the development of a smoothing-derivative algorithm based on a statistical method called the F-test. This algorithm is necessary to deal with noisy data of the surface potential and to extract the information about the electric field and charges in the material. The analysis of all the results and its explanations are described in Chapter 6, 7 and 8. At the end, the summary, consisting of the conclusion of this study and suggestions for future research, is given in Chapter 9.

Fig. 1.1 shows the blue print of the proposed approach for electric field and charge investigation. Step 1 in Fig. 1.1 shows a final sample structure at the end of the process of the sample preparation. This sample structure was used during the investigation. Step 2 in Fig. 1.1 gives an idea about how a surface potential profile in biased and in unbiased conditions looks like. Step 3 shows the process how the smoothing-derivative algorithm deals with the noisy surface potential data and gives the information about a charge distribution. Lastly, Step 4 is the result analysis.
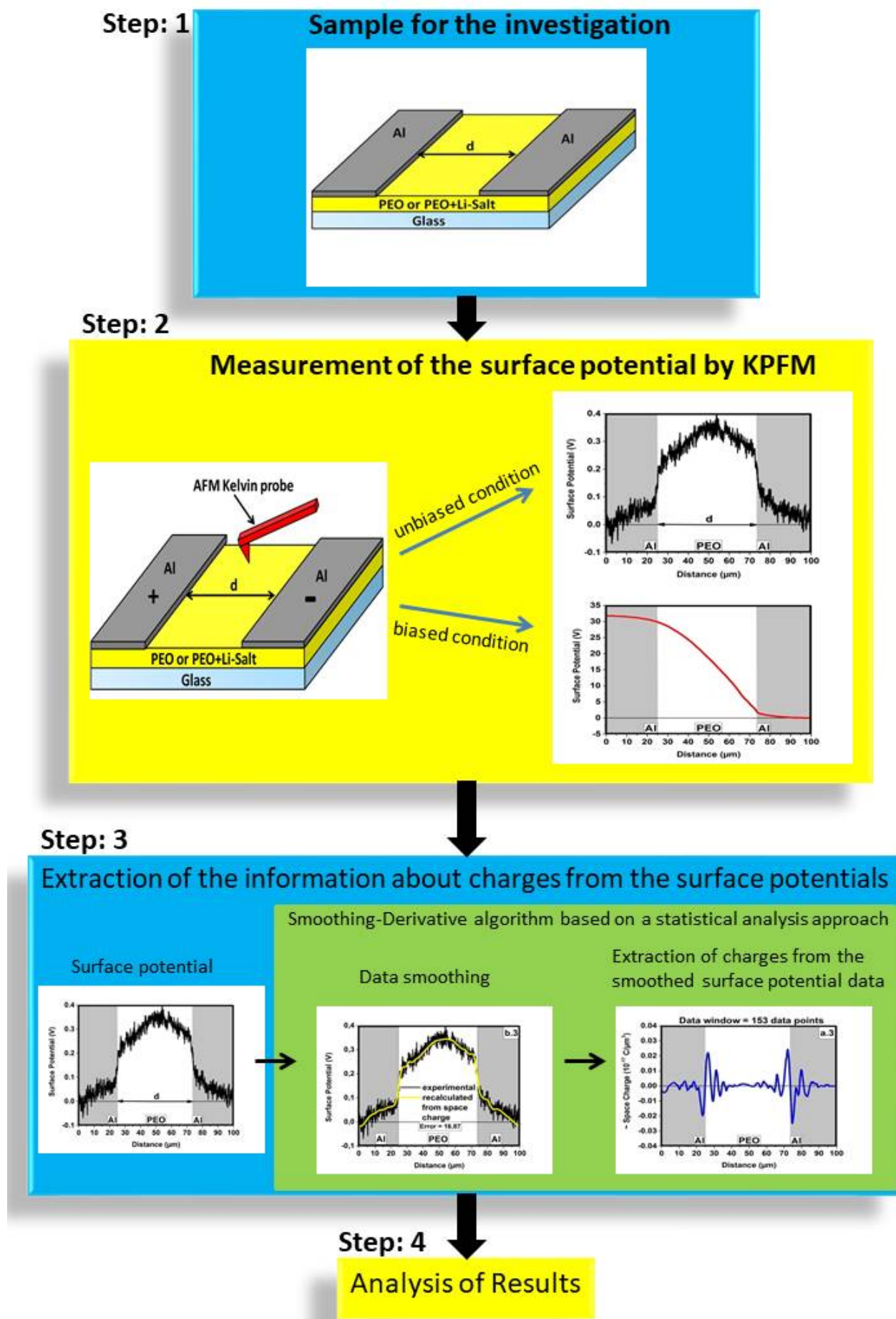
Figure 1.1: The appraoch for the investigation.

Chapter 2

Theoretical background

2.1 Kelvin probe force microscopy (KPFM)

Kelvin probe force microscopy (KPFM) is operated by an atomic force microscope (AFM) system. The KPFM measures a local contact potential difference between a conductive cantilever tip and a sample directly underneath the cantilever tip. In another word, by the KPFM, we can do mapping of a work function or a surface potential of the sample at a high spatial resolution. That's why, the KPFM is also called surface potential microscopy. The KPFM is generally used to characterize electrical properties of metals and semiconductor materials at an atomic-scale or at a nano-scale level [37]. The electrical properties of organic [38, 39, 40] and biological [41, 42] materials have also been investigated by the KPFM.

2.1.1 Background

In 1898, Sir William Thomson, later known as Lord Kelvin made an experiment. In that experiment, he detected using a gold-leaf electroscope that charges are created on parallel plates of copper and zinc when they are brought into electrical contact and then moved apart [43]. The apparatus used by Kelvin are shown in Fig. 2.1. We can explain, what Kelvin observed in his experiment, by work function differences of materials. The work function (φ) is defined as the minimum energy measured in eV which we need to remove an electron from a solid to outside of the solid surface. In another word, we can say that the work function (φ) is an energy needed to move an electron from the Fermi energy level (E_f) into the vacuum level (E_v). The energy diagram explaining Kelvin's observation is shown in Fig. 2.2. When two different solid materials in the form of a parallel plate capacitor are connected electrically by means an electric wire (see Fig. 2.2(B)), then electrons (red balls in Fig. 2.2(B)) will flow from the material with lower work function (φ_2) to the one with higher work function (φ_1) in order to equalizing the Fermi energy levels $(E_{f1}$ and $E_{f2})$ of the materials. During this process, equal and opposite charges are induced on the parallel plate capacitor. An electric field is generated because of these charges. From this electric field, the potential is developed between the two plates. The potential developed between these two plates is denoted as the surface potential (ϕ) or the contact potential or the contact potential difference (CPD). In short, the surface potential is nothing but the work function difference between the two materials: $\phi = \varphi_1 - \varphi_2$. In principle we can measure the surface potential (ϕ) by applying an external DC voltage (V_{DC}) to the parallel plate capacitor but in the opposite direction of the surface potential until the charges on the surface of the materials disappear (see Fig. 2.2(C)). At this point the applied external voltage and the surface potential are equal : $V_{DC} = \phi$.
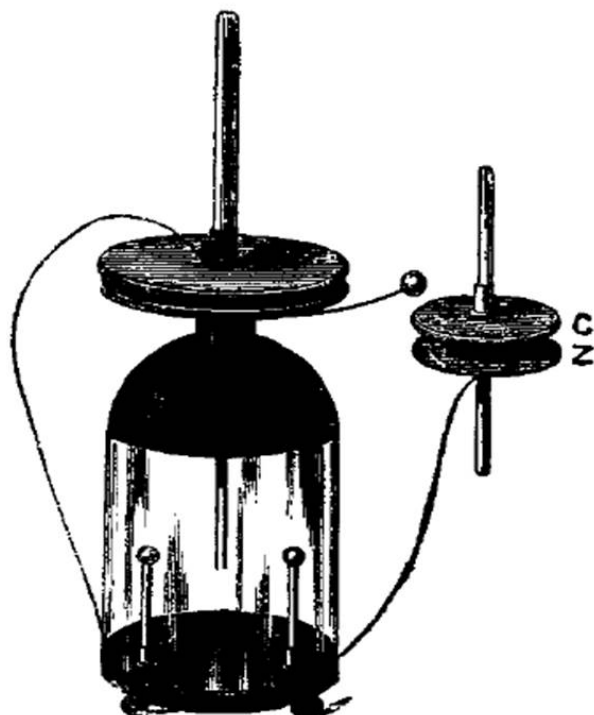
Figure 2.1: Set up of Kelvin's experiment.

W. A. Zisman was the first person who came up with a method to measure the surface potential or the contact potential difference of materials. In 1932, he had published an article to describe his concept known as "nulling concept" [44]. In this method, two different metal plates are placed opposite to each other forming a parallel plate capacitor. One of the plates is vibrating over another plate. This causes a capacitance to vary as the distance between two plates changes. This varying capacitance induces charge to flow which gives rise to an AC current. Now, an external voltage is applied between two plates, until the AC current reduces to its minimum or ideally zero ("null"). At this point, the external voltage is equal, but in opposite direction to the surface potential of the two metals.

M. Nonnenmacher and his colleagues [45] were the first who used the AFM system to measure the surface potential. They embraced the nulling concept of Zisman. The main idea of their concept is as follows: The cantilever tip and the sample underneath the tip form a capacitor. As they are connected electrically, the opposite charges will be induced on the tip and on the sample because of the work function difference between the tip and the sample. These charges disappear when the electric force between the tip and the sample is zero. For this reason, Nonnenmacher named this technique Kelvin probe force microscopy.

2.1.2   Basic principle of KPFM

As mentioned earlier, Nonnenmacher has used the concept of nullifying the electrical force between the tip and the sample in order to measure the surface potential. A good way to understand this concept is to start with the energy in a parallel plate capacitor. The equation of this
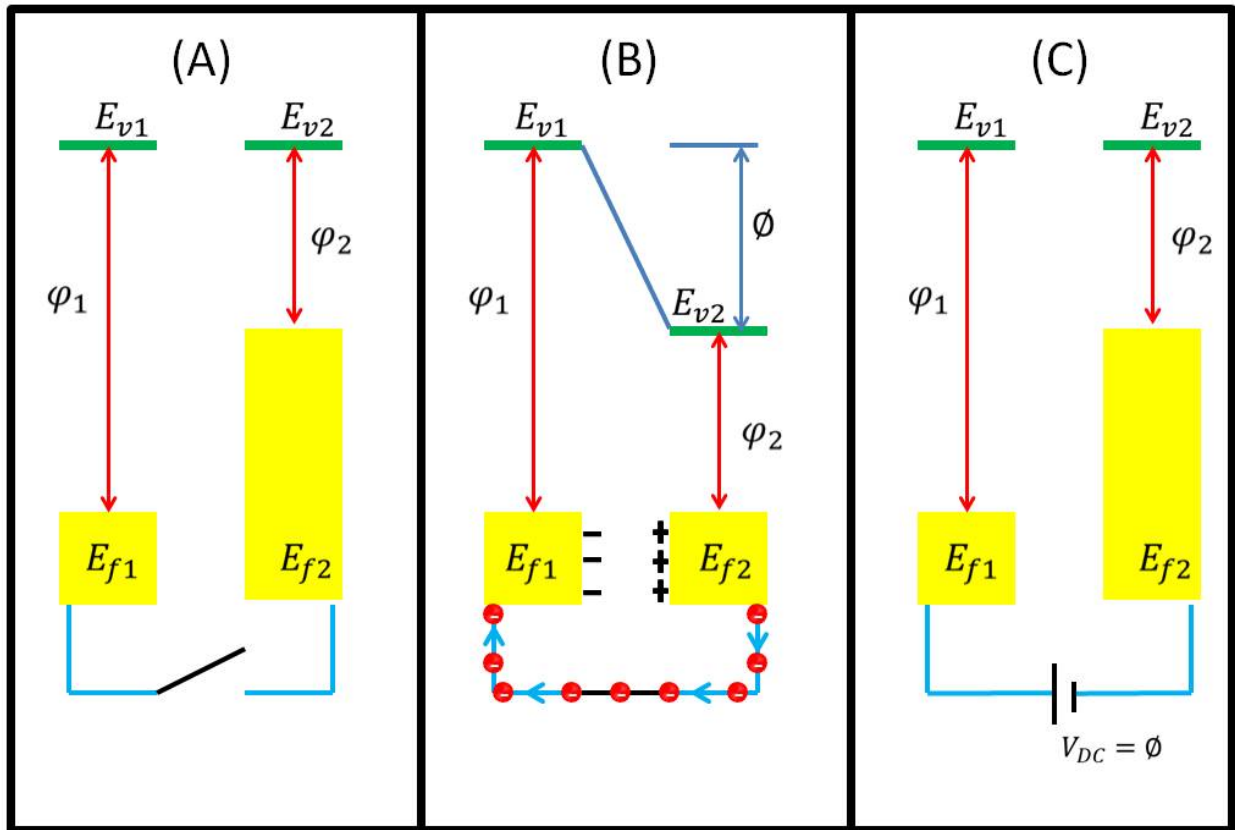
Figure 2.2: Energy diagram illustrating Kelvin's observation.

energy is as follows.

$$U = \frac{1}{2}C(\Delta V^2)$$

(2.1)

Here, the tip and the sample form a parallel plate capacitor. That is why, C is the local capacitance between the tip and the sample. ΔV is the voltage difference between these two.

The electric force F acting between the tip and the sample is calculated as follows: the electric force between the tip and the sample is the rate of change of the energy with the distance separating them.

$$F = -\frac{dU}{dz}$$

(2.2)

Now, substituting Equation 2.1 into Equation 2.2.

$$F = -\frac{1}{2}\frac{dC}{dz}(\Delta V^2)$$

(2.3)

Where, z is the direction normal to the sample surface and $\dfrac{dC}{dz}$ is the gradient of the capacitance between the tip and the sample surface.

During the surface potential measurement, an AC voltage $V_{AC}sin(\omega t)$ and a DC voltage V_{DC} are applied to the AFM tip. Here, ω is the resonant frequency of the cantilever. The AC voltage generates an oscillating electrical force between the tip and the sample. If there is a work function difference (surface potential (ϕ)) between the tip and the sample, there will be an extra oscillating electric force on the tip and the sample due to the surface potential. The amplitude of this extra electrical force can be detected. By applying a DC voltage V_{DC} equal in magnitude but in opposite direction to the surface potential, this extra oscillating electric force generated by the surface potential can be nullified.

ΔV in Equation 2.3 is consist of voltages V_{tip} and ϕ.

$$\Delta V = V_{tip} \pm \phi \tag{2.4}$$

and

$$V_{tip} = V_{AC}sin(\omega t) + V_{DC} \tag{2.5}$$

Substituting Equation 2.5 into Equation 2.4.

$$\Delta V = V_{AC}sin(\omega t) + V_{DC} \pm \phi \tag{2.6}$$

Note that, $\pm$ sign depends in which direction the bias V_{DC} is applied in order to nullify the surface potential (ϕ).

Now, by substituting Equation 2.6 into Equation 2.3, we get the following equation for the electrical force acting between the tip and the sample.

$$F = -\frac{1}{2}\frac{dC}{dz}(V_{AC}sin(\omega t) + V_{DC} \pm \phi)^2 \tag{2.7}$$

To simplify Equation 2.7 further, we need to use the relation $2sin^2x = 1 - cos(2x)$. The equation of the force will be rearranged as follows.

$$F = -\frac{1}{2}\frac{dC}{dz}\left[(V_{DC} \pm \phi)^2 + \frac{1}{2}V_{AC}^2\right] - \frac{dC}{dz}(V_{DC} \pm \phi)(V_{AC}sin(\omega t) + \frac{1}{4}\frac{dC}{dz}V_{AC}^2cos(2\omega t) \quad (2.8)$$

The above force can be divided into three different parts $F_{DC\,term}$, $F_{\omega\,term}$ and $F_{2\omega\,term}$.

$$F = F_{DC\,term} + F_{\omega\,term} + F_{2\omega\,term} \quad (2.9)$$

where,

$$F_{DC\,term} = -\frac{1}{2}\frac{dC}{dz}\left[(V_{DC} \pm \phi)^2 + \frac{1}{2}V_{AC}^2\right] \quad (2.10)$$

$$F_{\omega\,term} = -\frac{dC}{dz}(V_{DC} \pm \phi)(V_{AC}sin(\omega t) \quad (2.11)$$

$$F_{2\omega\,term} = \frac{1}{4}\frac{dC}{dz}V_{AC}^2cos(2\omega t) \quad (2.12)$$

The cantilever responds only to forces which are at or very near to the cantilever resonance. Because of this reason, the forces $F_{DC\,term}$ and $F_{2\omega\,term}$ do not have any significant influence on the oscillation of the cantilever [46]. Therefore, we can take only $F_{\omega\,term}$ into account to find out the surface potential (ϕ).

To find out the surface potential (ϕ), we need to make the force $F_{\omega\,term}$ equal to zero ($F_{\omega\,term} = 0$). In order to do that, the goal of the feedback loop of the AFM system is to adjust the voltage V_{DC}, until $V_{DC} \pm \phi$ equals zero ($V_{DC} \pm \phi = 0$). In other words, the AFM system adjusts the voltage V_{DC}, until it equals to the surface potential (ϕ) of the sample. At that point, the force $F_{\omega\,term}$ between the tip and the sample is equal to zero. In this way, the surface potential of different materials can be measured with the help of the Kelvin probe force microscopy (KPFM).

Chapter 3

Sample preparation

3.1 Poly(ethylene oxide) (PEO) as an investigated material: Why?

There are two main basic components which are needed for the development of any SPEs for LIBs. The first is a polymer matrix and the second is a lithium salt. One thing, we have to mention here, is that when a lithium salt is desolved in a polymer matrix, not all of the lithium salt is able to separate and give freely movable ions in the polymer matrix. That is why, the solubility of lithium salts in the polymer matrix is a very important parameter because it is one of the parameters which determines the conductivity of SPEs. For this reason, poly(ethylene oxide) (PEO) is the most desirable candidate among other polymers because it shows a very good solubility for lithium salts.
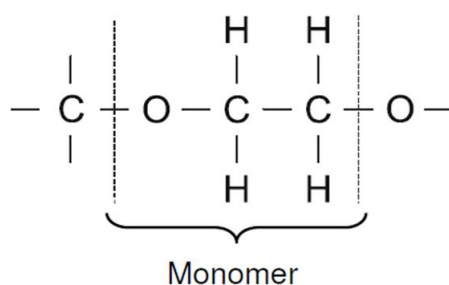
Figure 3.1: Monomer of poly(ethylene oxide).

PEO is the polymer which has a molecular weight above $20000 gmol^{-1}$ and it is a compound of polyether. The chemical structure is presented in Fig. 3.1. The PEO is also named polyethylene glycol (PEG). It depends on the molecular weight of the PEO. When the molecular weight of the PEO is less than $20000 gmol^{-1}$, then it is called the PEG. The PEO consists of

the sequential oxyethylene group: $-CH_2 - CH_2 - O-$ and the polar groups:$-O-, -OH-$ in the polymer chains. Becasue of this, the PEO shows a very good ability to dissolve the ionic salts [47].

3.2   Steps for the sample preparation

For this study, a commercially available pure PEO (from SIGMA-AIDRCH) and lithium perchlorate ($LiClO_4$) (from JANSSEN) in a powder form were purchased. The steps for the sample preparation are shown in Fig. 3.2.

In step 1, two types of aqueous solutions are prepared initially. One is only with pure PEO and another one is PEO doped with $0.1wt\%$ $LiClO_4$. After that, in step 2, approximately $1\mu m$ thick films from the solution of pure PEO and the solution of PEO doped with Li-salt are prepared on a highly resistive glass substrate by using a spin coating technique. Then in step 3, the sample is put into an oven at 60^oC for about $30min$ in order to achieve an adequate drying of the sample. In the last step, aluminum (Al) electrodes of approximately $80nm$ thickness are evaporated through a shadow mask on the top of the PEO by using a vacuum-thermal-evaporation technique.

With this procedure, two types of sample structures are prepared as shown in Fig. 3.3. The sample with the type 1 structure (see Fig. 3.3(a)) has a typical gap of a width d of about $50\mu m$ between two Al electrodes. The optical image (a top view) of the type 1 sample is shown in the top left corner of Fig. 3.3(a). The sample with the type 2 structure (see Fig. 3.3(b)) has varying distance between two electrodes. The optical image (a top view) of the type 2 sample is also shwon in the top left corner of Fig. 3.3(b). This type of samples is prepared in order to investigate the effect of the distance between two electrodes on the charge distribution in PEO. The two parallel vertical red lines in the optical images indicate how the distance between the two electrodes varies (Fig. 3.3(b)) or stays constant (Fig. 3.3(a)).
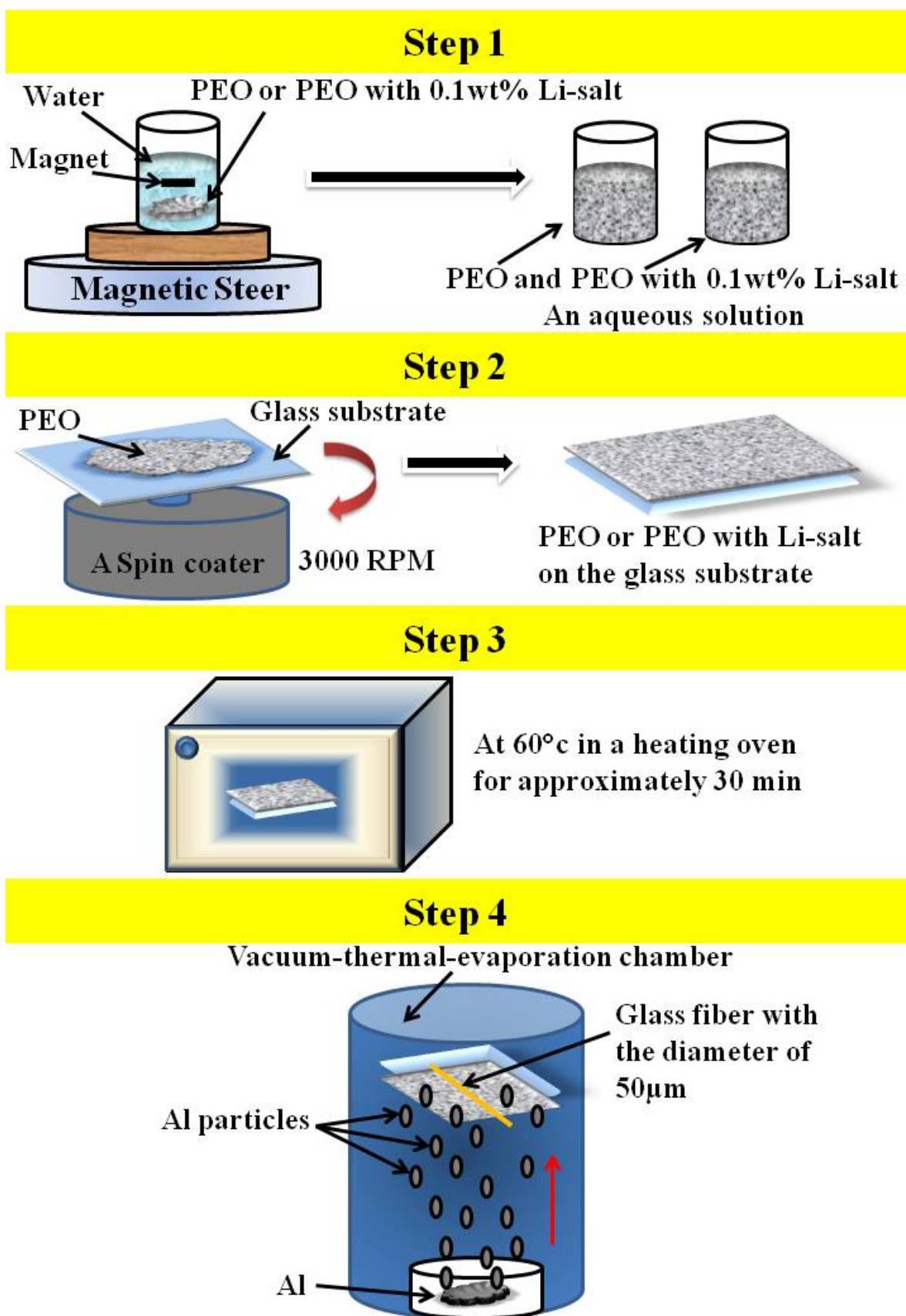
Figure 3.2: Steps for the sample preparation.
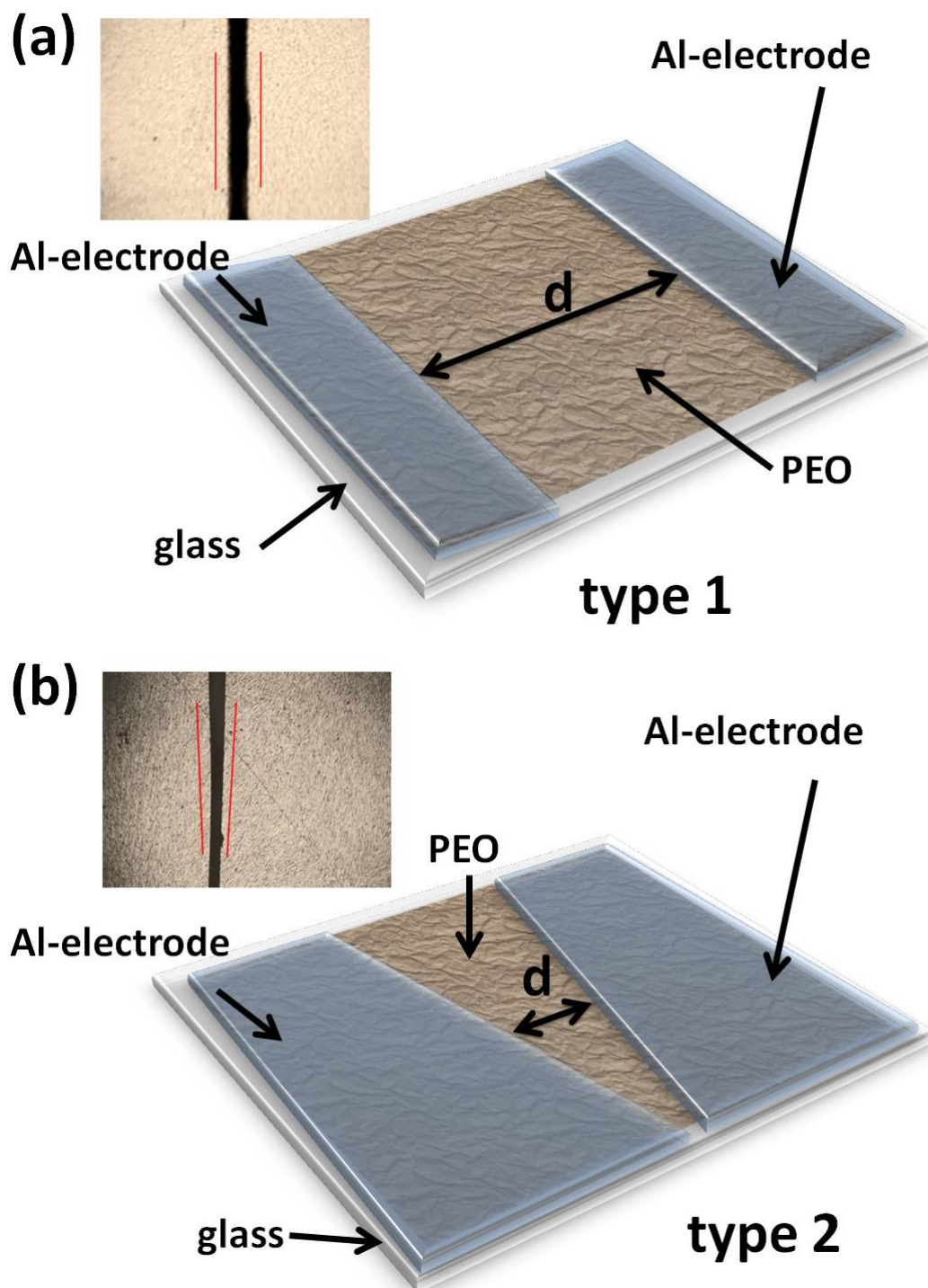
Figure 3.3: Sample structures.

Chapter 4

Surface potential measurement by the KPFM

The amplitude modulation (AM-KPFM) mode on a Veeco Innova $004 - 1005 - 000$ AFM set up is used for the surface potential measurement in this study. A tip with a conductive platinum-iridium (PtIr) coating (SCM-PIT from Bruker) is used.

4.1 Surface potential measurement steps

The surface potential is measured on the sample with the specific structure described in Chapter 3. To measure the surface potential along a line between two Al electrodes separated by distance d, the AM-KPFM works in two steps. A graphical representation of how the KPFM works to measure the surface potential, is depicted in Fig. 4.1. In the first step, the height profile of the sample surface is measured with a cantilever moving on the sample surface (see Fig. 4.1(A)). After that, the cantilever tip is lifted up to a specific lift height (see Fig. 4.1(B)). In this study, we have decided to use the lift height of $10nm$ in the measurements of the surface potential. However, the effect of different lift heights of the cantilever tip on the surface potential profile is investigated and described in section 4.3 in this chapter. In the second step, after lifting up the cantilever tip at a specific lift height, the surface potential is measured at that particular line where the height profile was previously determined in the first step (see Fig. 4.1(C)). In our experiment a single complete measurement, i.e. both the height profile measurement and the surface potential measurement, took 10s. A slowest scan rate of 0.1Hz was choosen purposefully because it gives enough time to the feedback system to respond appropriately to changes in height and surface potential in order to get a better resolution with a minimum noise level. Also, if the scan is too fast, the tip may crash into protrusions on the surface, possibly damaging the tip and/or sample. The concept of how the surface potential is measured, has been described in Chapter 2.

All surface potential measurements in this study have been conducted under a controlled dry environment of $5 - 8\%$ relative humidity. The environment, as dry as possible with the available experimental set-up, has been chosen to avoid the effect of the atmospheric water on the surface potential measurement and on the conductivity of the PEO. In the literature [48] it is reported that the surface potential on a silica surface had changed continuously with time at high relative humidity and no change had been observed at low humidity. It is checked that for our samples, the surface potential profile in the short-circuited condition shown in 4.4 does not change in time.
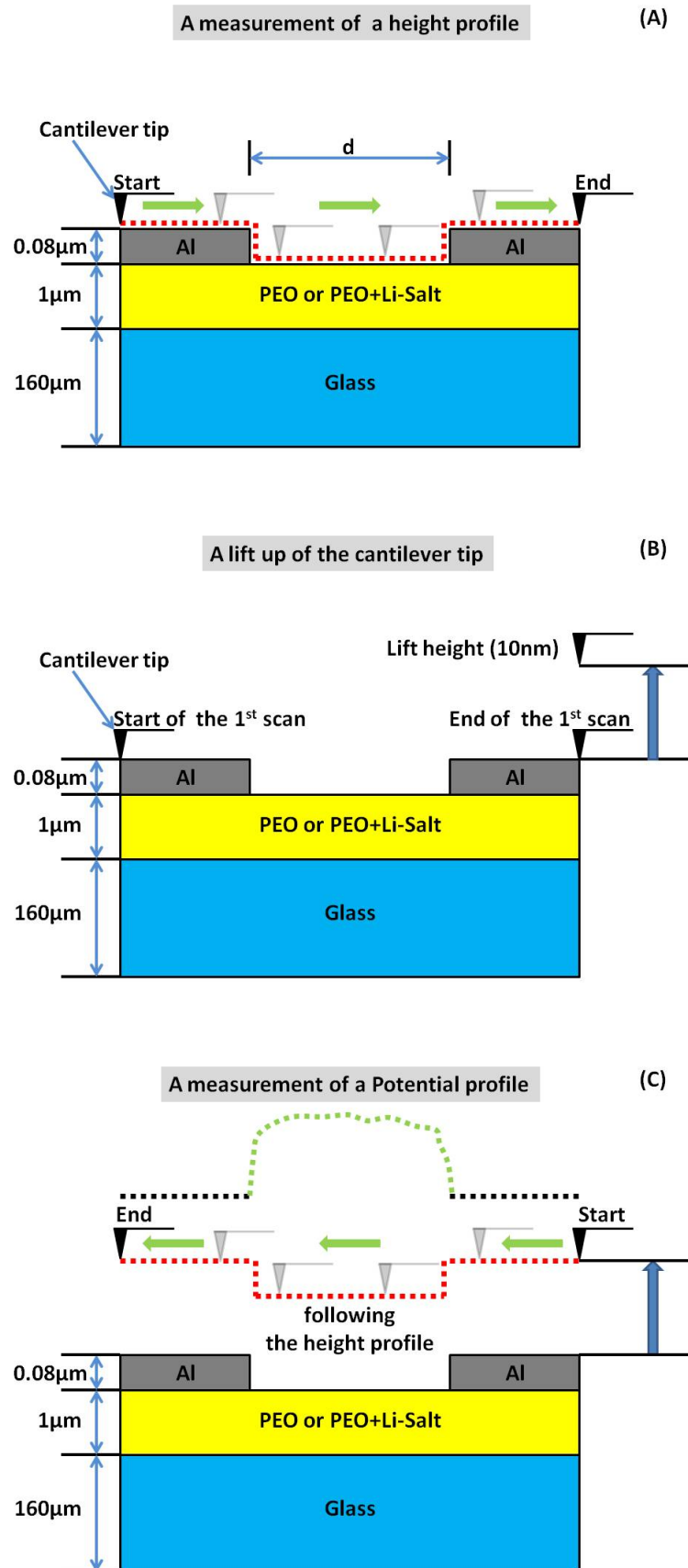
Figure 4.1: A measurement of a height profile (A), a lift up of the cantilever tip (B) and a measurement of a potential profile (C).

4.2 The influence of the topography on the potential profile

As the surface potential is measured by following the topography (the height profile (see Fig. 4.1(C))) of the sample, it is necessary to check the influence of the topography on the surface potential measurement. For this purpose, we have developed a sample with Al on a glass substrate by using a vacuum-thermal-evaporation technique. A layer of Al on the glass substrate has a step like structure shown in Fig. 4.2. As there is only one type of material on the glass substrate, we expect the surface potential to be the same everywhere regardless of the step on the layer of Al (see Fig. 4.2). The experimental results are shown in Fig. 4.3[49]. In this experiment, we have checked the influence of the height profile of the sample on the surface potential under both, biased and unbiased, conditions. Fig. 4.3(a) shows the surface topography of the sample and Fig. 4.3(b.1 and b.2) show the surface potential profile under the biased and unbiased conditions respectively. During the biased condition, we have applied an external voltage of $28V$ on the sample. It can be seen from Fig. 4.3 that the surface potential profiles under biased (Fig. 4.3(b.2)) and unbiased (Fig. 4.3(b.1)) conditions are not noticeably influenced by the surface topography. Moreover, as mentioned in the literature [50], a study presented by S. Sadewasser and his co-workers, reveals that the influence of the topography on the surface potential is quite small. Therefore, it is reasonable not to take the influence of the topography of the sample surface into consideration.
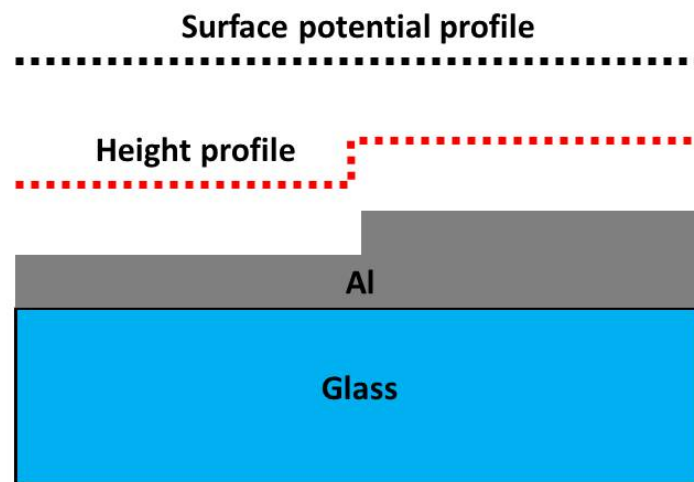
Figure 4.2: The step like structure of the layer of Al on the glass, the height profile (red), the surface potential profile (black).
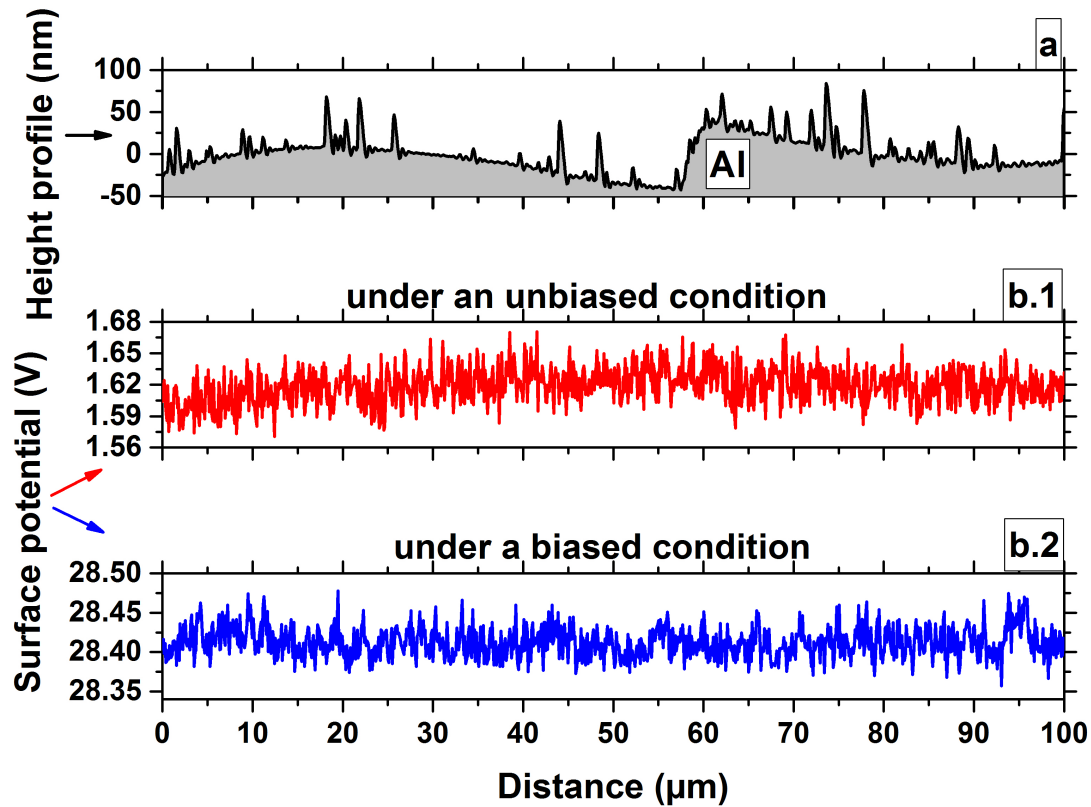
Figure 4.3: The height profile (a), surface potential under unbiased condition (red) (b.1) and surface potential under the biased condition (blue) (b.2).

4.3 The effect of the lift-height of the cantilever tip on the potential profile

In the Kelvin measurement, the tip-potential is adjusted to the surface potential of the sample underneath the cantilever tip. Therefore, there will be no electric field between the tip of the cantilever and the surface of the sample. Thus, one can neglect the influence of the tip on the charges in the sample. Nevertheless, at the same time, it is also necessary to understand the importance of the lift-height of the cantilever tip during the Kelvin measurement. Fig. 4.4 and Fig. 4.5 show the potential profiles with zero voltage applied and during application of $30V$ respectively. These profiles are measured on the undoped PEO sample with the type 1 sample structure. As it is clearly seen from the surface potential profiles shown in Fig. 4.4 and 4.5, there is a potential drop on the electrodes.

This potential tail depends on the lift height and can be derived as follows. Let us consider that we have stray fields from the left electrode during the applied external voltage or from surface charges in the PEO which end up perpendicular on the right electrode (Fig. 4.6) [49]. The equipotential lines are perpendicular to the field lines. At a height h, typically $h = 10nm$, the cantilever measures the potential. With α as an angle between electrode and an equipotential line we find the following equation.
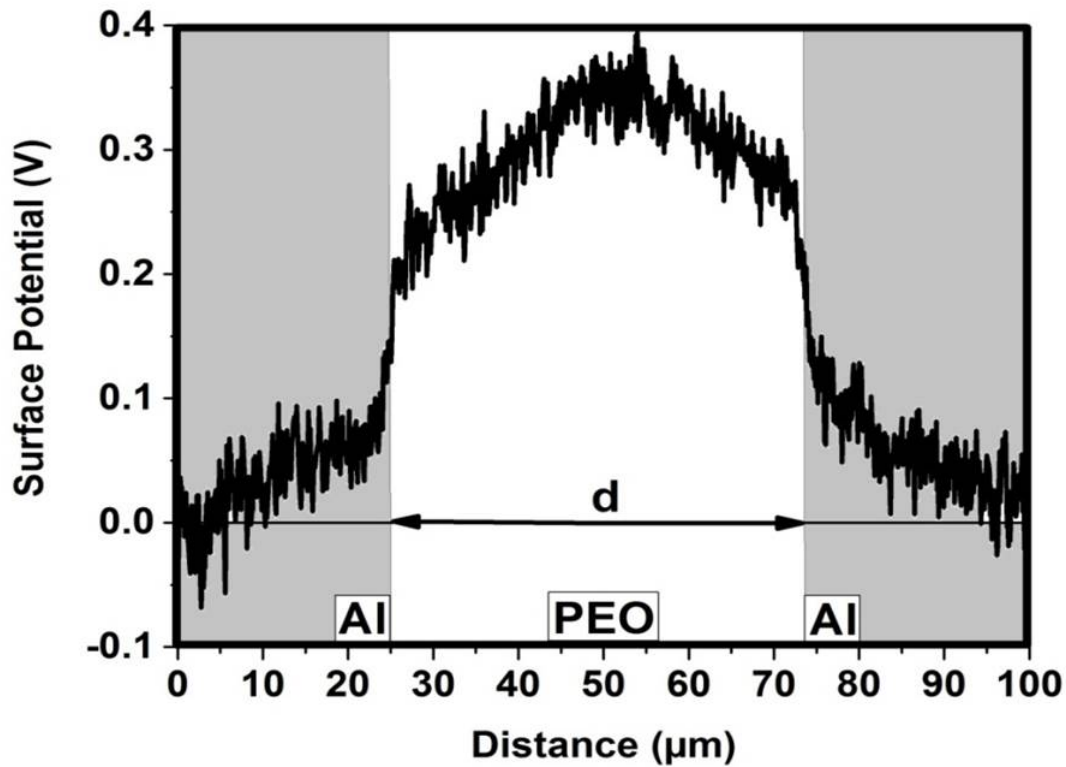
Figure 4.4: Measured surface potential referring to the type 1 sample (see Fig.3.3(a)) with zero voltage applied.

$$\alpha = arctan\left(\frac{h}{x}\right) = \left(\frac{\phi}{constant}\right)$$
$$Therefore, \phi = constant * arctan\left(\frac{h}{x}\right)$$

(4.1)

By using Equation 4.1, the normalized potentials for different lift heights h are plotted in Fig. 4.7(a) [49]. Experimentally measured potentials at two different lift heights ($h = 0.01\mu m$ and $0.5\mu m$) are shown in Fig. 4.7(b) for a comparison [49]. From both results, the experimental and the one calculated from Equation 4.1, it can be concluded that if we increase the lift height of the cantilever-tip, the potential drop over the electrode is also increased. In addition to this, it can also be concluded that if the angle α is increased along the electric field lines, the potential ϕ increases as well. Here, one more point, that has to be mentioned, is that the charges inside the material also have an impact on this potential drop. In Chapter 6, we have shown the transient impact of the internal charges on the potential drop during an applied external voltage.
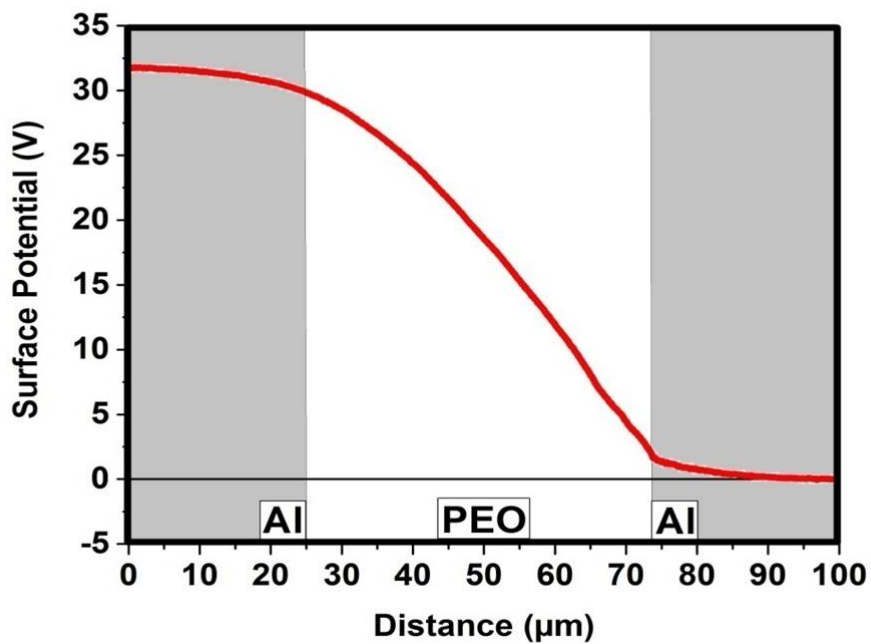
Figure 4.5: Measured surface potential referring to the type 1 sample (see Fig. 3.3(a)) with $30V$ applied.
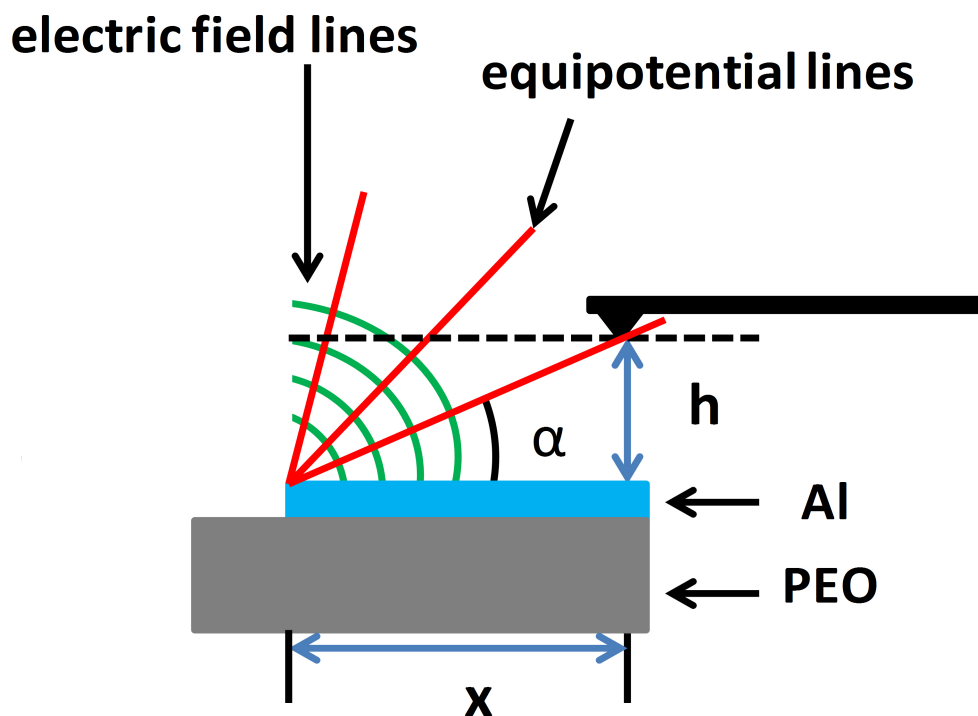
Figure 4.6: The electric field lines and the equipotential lines at the interface.
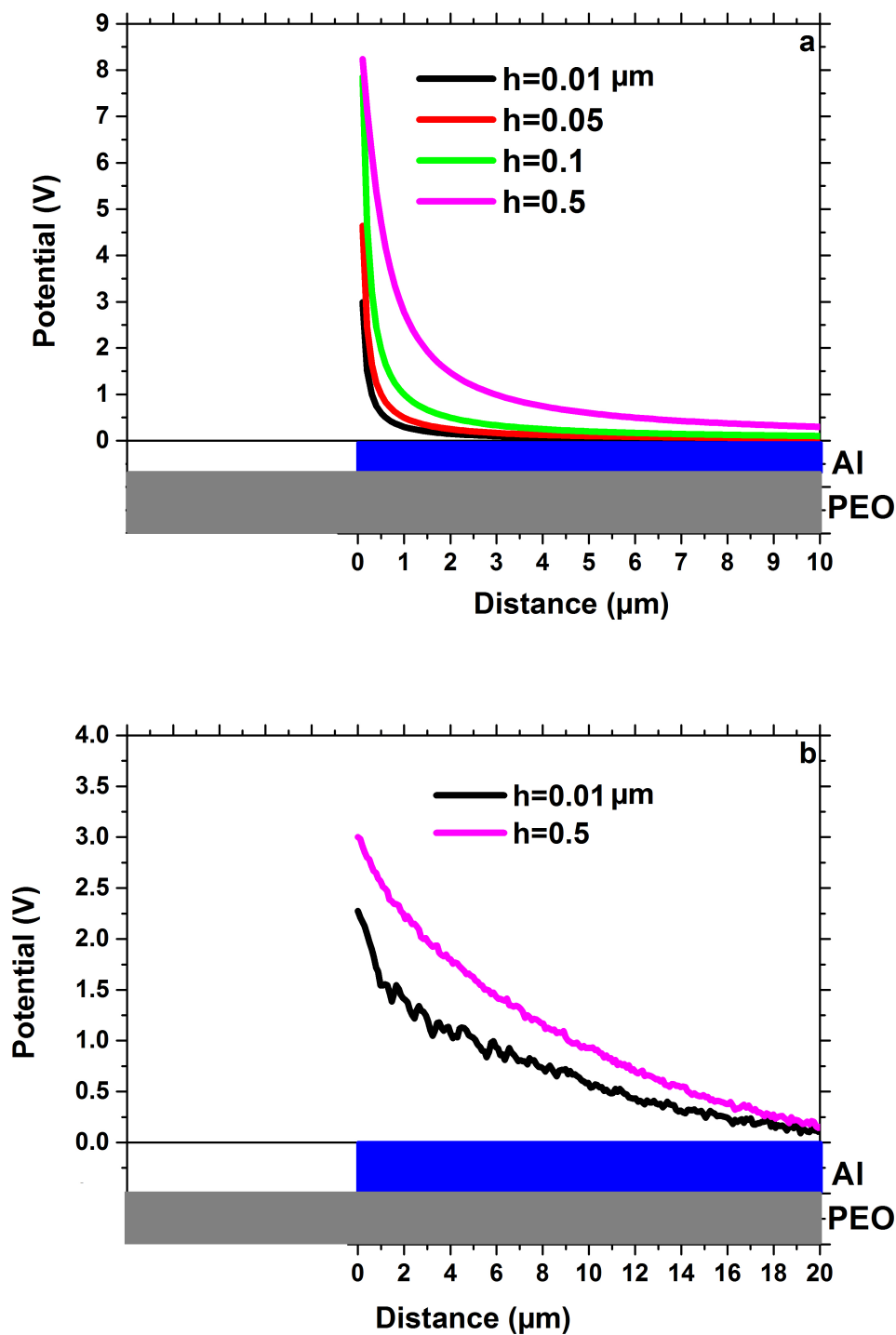
Figure 4.7: The modeled potential profiles (a) and the experimental potential profiles (b) at different heights above the sample surface.

Chapter 5

Calculation of a space charge distribution from a surface potential

5.1 Approach and assumption

The approach for the calculation of a space charge from a surface potential is as follows: First, the surface potential $\phi(x)$ distribution of the PEO sample with the structure shown Fig. 3.3, is measured by the KPFM as described in Chapter 4. Then, using the Poisson equation, the space charge $\rho(x)$ can be calculated by the following equation.

$$\rho(x) = -\varepsilon_0 \varepsilon_r \frac{d^2\phi(x)}{dx^2} \tag{5.1}$$

Where, ε_0 is the vacuum permittivity and ε_r is the relative permittivity of the material. For the PEO, the value of the relative permittivity is chosen at high frequencies $\varepsilon_r \approx 4$ [14].

In order to use the above mentioned approach for the calculation of the space charge $\rho(x)$ distribution from the surface potential $\phi(x)$ data delivered by the KPFM, the following presumption has been made. Space charges produce an electric field inside the PEO. In an unperturbed surface, the tangential component of this electric field $E(x)$ is continuous, so that one can assume that the equipotential surfaces are perpendicular to the film and that they are the same inside the PEO and close to the PEO/air interface (see Fig. 5.1) [49]. Because of that, one can quantify the space charge distribution $\rho(x)$ by measuring the surface potential $\phi(x)$ along the x-direction on the sample by using the Poisson equation.

This assumption can be checked easily by the use of finite element method (FEM) with COMSOL Multiphysics software. In this simulation, we have used a two dimensional ($2D$) model which represents our sample structure (see Fig. 3.3(a)). The simulation has been done under the biased condition in which we have applied $1V$. The results of the equipotential lines and the tangential component of the electric field are shown in Fig. 5.2 [49]. The simulation result confirms our assumption that the equipotential surfaces inside the PEO and close to the PEO/air interface are the same. From this result, we can say that a measurement of a potential distribution by the KPFM over a surface of a material is the same potential distribution found inside the material.
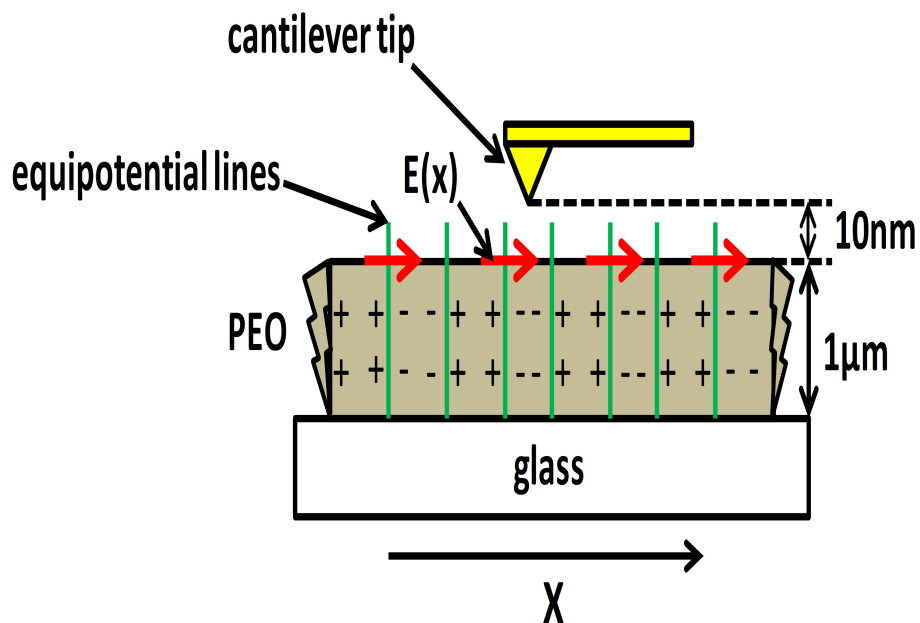
Figure 5.1: Equipotential lines, electric field and charges at the sample structure.
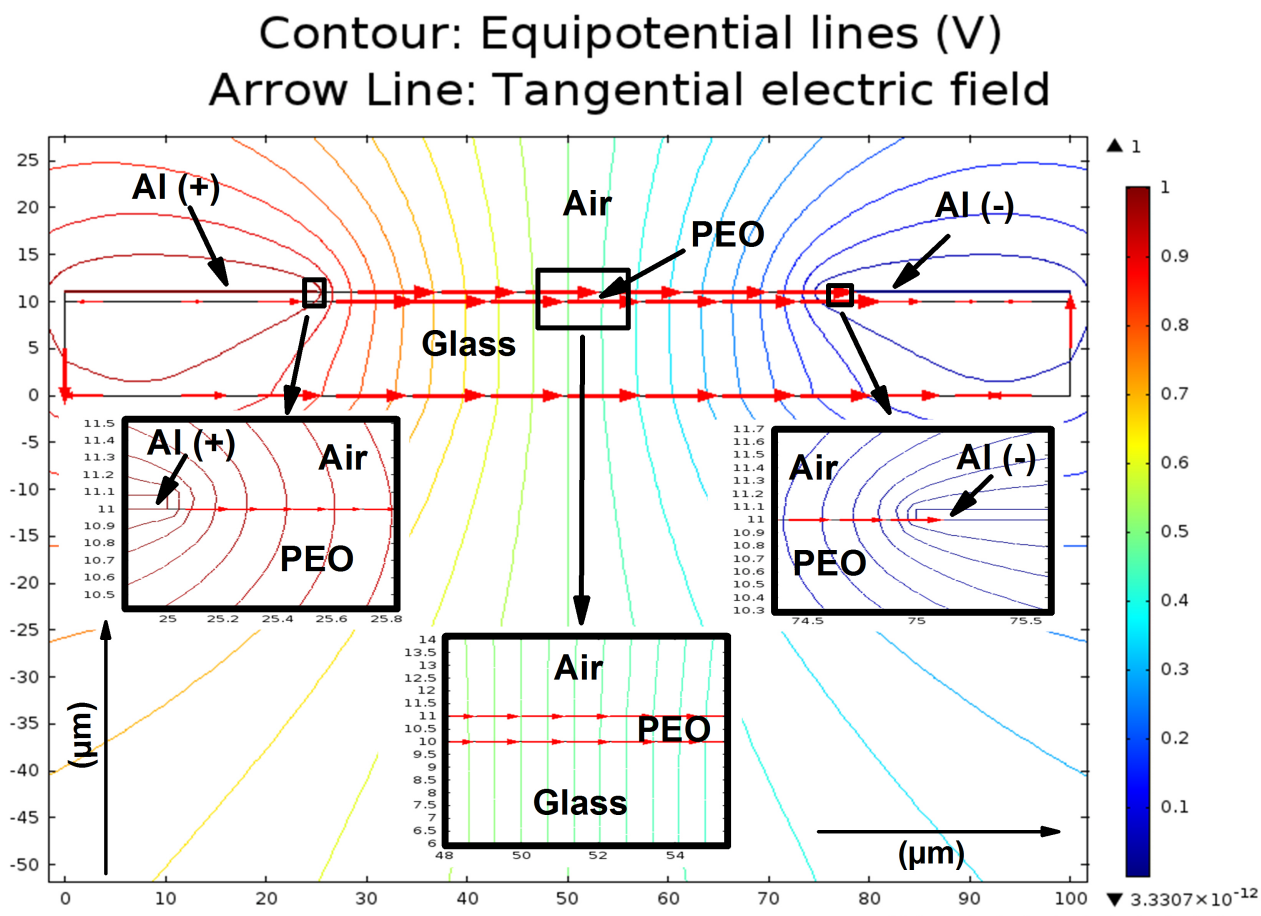
Figure 5.2: The equipotential lines and the tangential component of the electric field.

5.2 Requirement of a signal processing method to analyze the experimental data: why?

The KPFM machine delivers the noisy data of a surface potential. According to Equation 5.1, the space charge distribution is simply a second order derivative of the noisy surface potential. The calculation of the space charge distribution (the second order derivative) from the noisy surface potential is not an easy task. The reason for that is, a random noise in the data creates lots of difficulties during the calculation of second order derivatives of the data because numerical derivatives (especially higher order derivatives) amplify the noise [51, 52].
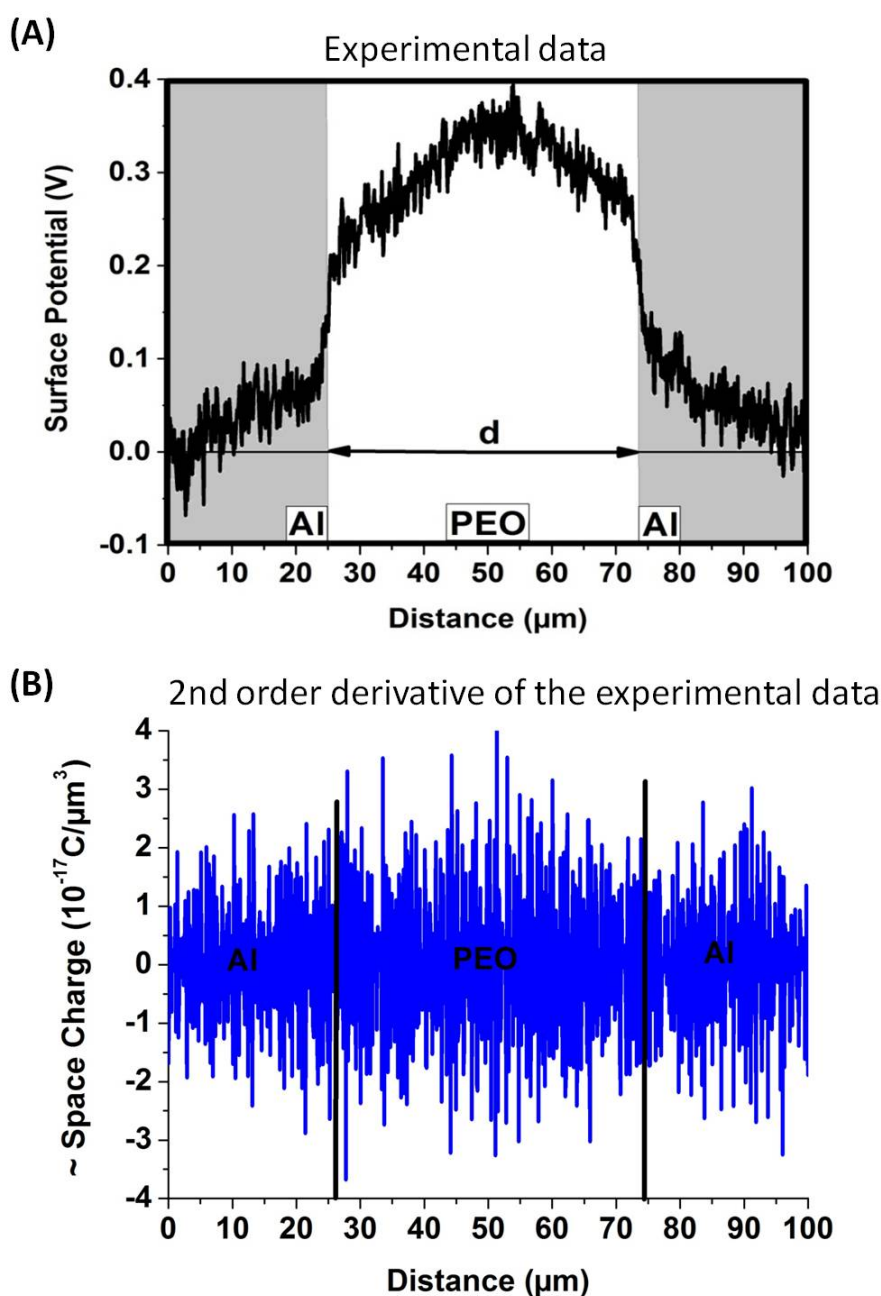
Figure 5.3: Experimental data of the surface potential (A) and the second order derivative of the experimental data (B).

Fig. 5.3(A) shows the noisy experimental data of the surface potential. The calculation of second order derivative of this experimental data is shown in Fig. 5.3(B). One can see clearly from Fig. 5.3(B) that it merely shows amplified noise instead of the space charge distribution. To overcome the problem of the noise in the experimental data of the surface potential, the use of signal processing methods on noisy data of the surface potential are needed in order to calculate the derivatives. The most common signal processing method for reducing a noise level in experimental data is data smoothing. For this purpose, a smoothing-derivative algorithm has been developed. This algorithm is described in the following section.

5.3 Smoothing-derivative algorithm

In order to make numerical derivative operation on the noisy data, the smoothing procedure is the most common approach for optimizing the signal-to-noise ratio in the noisy experimental data. The amount of effective smoothing operation which has to be done on the noisy data is an important criterion because a poor smoothing operation as well as an over smoothing operation leads to erroneous results. Many data smoothing techniques are available such as Fast Fourier Transforms, a moving average, Gaussian Filtering etc. The most common and widely used method for data smoothing and calculation of derivatives is the Savitzky-Golay (SG) method described in the publication of Savitzky and Golay [53]. This method is based on the least squares polynomial regression approach. In the following subsection, the SG method is depicted and evaluated critically. Then, considerations are brought forward on how to optimize and advance the SG method in order to use it for the present purpose, e.g. the calculation of the space charge distribution from the noisy surface potential data.

5.3.1 The Savizky-Golay method and its problem

In this approach, fixed degree polynomial functions are fitted on a specified amount of equally spaced data points. This specified amount of data points is termed as a data point window (DPW). This data point window moves over all data points. In this way, the polynomial functions smooth the data points. From these functions, the searched derivatives are calculated. The general equations of polynomial function and its derivatives in this case up to second order are

$$f(x) = a_0 + a_1 x^1 + a_2 x^2 + a_3 x^3 + ... + a_n x^n \tag{5.2}$$

$$\frac{df(x)}{dx} = a_1 + 2a_2 x^1 + 3a_3 x^2 + ... + n a_n x^{n-1} \tag{5.3}$$

$$\frac{d^2 f(x)}{dx^2} = 2a_2 + 6a_3 x^1 + ... + n(n-1)a_n x^{n-2} \tag{5.4}$$

However, this smoothing procedure is useful only for data representation. But, if smoothed values are necessary for further interpretation, then problems can arise (e.g. signal distortion). The reason for these problems is that both a chosen degree of polynomial (DOP) and the length of a data point window, affect individually the noise reduction and the signal fidelity [54].
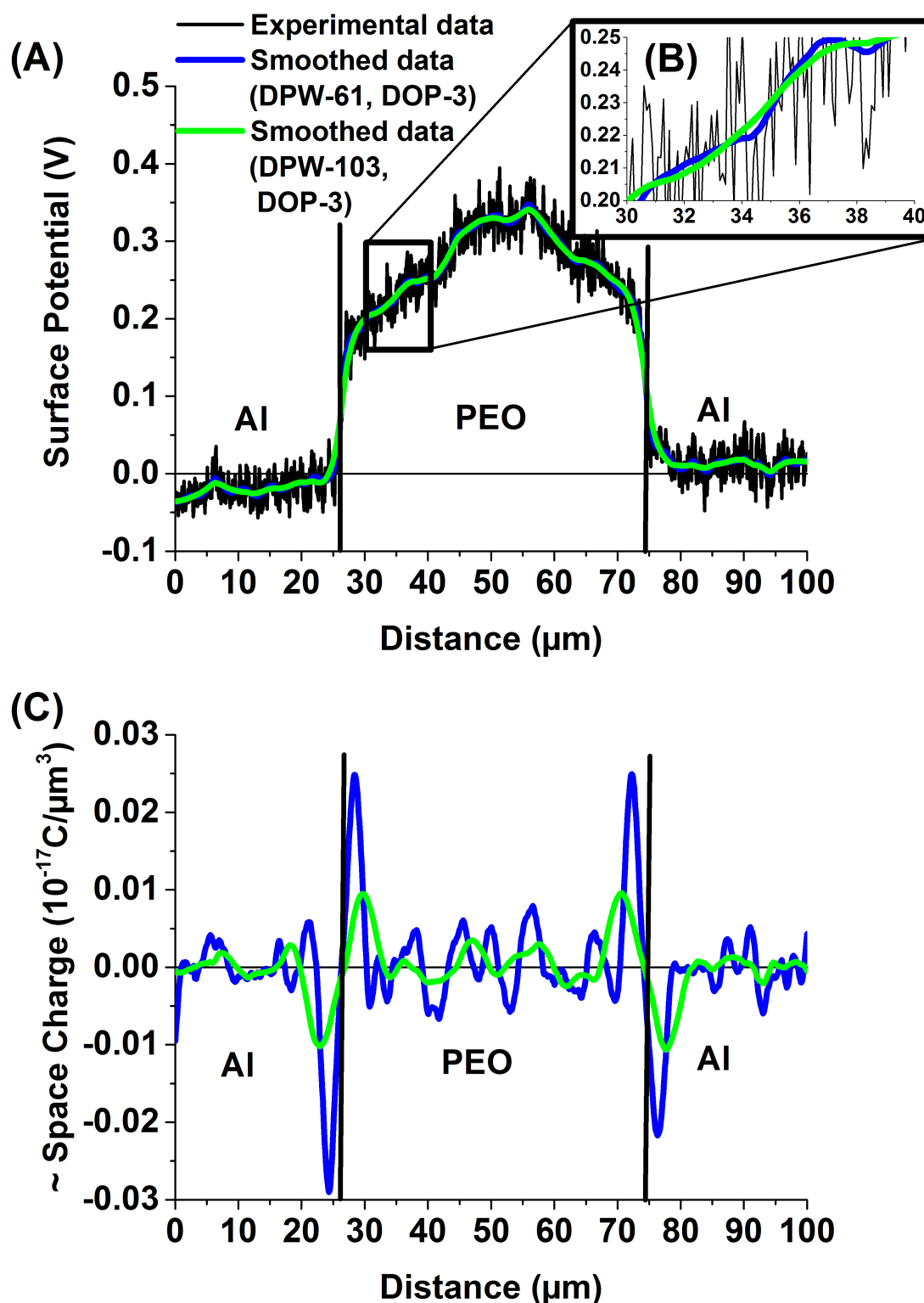
Figure 5.4: The effect of different DPW on the smoothed data (A, B) and on its second order derivative (C).

At first, we check how the length of a data point window affects the smoothing of the data and its derivative. To check this, the Savizky Golay smoothing and derivative operation was applied on the noisy experimental surface potential data shown in Fig. 5.4(A) at two randomly chosen data point windows with 61 and 103 points ($DPW = 61, 103$). The third degree of

polynomial ($DOP = 3$) was taken for both data point windows. One can see from Fig. 5.4 that the data point window affects significantly the smoothed data (see closely Fig. 5.4(B)) as well as the second order derivative (see Fig. 5.4(C)) [51].

Now, to check the effect of different degrees of polynomial, there were two different degrees of polynomial 3 and 5 ($DOP = 3, 5$) for $DPW = 103$ randomly chosen. From Fig. 5.5, it is clear that different degrees of polynomial give different results of the second order derivative [51].
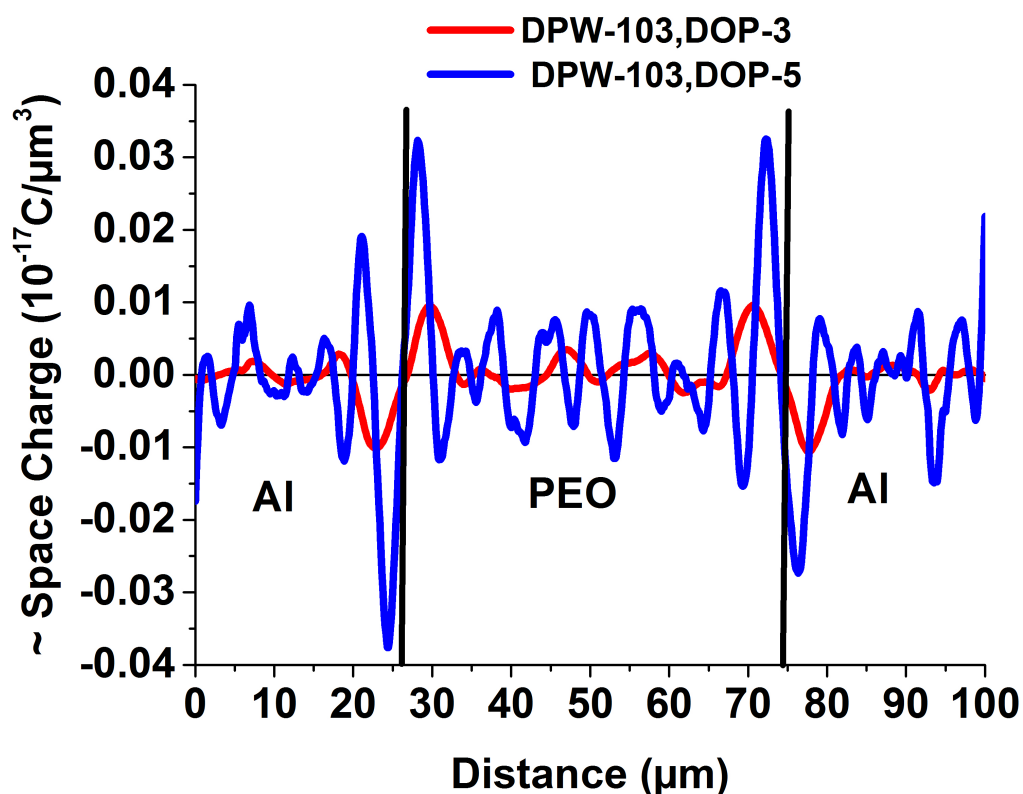
Figure 5.5: The effect of different DOP on second order derivative.

From the results presented in Fig. 5.4 and 5.5, it can be concluded that the data smoothing and calculation of its derivatives are highly sensitive to the chosen DPW and DOP. The results show that, for a particular set of data, the use of different DPWs with the same DOP gives completely different results of the smoothed data and its calculated derivative. The same problem arises when we use different DOPs with any particular DPW.

In the Savizky-Golay method, the length of a chosen data point window and a chosen degree of polynomial stay constant throughout the data smoothing and its derivative calculations. It can be possible that one needs to choose a higher or a lower degree of polynomial than the previously chosen degree in a particular data point window. It is already analyzed and documented in the literatures [54, 55, 56] that a low polynomial degree helps to maximize the noise reduction and a high polynomial degree helps to maximize the signal fidelity at a given length of a data point window. That is why one needs an optimal match between the polynomial degree and the length of a data point window. This can be achieved by using a statistical approach which is described in the next subsection.

5.3.2 Statistical approach for data analysis

As mentioned before, both the polynomial degree and the length of a data point window are critical parameters for smoothing and derivative operation on noisy data. Two different approaches, one for finding the best polynomial degree and the other for finding the best suitable length of a data point window are described one by one.

For finding the best polynomial degree for the given data point window, the statistical approach known as F-test (named after 'Sir Ronald A Fisher') has been used [57, 58]. For finding the best suitable length of the data point window, we have used a reverse calculation approach.

F-test

The F-test is used to test the overall fit of a regression model to a set of experimental data. In the F-test, two models with a different polynomial degree are compared. To compare two models, a ratio of a variance between estimated data by two models to a variance between experimental data and estimated data by a model is calculated. This ratio is called F-value or simply F.

$$F = \frac{a\ variance\ between\ estimated\ data\ by\ two\ models}{a\ variance\ between\ experimental\ data\ and\ estimated\ data\ by\ a\ model} \quad (5.5)$$

A variance χ^2 is calculated by the following equation.

$$\chi^2 = \frac{\sum_{i=1}^{i=N}\{(Experimetal\ data)_i - (Estimated\ data\ by\ a\ model)_i\}^2}{\nu} \quad (5.6)$$

Where, N is the total number of data points in a particular data point window. In another words, the variance is a measure of how well the model fits the actual data. Here, ν is called a degree of freedom. ν is defined as a total number of data points (N) used in estimation minus a total number of coefficients (n) of a polynomial function which is used for fitting the data points. The formula for ν is as follows.

$$\nu = N - n \quad (5.7)$$

For example, assume that, we have five data points, $N = 5$, and we want to fit a line, $Y = a_0 + a_1 x$, to these data points. The total number of data points used in the estimation will be $N = 5$. To fit the line to these data points, we need to calculate two coefficients a_0 and a_1. That means $n = 2$. So the degree of freedom ν in this case is $N - n = 5 - 2 = 3$.

In the formula of a variance that is Equation 5.6 , the numerator represents the sum of squared error which arises due to the difference between experimental data and estimated data

by a model. However, the value 'the sum of squared error' in the numerator of Equation 5.6 is a summed value. It will be influenced by the number of values that are summed. That means the more data points, the higher the sum of squared error. To eliminate this bias, it is divided by a degree of freedom ν. In another words, a variance χ^2 is simply an average sum of the squared error.

As mentioned before, the variance gives the information about how well the model fits the actual data, but to see an improvement by different models which means how much one model has improved a result as compared to the previous model, we need to calculate a ratio called F-value. In the process of comparing different models with different degrees of polynomial, first, we start with a very basic model. Suppose, we have a data point window with N number of experimental data points shown in Fig. 5.6(A). We fit to these data points a polynomial function with degree n which will be our Model 1. We start with a line with zero degree of polynomial ($n = 0$) which can be a line of an average of the data points (see Fig. 5.6(A)).

Now, we fit to the same data points a polynomial function with degree m which will be our Model 2. m is always greater then n ($m > n$). In this case, for example, we fit a line with polynomial degree of one ($m = 1$) which is $Y = a_0 + a_1x$ (see Fig. 5.6(B)). The dotted lines in Fig. 5.6 represent the difference between the estimated data by the models and the actual data. As we are comparing Model 1-the polynomial function with degree n and Model 2-the polynomial function with degree m, the F-value is calculated as follows:

First, we calculate the variance χ_1^2 between the experimental data and the estimated data by Model 2 (Fig. 5.6(B)).

$$\chi_1^2 = \frac{\sum_{i=1}^{i=N}\{(Experimental\ data)_i - (Estimated\ data\ by\ Model-2)_i\}^2}{\nu_1} \tag{5.8}$$

Then, the variance χ_2^2 between the estimated data by Model 1 and by Model 2 is calculated (Fig. 5.6(C)).

$$\chi_2^2 = \frac{\sum_{i=1}^{i=N}\{(Estimated\ data\ by\ Model-1)_i - (Estimated\ data\ by\ Model-2)_i\}^2}{\nu_2}$$
$$\tag{5.9}$$

where, the degrees of freedom are $\nu_1 = N - m - 1$ and $\nu_2 = (N - n - 1) - (N - m - 1) = m - n$.

The equation for the F-value is then.

$$F = \frac{\chi_2^2}{\chi_1^2} \tag{5.10}$$
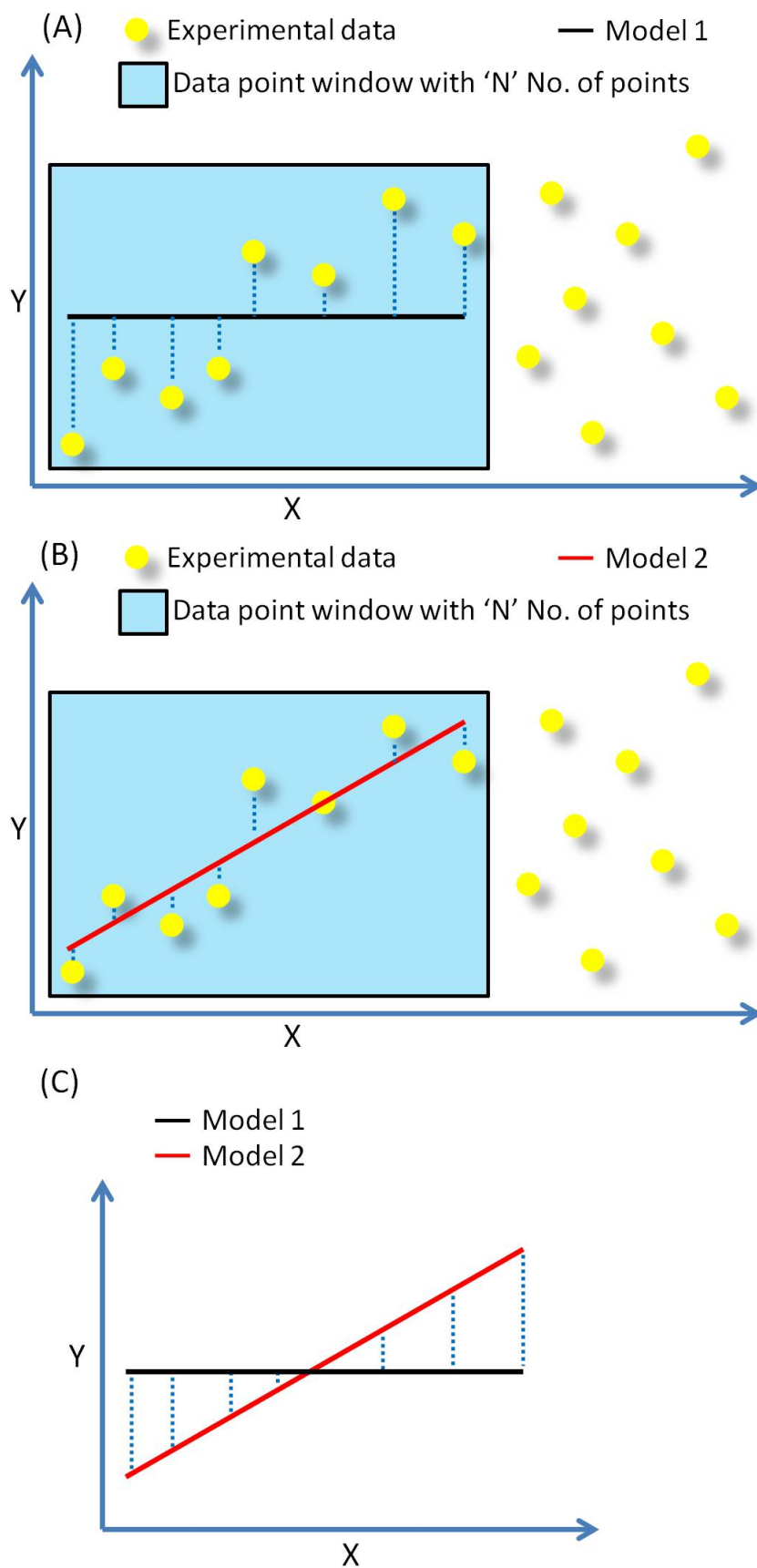
Figure 5.6: Approach for comparing two models.

Here, the F-value is a measure of how much Model 2 has improved the estimation of experimental data compared to the level of inaccuracy of Model 2 with respect to the level of inaccuracy of Model 1. To understand this, let say, if Model 2 is better than Model 1, then we expect the difference (χ_1^2) between experimental data and the estimated data by Model 2 to be small and the difference (χ_2^2) between the estimated data by Model 1 and the estimated data by Model 2 to be large. In short, a good model should have a large F-value because the numerator will be bigger than the denominator.

To obtain an optimum degree of polynomial function for fitting the data points, the F-test is conducted as follows: two models with different polynomial degrees, for example, Model 1 with a polynomial degree n and Model 2 with a polynomial degree m ($m > n$), are compared under the null hypothesis. To choose from two different polynomial degrees n and m which one is better than the other, the null hypothesis can be formed in a following way: Model 2 with the polynomial degree m is not significantly better than Model 1 with the polynomial degree n. This means, Model 1, which is a polynomial function with the degree n, is acceptable to be used to fit the data. The null hypothesis is nothing but an assumption which we make and then check its probability of being 'True' or 'False'. The probability of the null hypothesis being 'True' or 'False' can be checked by calculating the F-value (F) and by comparing this value with the critical F-value ($F_{\copyright}$) of the F probability distribution function in standard statistical tables at different α significance levels [58]. The F probability distribution function gives the probability $p(F, \nu_1, \nu_2)$ of all possible F-values for a given set of degree of freedoms (ν_1, ν_2). It is calculated by the following equation [58].

$$p(F, \nu_1, \nu_2) = \frac{\Gamma\left(\dfrac{\nu_1 + \nu_2}{2}\right)}{\Gamma\left(\dfrac{\nu_1}{2}\right)\Gamma\left(\dfrac{\nu_2}{2}\right)} \left(\frac{\nu_1}{\nu_2}\right)^{\left(\frac{\nu_1}{2}\right)} \left[\frac{F^{\left(\frac{1}{2(\nu_1 - 2)}\right)}}{\left(1 + \dfrac{F\nu_1}{\nu_2}\right)^{\left(\frac{1}{2(\nu_1 + \nu_2)}\right)}}\right] \tag{5.11}$$

See the literature [59] for a derivation of the above equation. As it can be seen from the above equation the probability $p(F, \nu_1, \nu_2)$ of F-values is dependent on a given set of degree of freedoms (ν_1, ν_2), a shape of a probability distribution graph of F-values is different for different sets of degree of freedoms (ν_1, ν_2). To understand the concept, a sample representative shape of the graph of the probability distribution of F-values is shown in Fig. 5.7. First, we calculate the F-value for a given set of degree of freedoms to compare Model 1 and Model 2. Then, we form the null hypothesis as mentioned above. After that, we check the probability of our null hypothesis being 'True' by calculating the probability of the calculated F-value for a given set of degree of freedoms. Whatever the probability of the calculated F-value is, is the probability of the null hypothesis being 'True' that we decide. To decide Model 2 is significantly better than Model 1, we set a minimum probability of the null hypothesis being 'True'. This minimum probability is known as a significance level α. The F-value at this α level is known as the critical F-value ($F_{\copyright}$). If the calculated F-value is higher than $F_{\copyright}$ then the probability of the null hypothesis being 'True' is below the preset minimum probability. Then, we

can conclude that the chances of Model 2 being not significantly better than Model 1 are low which means Model 2 in fact gives a better result than Model 1. In the sample graph presented in Fig. 5.7, it is shown $F_{©}$ at $\alpha = 5\%$ which means if the calculated F-value is bigger than $F_{©}$ then we are less than 5% sure that Model 2 does not provide a significantly better result than Model 1. In another wards, this can be interpreted that the chance of Model 2 giving a significantly better result than Model 1 is more than 95%.
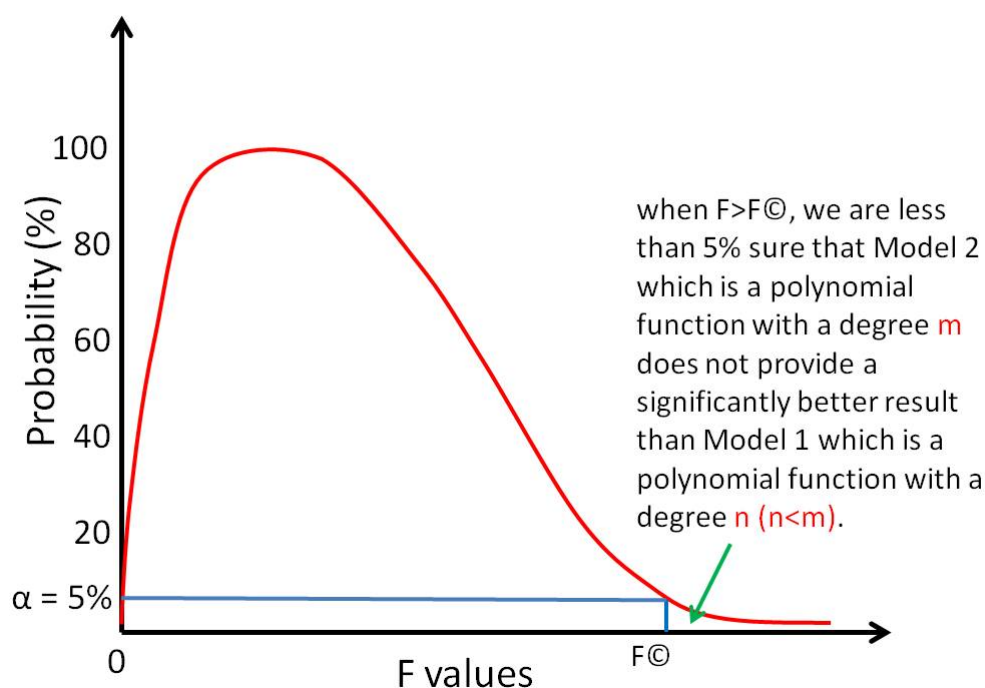
Figure 5.7: A sample graph of probability Vs F-values.

The significance level α is generally set to either 1% or 5% which means, there is only 1% or 5% probability that the null hypothesis is 'True'. This means, we are only 1% or 5% sure that Model 2 is not better than Model 1. Put this in another words, when the null hypothesis has only 1% or 5% chance of being 'True', that means, it is more likely that Model 2 is better than Model 1. In our calculation, 5% significance level was chosen. The reason is explained at the end of the section 5.4.

In our F-test, when F is bigger than $F_{©}$ ($F > F_{©}$), this means the polynomial function with degree m gives a significantly better result than the polynomial function with degree n. Then, the polynomial degree m is taken as a new polynomial degree n which is then compared with a new polynomial degree m where, m is always greater than n ($m > n$). In this way, the best fitting polynomial degree is found by making series of F-tests with different values for m and n, as the data point window sliding over the experimental data. Different data point windows in series of equal length yield polynomial functions with different polynomial degrees. After that, the second order derivatives of these polynomial fit functions are calculated. This means, the space charge distribution is calculated according to Equation 5.1.

Here, one thing is to be mentioned that the space charge distribution calculated from the noisy experimental surface potential data by the above mentioned approach yields different

space charge distributions for different lengths of data point windows. To choose which space charge distribution is close to the most probable space charge distribution, a further approach is needed which decides the suitable length of a data point window. For that we use the reverse calculation approach.

Reverse calculation approach

The space charge distribution is the second order derivative of the surface potential which means two times integration of the space charge distribution considering the boundary conditions should yield the surface potential.

$$\phi(x) = -\int_0^x \int_0^x \frac{\rho(x)}{\varepsilon_0 \varepsilon_r} dx dx \tag{5.12}$$

The reverse calculation approach is that, at first the space charge distributions are calculated using the F-test approach for all possible lengths of data point windows. Then, through the integration procedure, the surface potentials from all calculated space charge distributions are recalculated and compared to the experimental surface potential. For a comparison, the sum of squares of differences (*Deviation*) between the experimental and the recalculated surface potential at a given length of a data point window is calculated for all possible lengths of data point windows. Within each data window, the optimal polynomial degree is used. The deviation is calculated by the following equation.

$$Deviation = \sum_{i=1}^{n} (SP_{(exp)i} - SP_{(cal)i})^2 \tag{5.13}$$

Where,
SP_{exp} : a value of the experimental surface potential
SP_{cal} : a value of the recalculated surface potential from the space charge distribution
n : the total number of data points

The length of the data point window for the final calculation of the space charge distribution is decided where the *Deviation* between the experimental surface potential and the recalculated surface potential from the space charge distribution is at a minimum and the recalculated surface potential fits the experimental surface potential. In the calculation of the space charge distribution, the second derivative is taken at each center of the data point window.

5.4 Results from the algorithm

The algorithm flow chart is shown in 5.8 [52]. By using the approaches described in section 5.3, the space charge distributions were calculated from the measured 1024 experimental data points of the surface potential. In this algorithm, the values of space charge distribution (the second order derivative) are considered at each center of the data point windows. The space charge distributions were calculated with different lengths of a data point window starting from
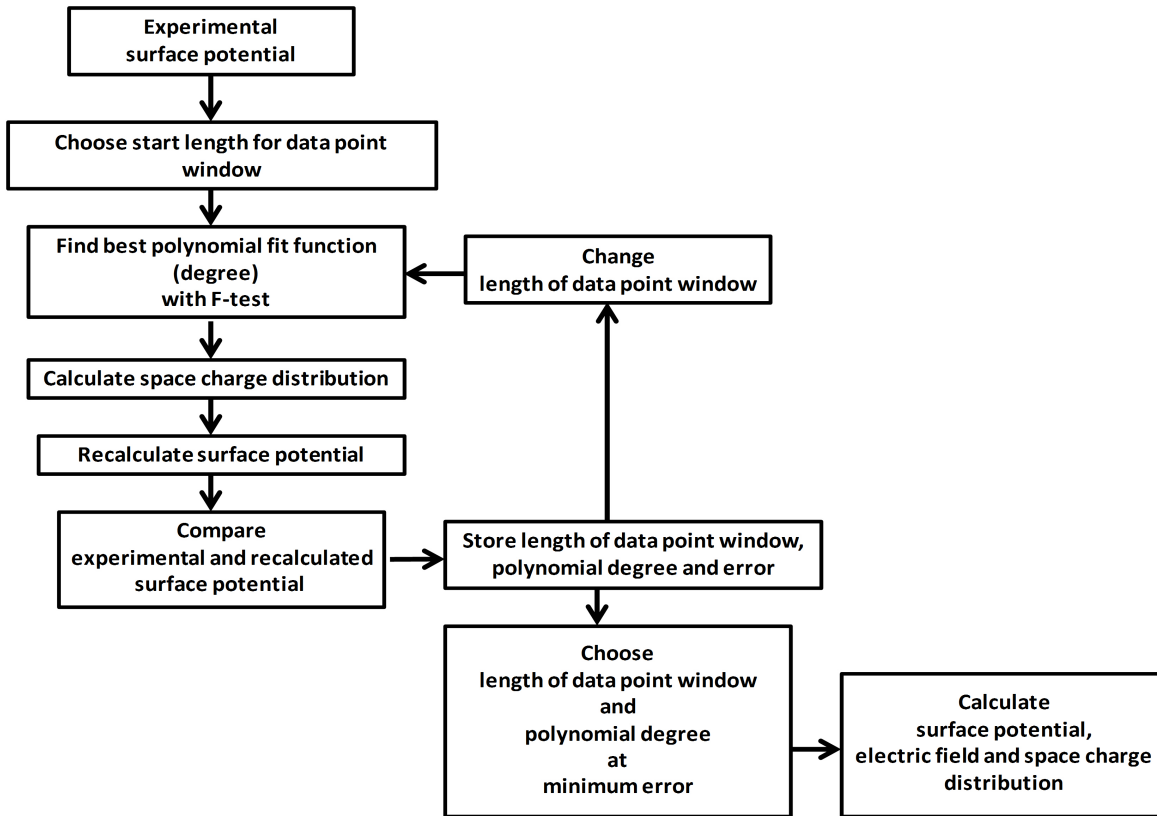
Figure 5.8: Flow chart of the algorithm.

1 to 307 data points in a window. The end limit of the length of a data point window is chosen where the algorithm starts to oversmooth the experimental data. That means the smoothed data do not fit the experimental data. The even and the next odd polynomial degrees (i.e. 2 and 3, 4 and 5, 6 and 7 etc.) yield equivalent results for central point smoothing in the Savitzky- Golay filter [53, 54] which we have also checked. The F-test was performed on a range of 1 to 23 odd polynomial degrees and the increment of the length of a data point window was also odd (i.e. $1, 3, 5, \ldots, 307$). In this way, it helps to reduce the simulation time.

In Fig. 5.9 (a.1, a.2, a.3) the space charge distributions calculated from the experimental surface potential (shown in Fig. 5.3(A)) with three different lengths (21, 151, 153) of data point windows are shown as an example [52]. All three space charge distributions are different relative to each other. That is why, to choose the most probable space charge distribution, the surface potentials are recalculated from every space charge distribution by the reverse calculation approach. Fig. 5.10(b.1, b.2, b.3) shows the surface potentials recalculated from the space charge distribution which are depicted in Fig. 5.9 [52]. In Fig. 5.10(b.1, b.2, b.3), it is shown how well the recalculated surface potentials fit to the experimental surface potential. Fig. 5.10(b.3) depicts the best fit according to Equation 5.11 calculated from the data window with 153 data points sliding along the data set. The value of *Deviation* attains its minimum for this length of a data window. All other data windows until 307 data points produced higher values of *Deviation*. So it can be deemed acceptable that the most reliable space charge distribution is the one which is calculated using the data window with 153 points.

As mentioned before, when using the F-test a significance level needs to be set. In the
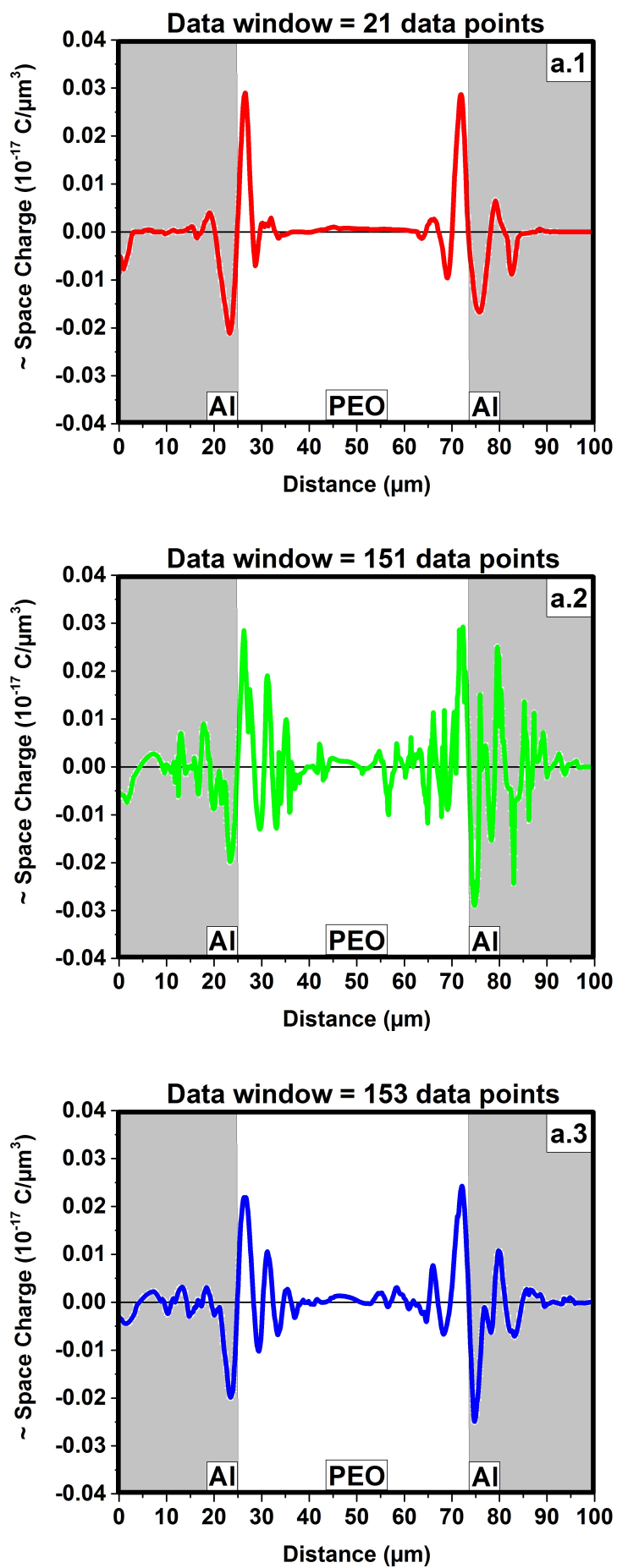
Figure 5.9: Space charge distribution for different lengths of data windows.
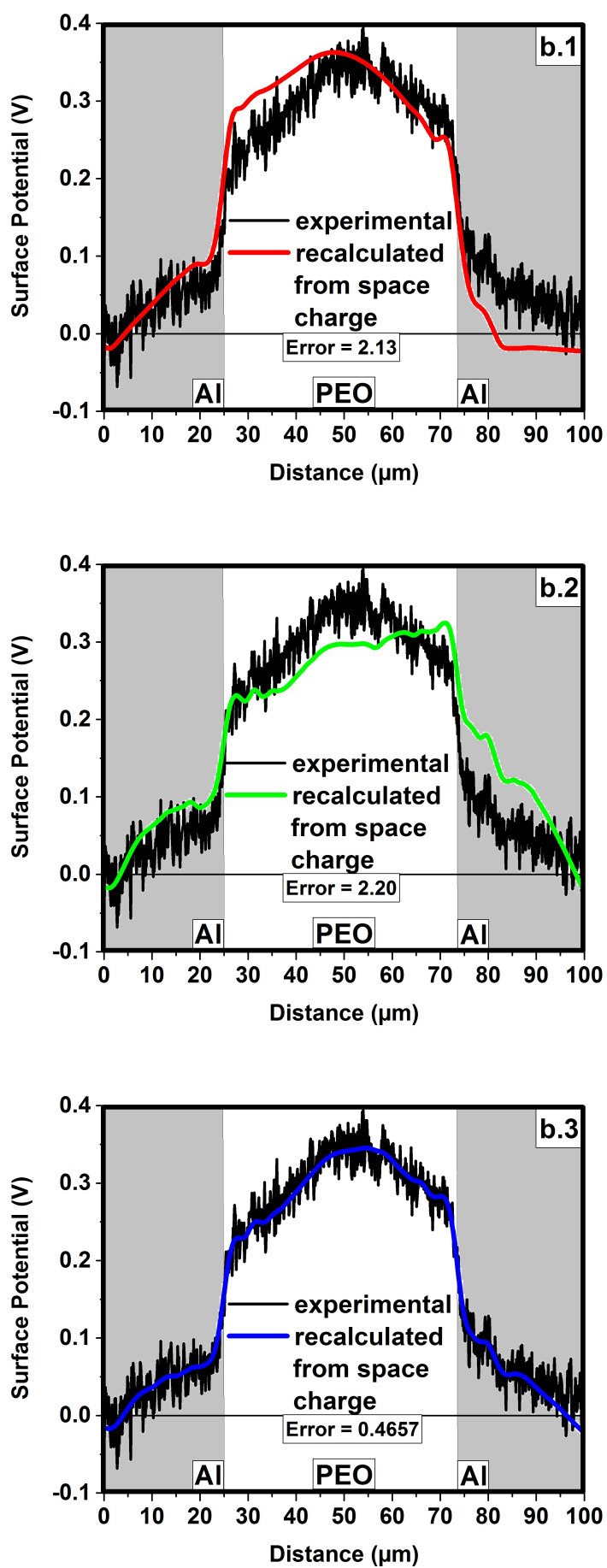
Figure 5.10: Recalculated surface potential for different lengths of data windows.

present study, the calculations of the space charge distributions were conducted by using different significance levels (1%, 5%, 15%, 25% and 50%) [52]. After that, the minimum of *Deviation* calculated by using different significance levels were compared. Table 5.1 shows that the minimum of *Deviation* for 5% significance level is minimal compared to the minimum of *Deviaiton* for other significance levels. It was also observed that the oscillations in the space charge distribution were increased with increasing significance levels from 5%. It might be due to the unnecessary use of a high degree polynomial function because the higher the significance levels, the higher the probabilities of using high degree polynomial functions. It has been analyzed before [54] that the use of the high degree polynomial function is not very useful as compared to the low degree polynomial function in terms of a noise reduction. In these calculations, 5% significance level is the best choice to use between a low degree polynomial function (to maximize the noise reduction) and a high degree polynomial function (to maximize the signal fidelity). 5% significance level is also recommended by Fisher [57], Neyman and Pearson [60].

Significance level α	Deviation
1%	0.4977
5%	0.4657
15%	0.4670
25%	0.4733
50%	0.4697

Table 5.1: Different significance level α

5.5 The authenticity check of the algorithm result

As it can be seen from Fig. 5.9(a.3)), the reliable space charge distribution reveals charge oscillations in the volume of PEO. In the best of our knowledge, this kind of charge oscillations has not been detected so far for solid polymer electrolytes and solid insulating materials. However, it should be mentioned here that, for ionic liquids such charge oscillations were predicted by M. V. Fedorov and A. A. Kornyshev [61]. M. V. Fedorov and A. A. Kornyshev have performed molecular dynamic simulations for a simplified system of an ionic liquid to understand the double layer formation in ionic liquids at a room temperature. Their results show strong oscillations of electrostatic potential near each electrode extending from the electrode to the volume of an ionic liquid (see Fig. 1 in[61]). These oscillations of the electrostatic potential clearly indicate charge oscillations in the ionic liquid. Similar results were also predicted by H. Lu and his colleagues [62]. It has to be checked if the space charge oscillations in the volume of the PEO are a real physical phenomenon or an artifact of the calculation procedure. The following approach has been carried out [52].

First of all, the surface potential and the space charge distribution are assumed by means of a mathematical function. Then, white Gaussian noise is added to the assumed surface potential. After that, the assumed surface potential data with the white Gaussian noise are processed by the algorithm described in Section 5.4 and the space charge distribution is calculated. At the end, one can compare the calculated space charge distribution with the assumed space charge distribution to see the effect of the algorithm.
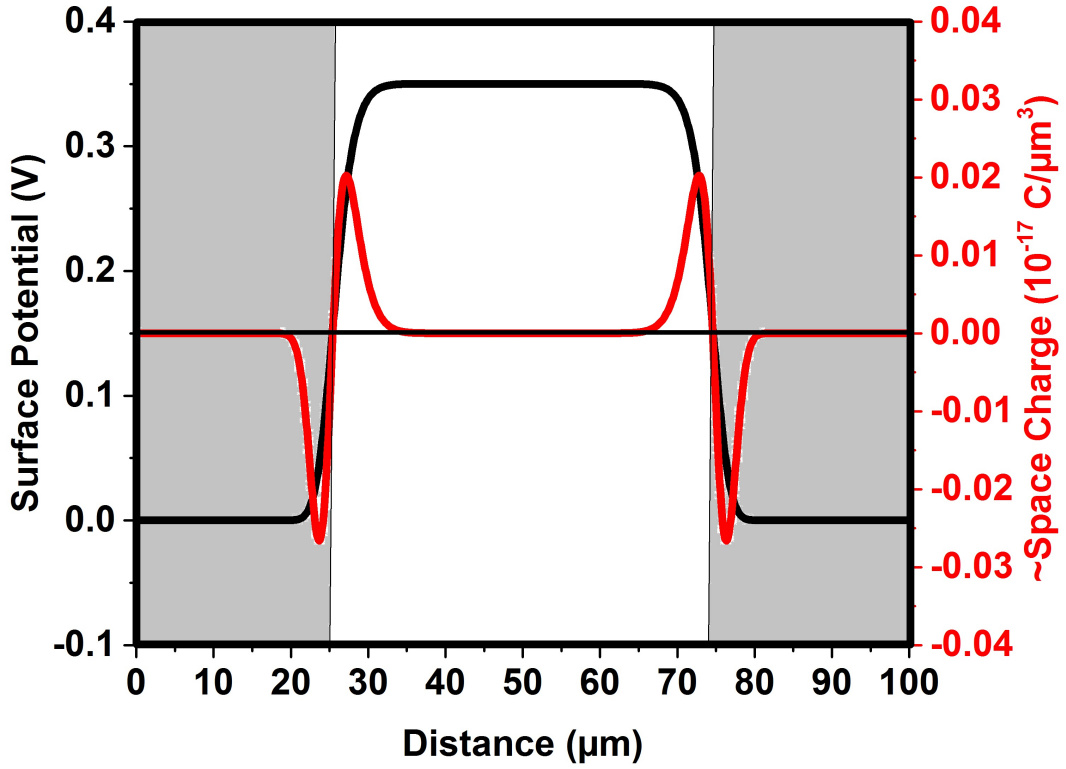
Figure 5.11: Assumed surface potential and space charge distribution.

The surface potential $\phi(x)_{assumed}$ is assumed by considering the following mathematical equation.

$$\phi(x)_{assumed} = H \left[1 - tanh^2 \left\{ a \left(\frac{x - \frac{c}{2}}{b} \right)^n \right\} \right]$$

(5.14)

$$where, \ H = 0.35V, \ a = 0.8, \ n = 8, \ b = 24\mu m, \ c = 100\mu m$$

The reason to choose this mathematical function is that it gives a shape of the surface potential profile which is comparable to the shape of the experimental surface potential profile in the short-circuited condition (see Fig. 5.3(A)). The parameters H, a, n, c and b are chosen to achieve the shape of the assumed surface potential profile as close as possible to the experimental surface potential profile. The value of the parameter c is a total scan range which is $100\mu m$ in our case. The space charge can be assumed by the second order derivative of Equation 5.14. The same number of data points as in the experiments (1024 points) are generated by this mathematical function. The assumed surface potential without added noise and the assumed space charge distribution profile are shown in Fig. 5.11 [52].

Now, the white Gaussian noise is added to the assumed surface potential data by using the inbuilt function from Matlab R2015a software. The amount of noise added to the assumed sur-
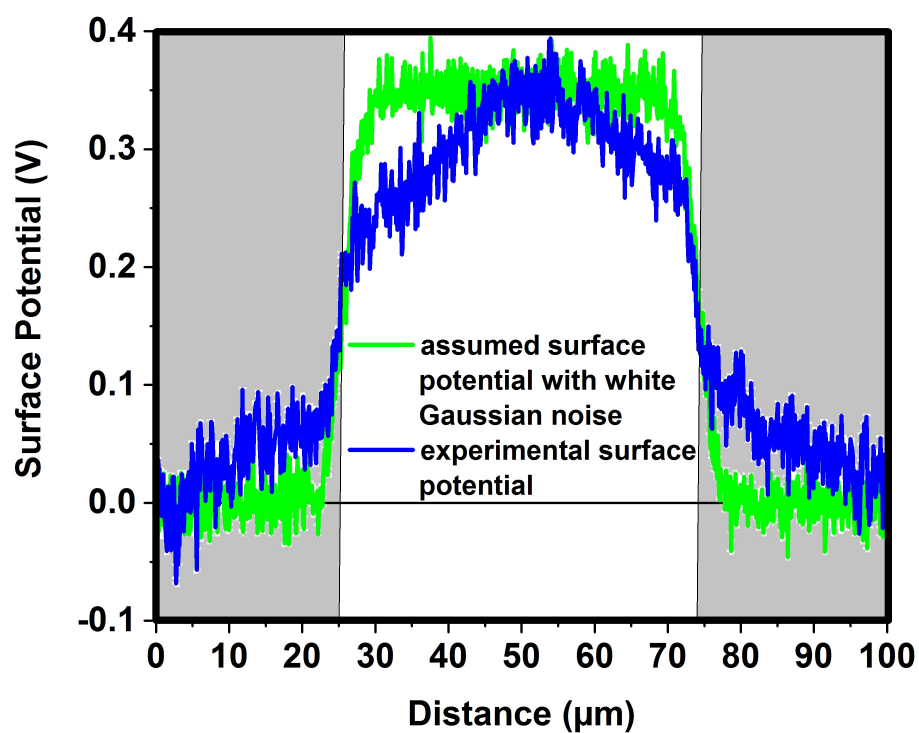
Figure 5.12: Assumed surface potential with white Gaussian noise and experimental surface potential.
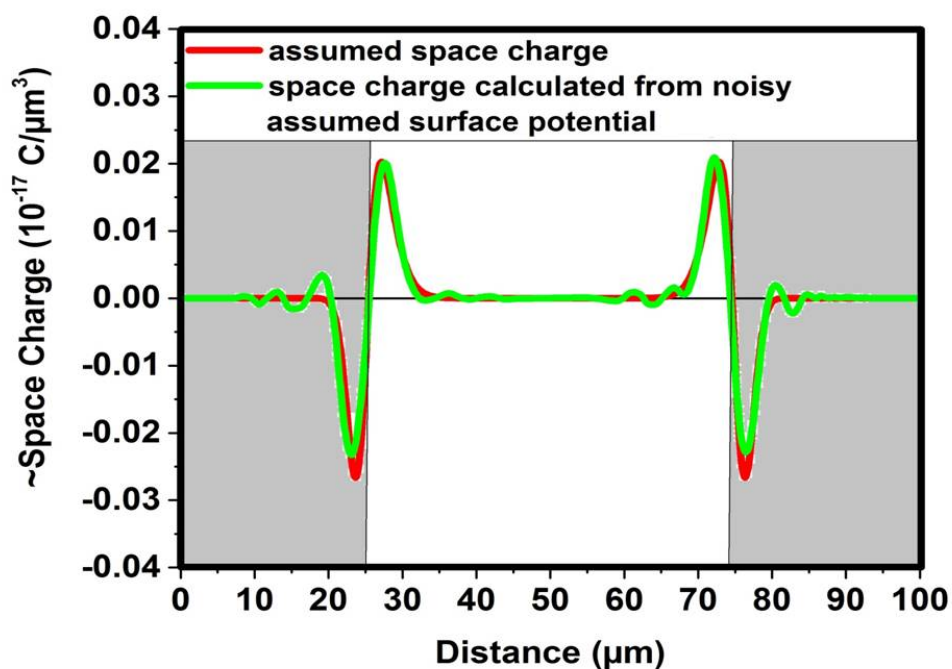
Figure 5.13: Space charge distribution from the assumed surface potential with and without noise added.

face potential data is approximately the same as the noise coming from the experimental setup. One can compare the assumed surface potential profile with added noise and the experimental surface potential profile in Fig. 5.12 [52].

As there is no oscillation in the assumed space charge distribution, the algorithm should calculate from the noisy assumed surface potential a space charge distribution which has to be as close as possible to the assumed one. Fig. 5.13 shows the comparison between the assumed space charge and the calculated space charge from the assumed potential with noise added [52]. One can see clearly from Fig. 5.13 that the oscillations produced by the algorithm in the middle part of the space charge distribution are close to zero as assumed in the space charge distribution. In comparison to this, the oscillations found in the space charge distribution calculated from the experimental surface potential (see Fig.5.9(a.3)) are significantly larger in magnitude and cannot be an artifact from the algorithm. This means that the oscillations found in the PEO are a real physical phenomenon. In addition to this, we have also detected oscillations in the potential profile during the applied voltage. These oscillations in the potential profile also give an indication that the charge oscillations found in the PEO are a real physical phenomenon. The oscillations in the potential profile are discussed more in detail in Chapter 6, Section 6.2.1.

Chapter 6

Charge distributions: comparison between pure PEO samples and PEO samples doped with Li-salt

In this chapter the formation and movement of charges in pure and $0.1wt\%$ Li-doped PEO under biased and unbiased condition is compared.

6.1 Comparison before application of an external electric field

Fig. 6.1(a.1) and Fig. 6.2(b.1) show the comparison of the surface potential between the short-circuited doped and undoped PEO samples [49, 63]. The undoped sample produces a higher surface potential than the sample doped with $0.1wt\%$ $LiClO_4$ does. The higher the doping level the lower is the mid-sample potential. The concentration of $LiClO_4$ is choosen in a way that we can still identify the electrode/electrolyte interface. Using the procedure described in Chapter 5, we find the space charge distributions as shown in Fig. 6.1(a.2) and Fig. 6.2(b.1) for the undoped samples and the samples doped with $LiClO_4$ [49, 63]. The result of the potential measurement is similar to our former findings [20]. However, at that time we were not able to detect the charge oscillations visible now in Fig. 6.1(a.2) and Fig. 6.2(b.2).

Fig. 6.1(a.2) and Fig. 6.2(b.2) shows the comparison of the space charge distributions between the doped and undoped samples in the short-circuit condition before application of an external field. In both type of samples, positive space charges and negative induced space charges are detected respectively in the PEO and on the Al electrodes at the Al/PEO interfaces. The development of positive charges at the region near the electrodes can be elucidated by the following mechanism [20]: It is assumed that positive ions are immobile and negative ions are mobile. The electrodes attract negative ions by their image charges. These negative ions together with their image charges form dipoles with lengths of atomic distances. Further negative ions from the region near the electrode are pushed back into the volume of the sample by these dipoles with their fields and leave behind the immobile positive charges. The atomistic thin dipole double layer at the electrodes does not contribute significantly to the potential in the sample and is not detected in the measurement. These positive charges produce the first positive peak of the space charge near the electrodes. Integration (twice) over these positive charges yields the increase of the potential at the electrodes. A graphical representation of this mechanism is shown in Fig. 6.3.
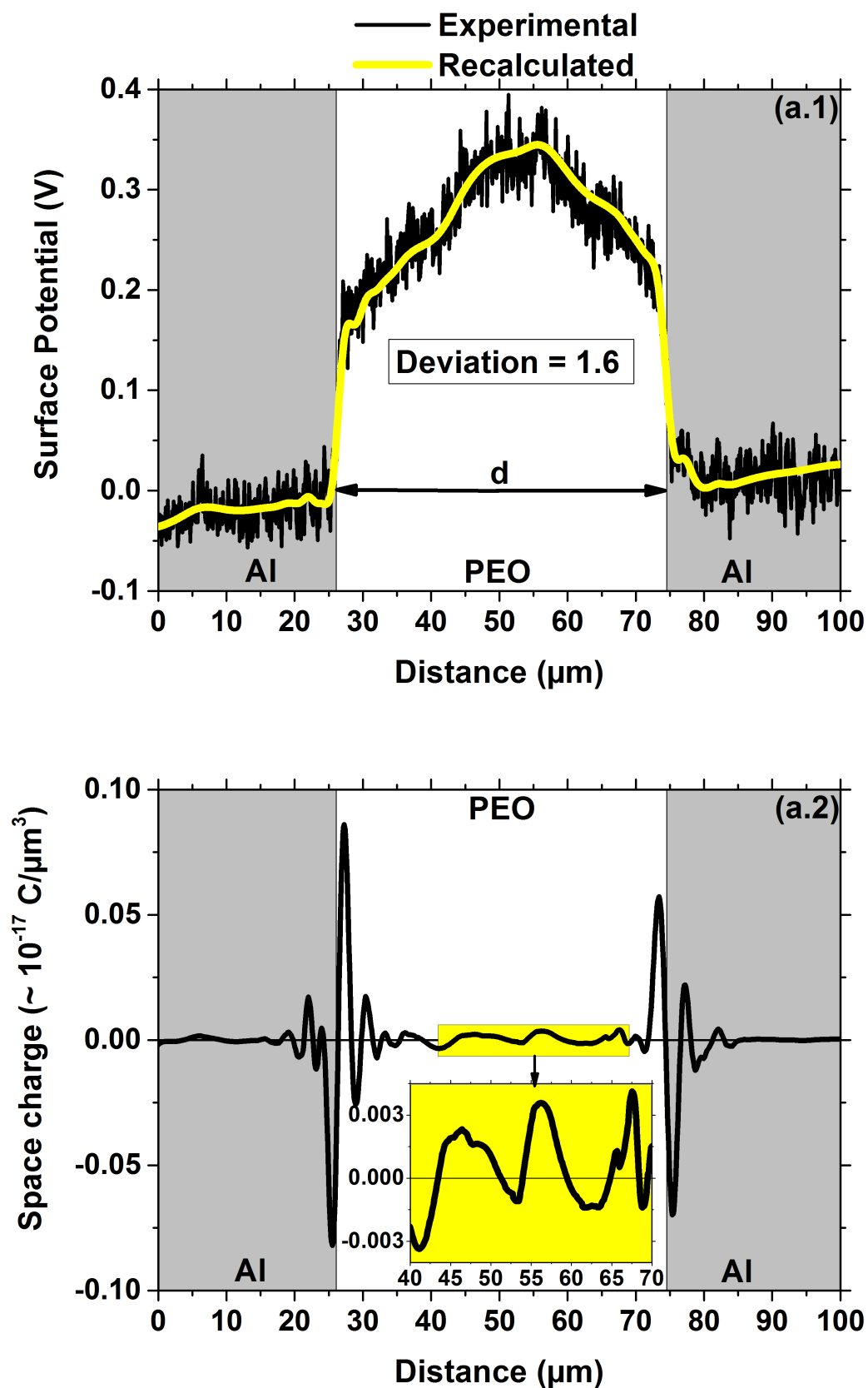
Figure 6.1: Surface potential (a.1) and space charge distribution (a.2) for undoped PEO samples under short-circuited condition before application of the external electric field.
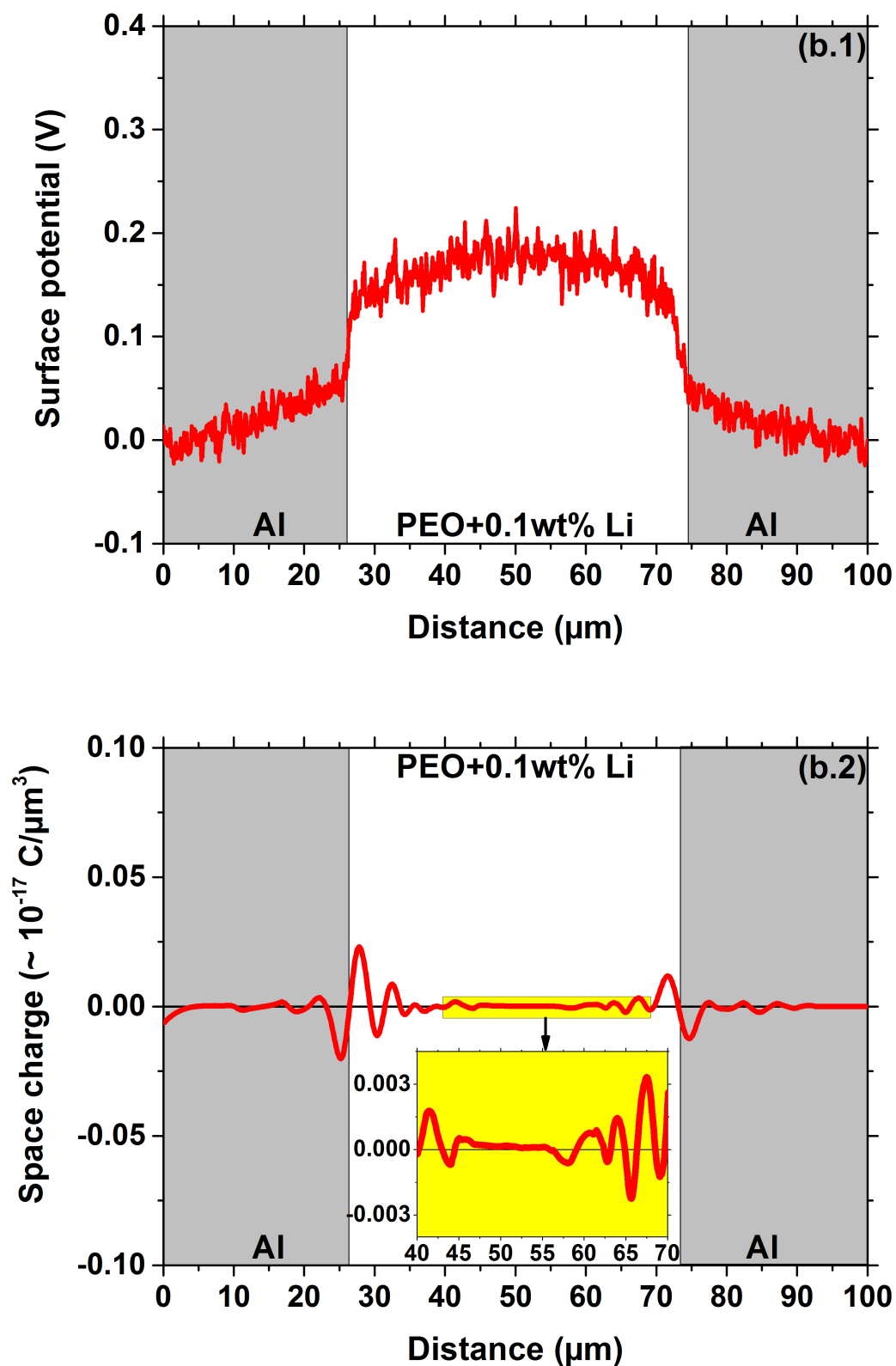
Figure 6.2: Surface potential (b.1) and space charge distribution (b.2) for the PEO samples doped with $0.1wt\%$ $LiClO_4$ under short-circuited condition before application of the external electric field.

Charge oscillations are detected inside the material (see an enlarged exemplar in Fig. 6.1(a.2) and in Fig. 6.2(b.2)). It could be possible that the positive space charges pull negative ions towards them and vice versa. This could lead to the charge oscillations. The explanation is not complete because simultaneously a charge diffusion sets in. This may be the reason for the smaller positive charge region at the electrodes in the PEO sample with Li-salt in which higher mobilities for the charges are expected [13].
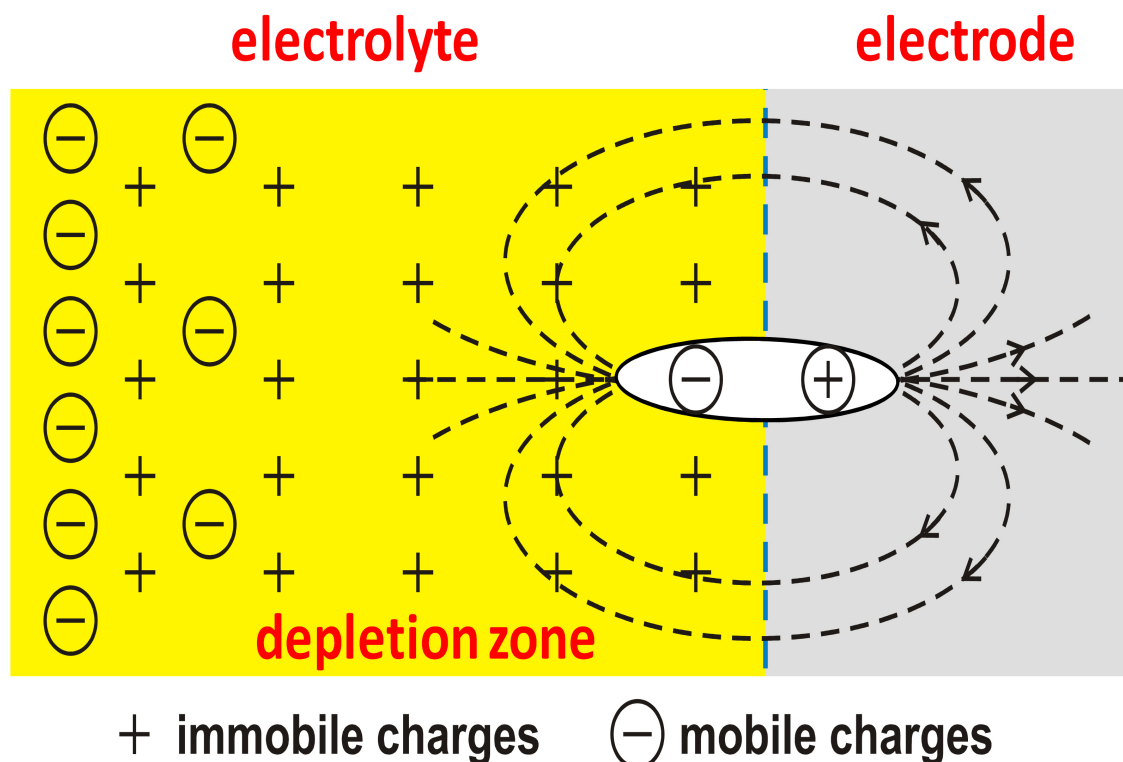
Figure 6.3: Dipole at the interface and depletion zone in the electrolyte.

From the viewpoint of the system's total energy, the appearance of charge oscillations seems to be reasonable. It is favorable for the system to produce local charge oscillations even in equilibrium since they decrease the system's energy [49]. To check this assumption, consider a charge distribution $\rho(x) = constant * sin(\frac{x}{\lambda})$ having a wavelength λ. The electric field distribution then is $E(x) = -constant * \lambda cos(\frac{x}{\lambda})$. The energy density $\eta(x)$ is

$$\eta(x) = \frac{1}{2}\varepsilon E^2(x) \sim \lambda^2 cos^2\left(\frac{x}{\lambda}\right) \tag{6.1}$$

thus decreases with the square of the charge distribution's wavelength.

In Fig. 6.4(a) [49] two space charge oscillations with equal amount of positive and negative charges are assumed: an oscillation with a long wavelength $\lambda = 50\mu m$ and an oscillation with a shorter wavelength $\lambda = 25\mu m$. For both configurations the internal electrostatic energy density
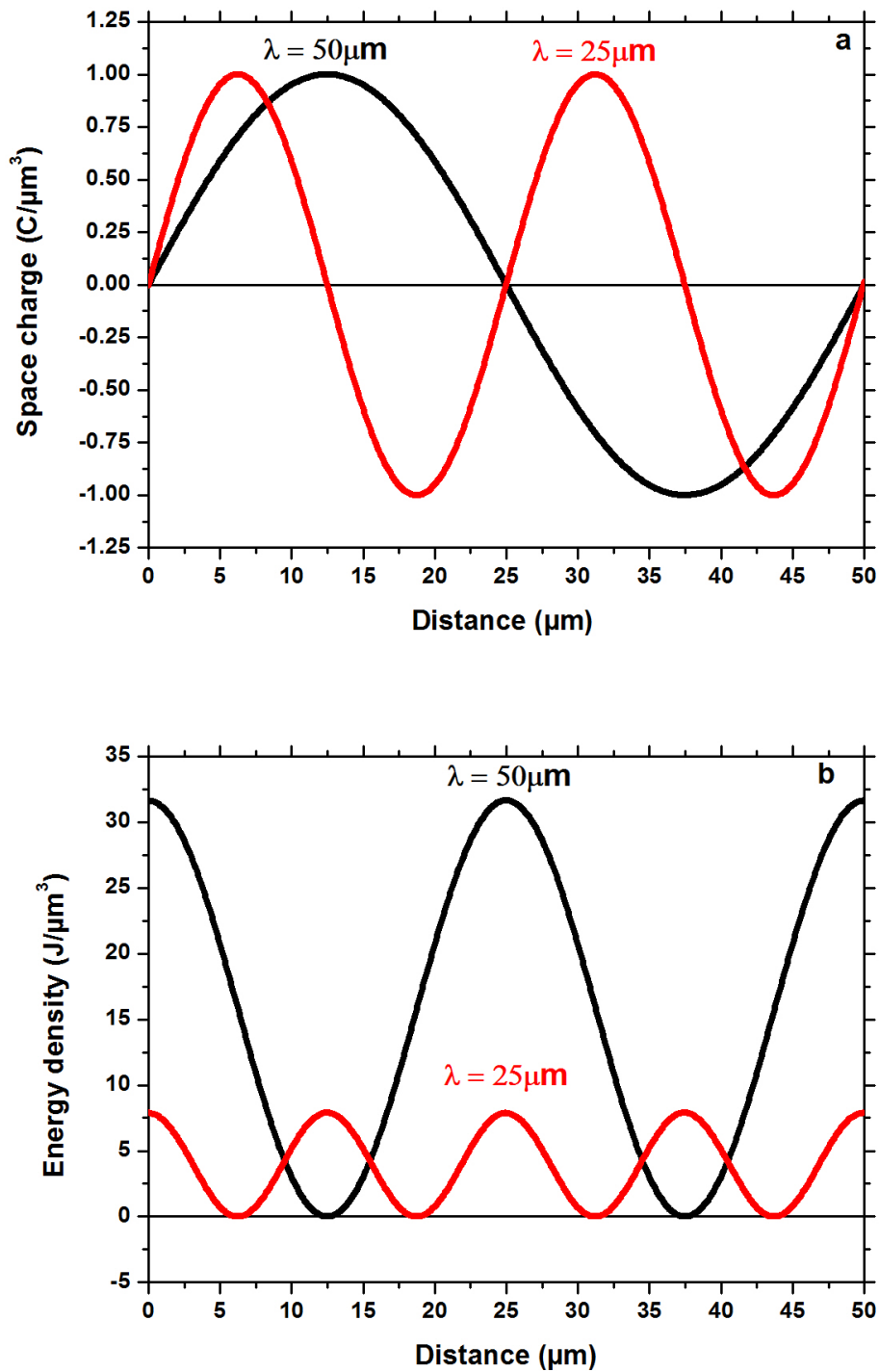
Figure 6.4: Assumed space charge (a) and energy density (b) distribution

is computed (see Fig. 6.4(b)) [49]. It is seen that the shorter wavelength has the lower energy density. Thus the oscillation is energetically favored compared to a constant charge.

6.1.1 Effect of the distance between the electrodes on charge oscillations

It has already been mentioned in our former publication [14, 20] that the electrodes play an important role in the distribution of the internal potential in ion conducting polymers due to image charges. However, at that time we were unable to extract a charge distribution from a measured surface potential. Here, we have investigated the effect of the distance between two Al electrodes on the charge oscillations in the PEO sample. To perform this investigation, we have used a sample with Al-PEO-Al structure with varying distances between the Al electrodes. This sample structure is depicted in Fig. 3.3(B).

In order to check the effect of the electrodes on the charge oscillations, the surface potential measurements were done at two locations on the sample (Fig. 3.3(B)) with different distances between the two Al electrodes under an unbiased condition. Fig. 6.5 shows the surface potential profiles under the short circuit condition at two locations on the sample where the distances between the two electrodes are $34\mu m$ and $55\mu m$, respectively [64]. From Fig. 6.5, it can be seen that the mid-surface potential height is more or less unaffected by the distance between the two electrodes. Without any external field, the charge distributions are calculated from both surface potential profiles shown in Fig. 6.5.

The calculated charge distribution profiles are depicted in Fig. 6.6 [64]. In both charge distribution profiles, positive space charges are detected in the PEO near the Al electrodes and induced negative space charges are detected on the Al electrodes at the Al/PEO interfaces. Charge oscillations are detected in the volume of PEO.

Here, one thing can be said for sure that the charge oscillations are significantly affected by the distance between the two electrodes. It can be seen from Fig. 6.6(a) and 6.6(b) that the formation of charge oscillations inside the volume of the PEO is decreasing as the distance between the electrodes is increasing.

The oscillations here seem to be caused by the electrodes with the charges in the material and images in the electrodes. This occurrence can be deemed as further indication that the charge oscillations found in PEO are a real physical phenomenon of the material and not an artifact from the calculation procedure.

The reason to conclude this, is as follows: The level of noise is the same in both set of potential data (Fig. 6.5(a) and 6.5(b)). So we expect that the level of oscillations would be the same if they are originated by the noise and/or the algorithm. Yet, even though the level of noise is in fact the same in both sets of potential data, the results shown in Fig. 6.6 reveal that the oscillations in the sample with the distance $55\mu m$ between the two electrodes are less as compared to the sample with the distance $34\mu m$ between the two electrodes.
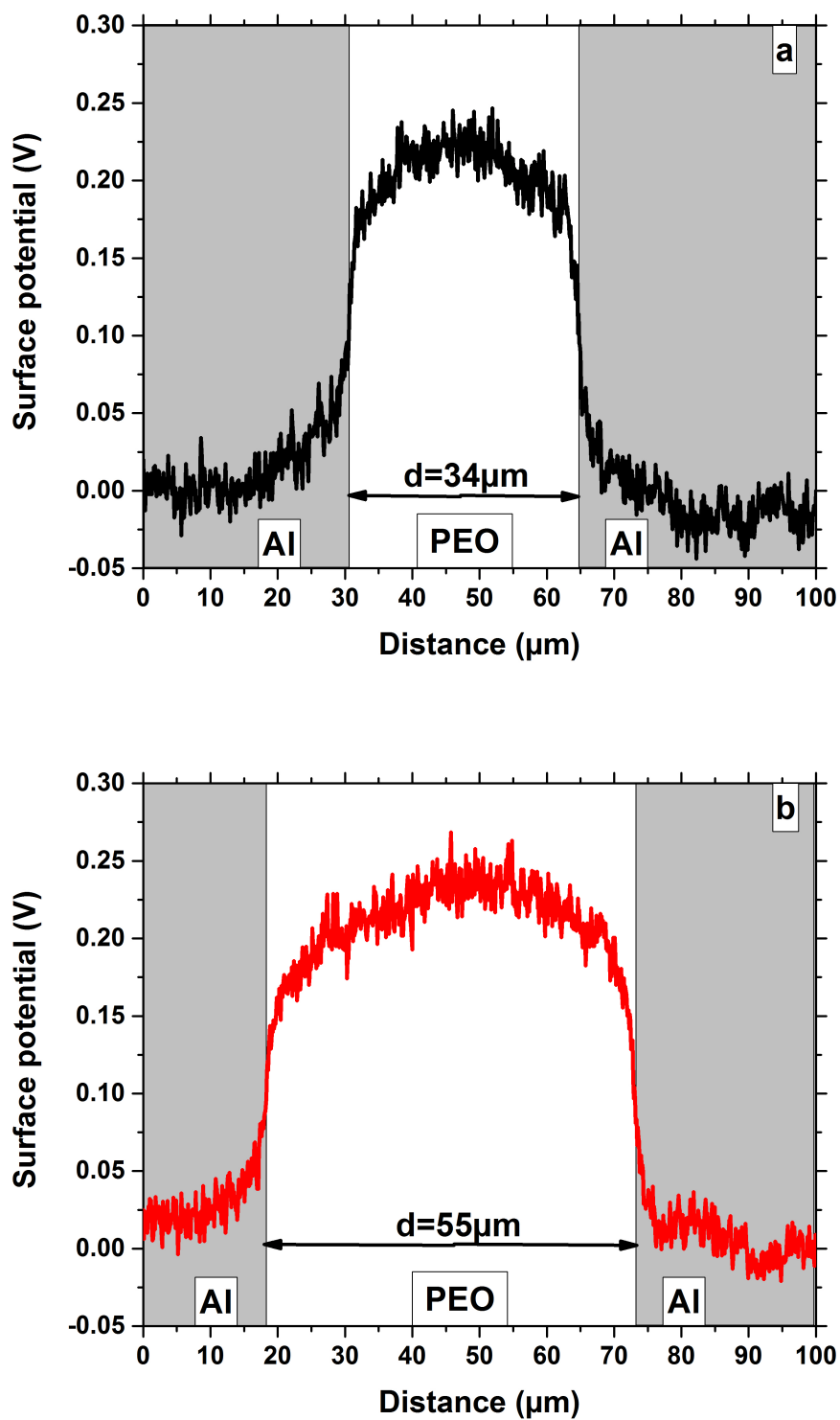
Figure 6.5: Surface potential at d = $34\mu m$ (a) and d = $55\mu m$ (b) under the short-circuit condition.
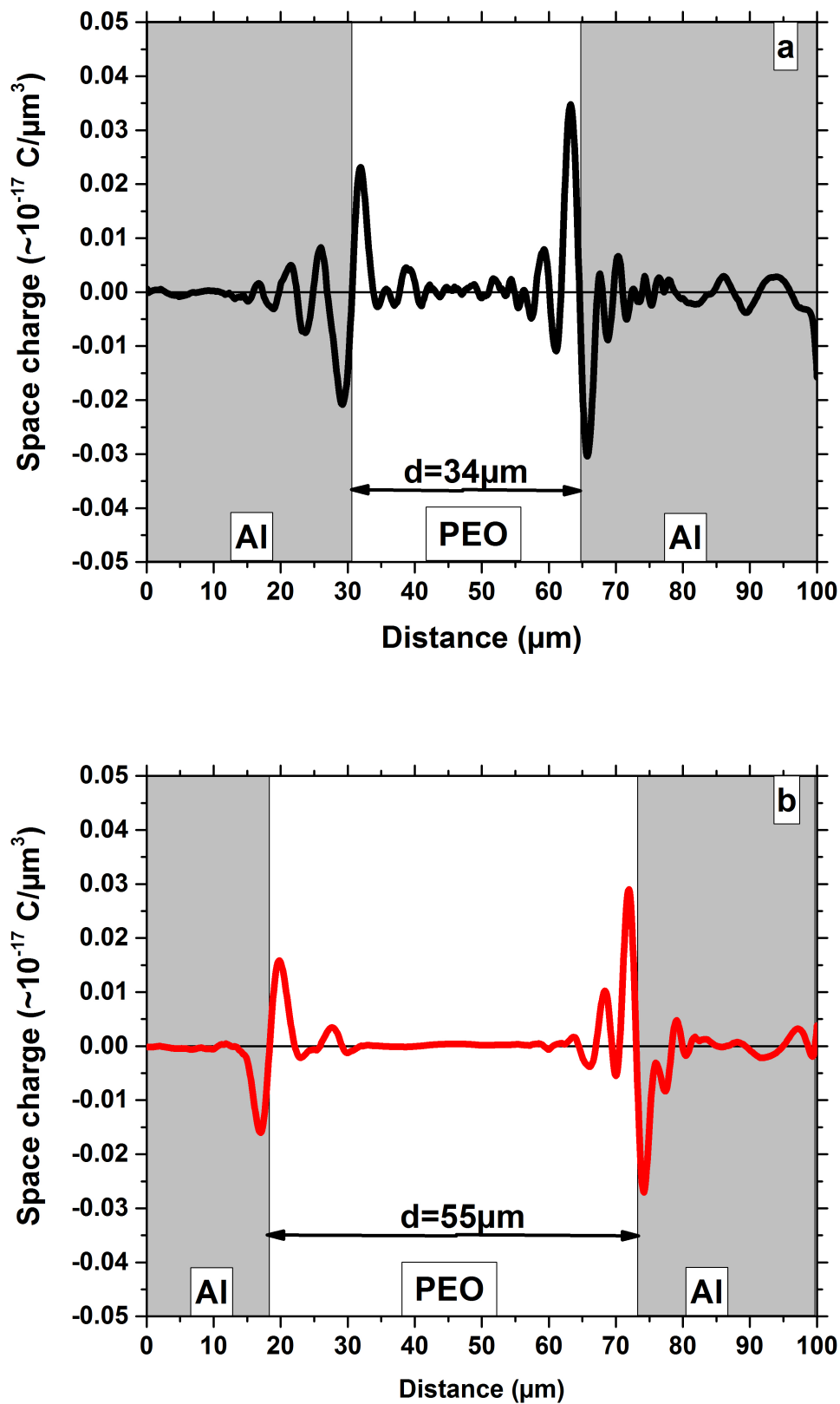
Figure 6.6: Space charge at d = $34\mu m$ (a) and d = $55\mu m$ (b) under the short-circuit condition.

6.2 Comparison during application of an external electric field

To understand the formation and the movement of the charges inside the volume and at the interface region of the samples, an external field of $0.6\frac{MV}{m}$ was applied for $590s$ and the transient formation of the internal potentials was measured at four different moments in time on the same line along the sample surface. The potential profiles were recorded at $10s$, $60s$, $300s$ and $590s$ after application of the electric field.

Fig. 6.7(a.1) and Fig. 6.8(b.1) show the surface potential profiles at four different moments ($10s$, $60s$, $300s$ and $590s$) in time on lines along the sample surface for both type of samples [49, 63]. The transient formation of the potential distribution between the pure PEO and the Li-doped PEO sample is significantly different. $10s$ after application of the voltage we find for both samples a spatially constant potential at the positive electrode which drops down in the volume. This is in line with the observations reported in [19]. Because of the higher speed of the measurement system we can now observe the transient formation of the potential. The potential's drop is shifted in time towards the negative electrode. This shift is more pronounced in the doped sample with the higher ion mobility and concentration.

Fig. 6.7(a.2) and Fig. 6.8(b.2) depict space charge distribution profiles calculated from the potential profiles [49, 63]. In general the space charge oscillations are significantly larger in the case of the doped sample. Apart from the charge oscillations a positive charge packet marked with arrows (see an enlarged exemplar in Fig. 6.7(a.2) and in Fig. 6.8(b.2)) has been detected where the potential drops down. It travels towards the negative electrode and it has a higher speed in the doped sample.

However, the speed of the positive charge packet decreases with time in both type of samples. This can be seen in Fig. 6.9. It can be seen from Fig. 6.9 that the speed of the positive charge packet recorded at $60s$ after application of the electric field in both types of samples drops significantly and then drops slowly. The decreasing speed of this positive charge packet indicates that the electrical mobility of this positive charge packet is not constant but decreasing during application of the electric field as the time passes. The reason for this might be that the positive charge packet feels a strong repulsive force from the positive charges which were accumulated at the negative electrode. As the accumulation of the positive charges at the negative electrode increases with time, the repulsive force exerted on the positive charge packet due to the accumulated positive charges at the negative electrode increases as well. That's why, the positive charge packet traveling towards the negative electrode is slowed down during application of the electric field as time passes.

The space charge oscillations are clearly perceptible in the front of the positive charge packet. These oscillations disappear behind the positive charge packet as it moves towards the negative electrode. The potential behind the packet is almost constant. At the negative electrode, a negative charge peak appears which can be an injected charge (see an enlarged exemplar in Fig. 6.7(a.2) and 6.8(b.2)). This negative charge peak at the negative electrode increases in time in the pure PEO sample. But in the doped PEO sample it increases from $10s$ to $300s$ and decreases later. This is possible because the injected charges are partly compensated in time by positive ions from the volume which are attracted by the negative electrode. The nature of charges is difficult to identify with this technique. But we can assume that in the

Figure 6.7: Surface potential (a.1) and space charge distribution (a.2) for undoped PEO samples during application of an external electric field of $0.6\frac{MV}{m}$.

Figure 6.8: Surface potential (b.1) and space charge distribution (b.2) for the PEO samples doped with $0.1wt\%$ $LiClO_4$ during application of an external electric field of $0.6\frac{MV}{m}$.
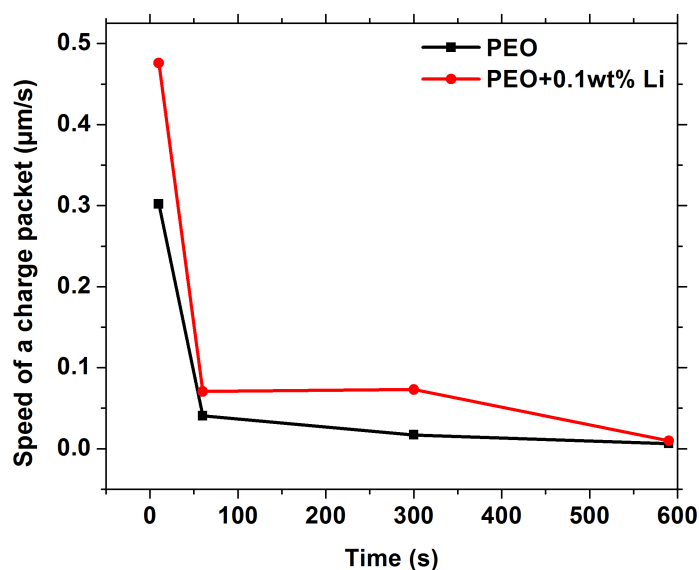
Figure 6.9: Speed of the positive charge packet in the pure PEO samples and the PEO samples doped with $0.1wt\%$ $LiClO_4$ during application of an external electric field of $0.6\frac{MV}{m}$.

undoped PEO sample unbonded H^+ and OH^- ions play a role in the ion conduction and in the doped PEO sample Li^+ and ClO_4^- ions mainly play a role in the ion conduction.

Fig. 6.10(a) and (b) depict electric field distributions for the pure PEO sample and the PEO sample doped with Li salt respectively. It can be seen from Fig. 6.10(a) and (b) that the electric field at the region near negative electrode is significantly higher in the doped PEO sample than it is in the pure PEO sample. This high electric field at the region near negative electrode in the doped sample is mostly due to mobile Li^+ ions. The electrical field (see Fig. 6.10(b)) at the region near negative electrode in the doped sample increases over time because the accumulation of Li^+ ions at that region near negative electrode in the doped sample increases over time during the applied external electric field (see Fig. 6.8(b.2)). The increasing electric field at the region near negative electrode in the pure PEO sample can be seen as well. But, as the pure PEO does not have access amount of positive ions as it is in the case of the doped sample, the increment in the electric field at the region near negative electrode in the pure PEO sample is not as significant as it is in the doped PEO sample.

Above and along the negative electrode we find a significant potential tail which is due to the non-zero lift height of the cantilever. This is discussed in Chapter 4. Also the charges inside the material have an impact on this potential drop. This can be seen by comparing the surface potential profiles for the doped sample (see Fig. 6.8(b.1)) and for the undoped sample (see Fig. 6.7 (a.1)). The potential drop increases as the number of positive charges increases with time at the interface of the negative electrode. In the doped sample, this effect is more significant than in the undoped sample. So we see that at the interface, inaccuracies in the space charge computation can not be avoided so far.
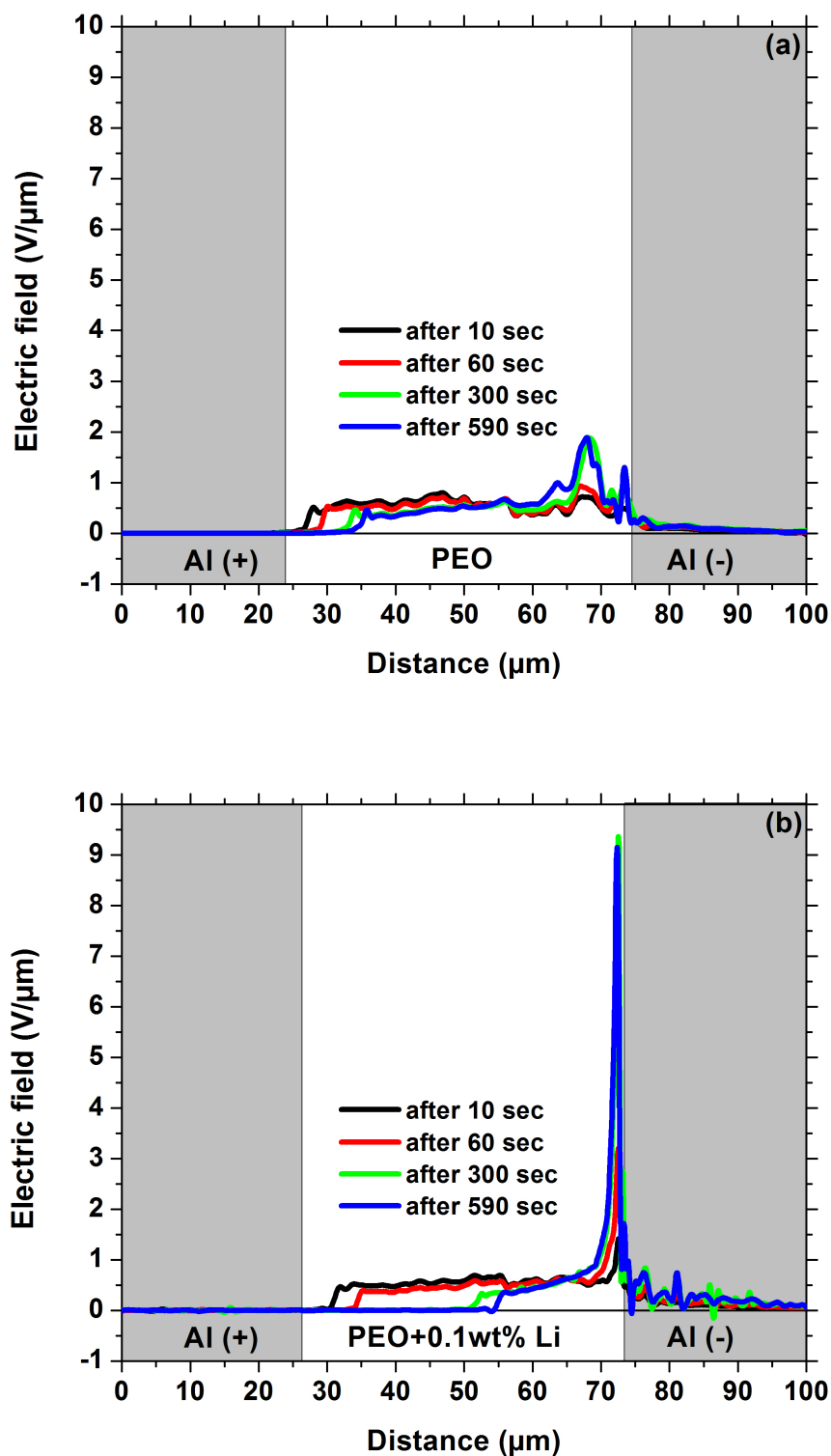
Figure 6.10: Electric field for undoped PEO samples (a) and electric field for the PEO samples doped with $0.1wt\%$ $LiClO_4$ (b) during application of an external electric field of $0.6\frac{MV}{m}$.

6.2.1 Effect of an external voltage on charge oscillations

In this section, the impact of an applied external voltage on the charge oscillations is investigated. The Al-PEO-Al sample with the type 1 structure (see Fig. 3.3(A)) is used. We have applied $1V$, $4V$ and $8V$ on the sample and measured the surface potential profiles $30s$ after the application of the external voltages. Fig. 6.11(a) shows the potential profiles at different voltages. The calculated charge distributions from these potential profiles are shown in Fig. 6.11(b).

From the results shown in Fig. 6.11, it is clear that the charge oscillations (Fig. 6.11(b)) are increased by increasing the applied voltage (Fig. 6.11(a)). Since the KPFM measurement system has a high resolution, we can detect oscillations in the potential's decent (see an enlarged exemplar in Fig. 6.11(a)). These oscillations in the potential's decent give clear indication of the charge oscillations in the volume of the PEO. The charge oscillations shown in Fig. 6.11(b) have an increased magnitude with increased voltage but they are almost fixed at the particular locations in the PEO. This effect also confirms that the charge oscillations in the PEO are physically existent. If these oscillations were due to the noise in the data, this effect could not be expected.

6.3 Comparison after application of an external electric field

In this section, the behavior of the surface potential and space charges after removal of the applied external field of $0.6\frac{MV}{m}$ for both types of samples is investigated and described. Fig. 6.12 and Fig. 6.13 show the transient potential profiles and their related charge profiles for undoped and doped samples after application of the external field respectively [49, 63].

During the applied electrical field, positive charges appeared at the negative electrode (Fig. 6.7(a.2) and 6.8(b.2)) which are found also after switching off the field for both types of samples at the right side, the side negative before (see an enlarged exemplar in Fig. 6.12(a.2) and 6.13(b.2)). This peak of positive charges is due to positive ions which moved towards the negative electrode. These ions diffuse back into the volume and therefore, they are seen to be decreasing slowly in time. The injected electrons which had been seen during the applied field at the region near the negative electrode (see an enlarged exemplar in Fig. 6.7(a.2) and 6.8(b.2)) have now left because of their higher mobility than the ion's mobility (see an enlarged exemplar in Fig. 6.12(a.2) and 6.13(b.2)). On the other side, the side positive before, we see the gathered negative charges (see an enlarged exemplar in Fig. 6.12(a.2) and 6.13(b.2)) which have travelled towards the electrode during application of the external field. These charges diffuse in time into the volume of the material and leave behind positive immobile charges which indicate the system returns to equilibrium (see Fig. 6.1(a.2) and 6.2(b.2)). The induced positive image charges in the Al on the left side can be seen. These induced positive charges decrease in time (see an enlarged exemplar in Fig. 6.12(a.2) and 6.13(b.2)) and finally turn into negative charges. Also in both types of samples, the charge oscillations are reduced in time since the attraction towards negative charges also slows down.
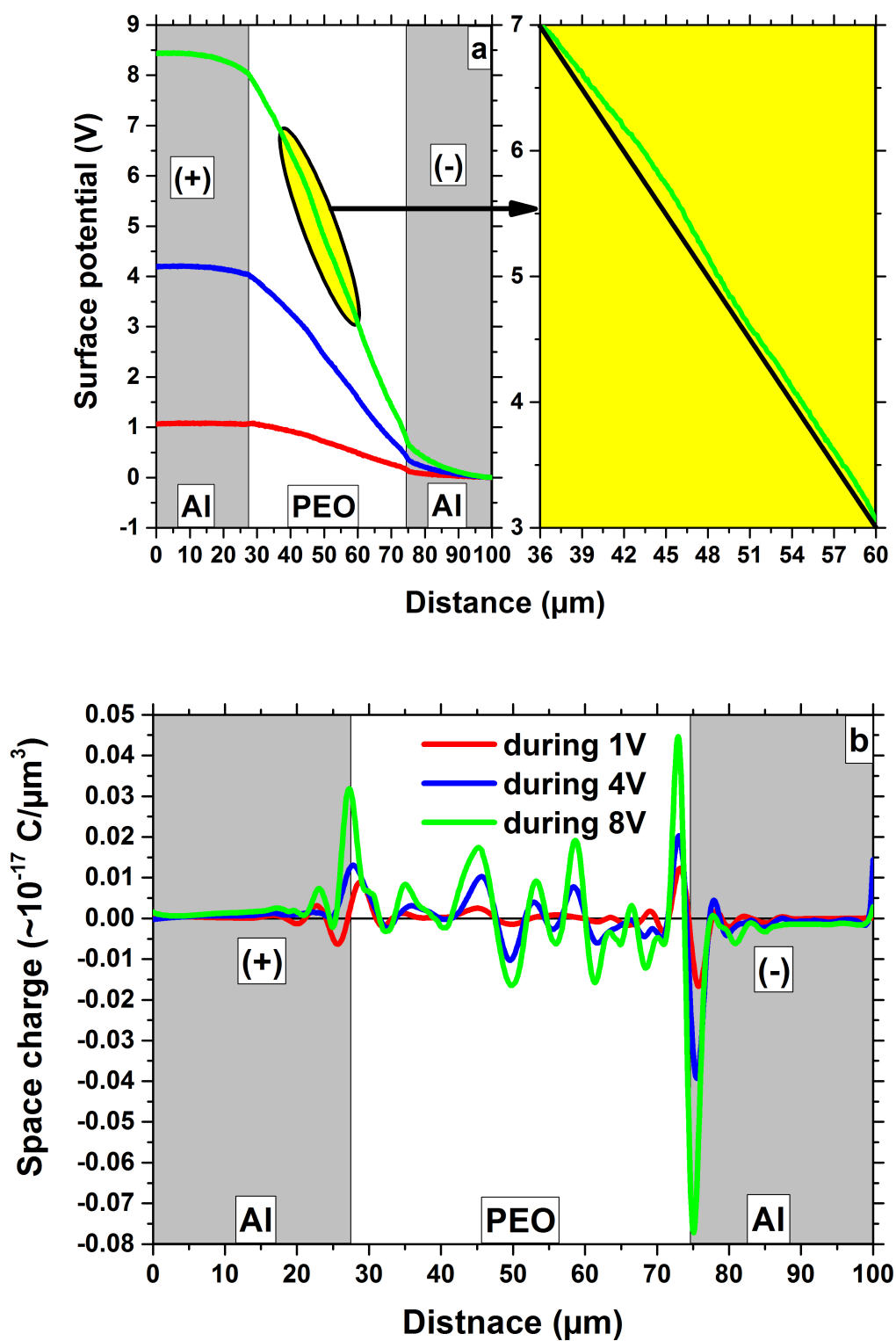
Figure 6.11: Surface potential (a) and Charge distribution (b) $30s$ after application of the external voltage of $1V$, $4V$ and $8V$.
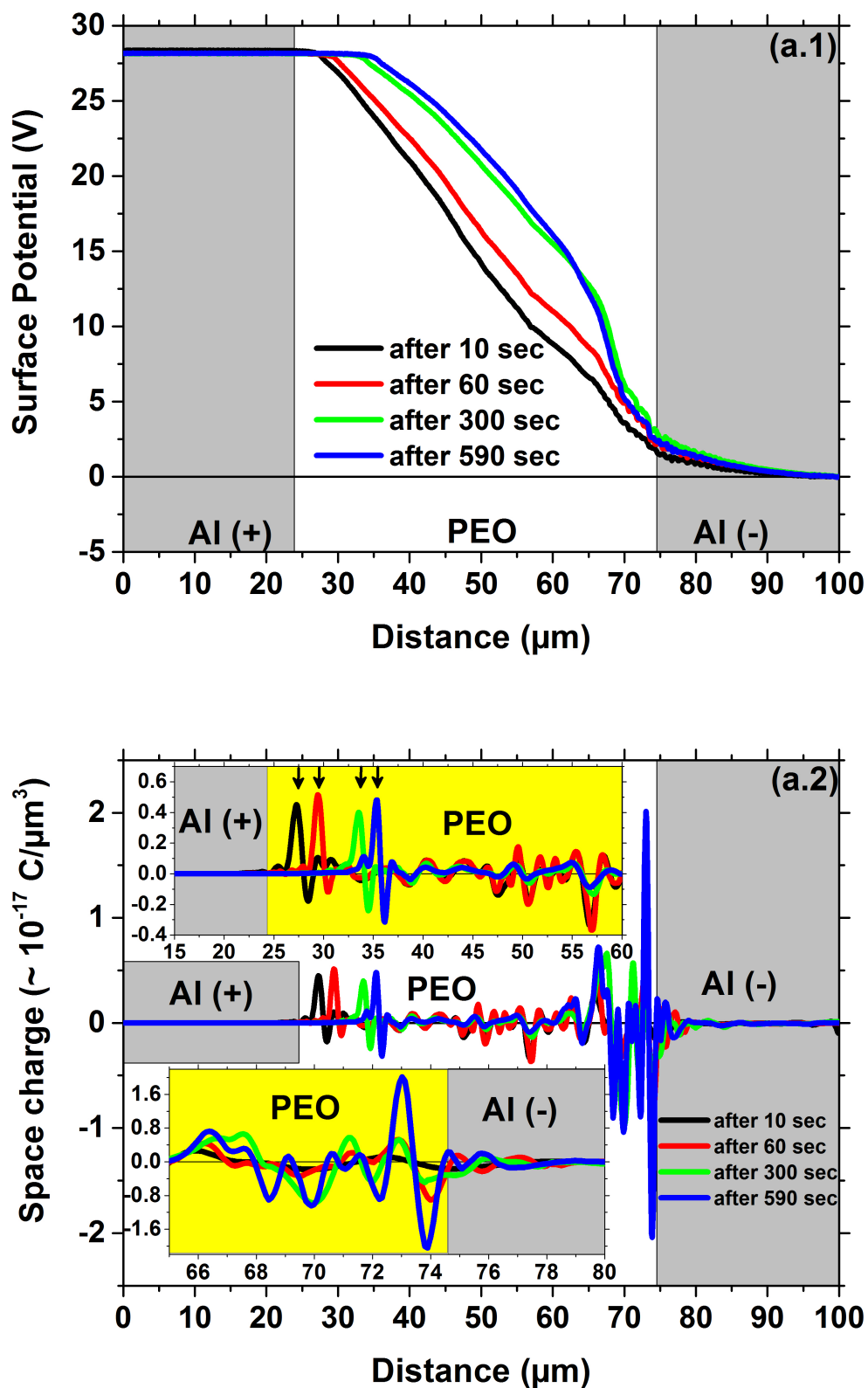
Figure 6.12: Surface potential (a.1) and space charge distribution (a.2) for undoped PEO samples after application of the external electric field of $0.6 \frac{MV}{m}$.
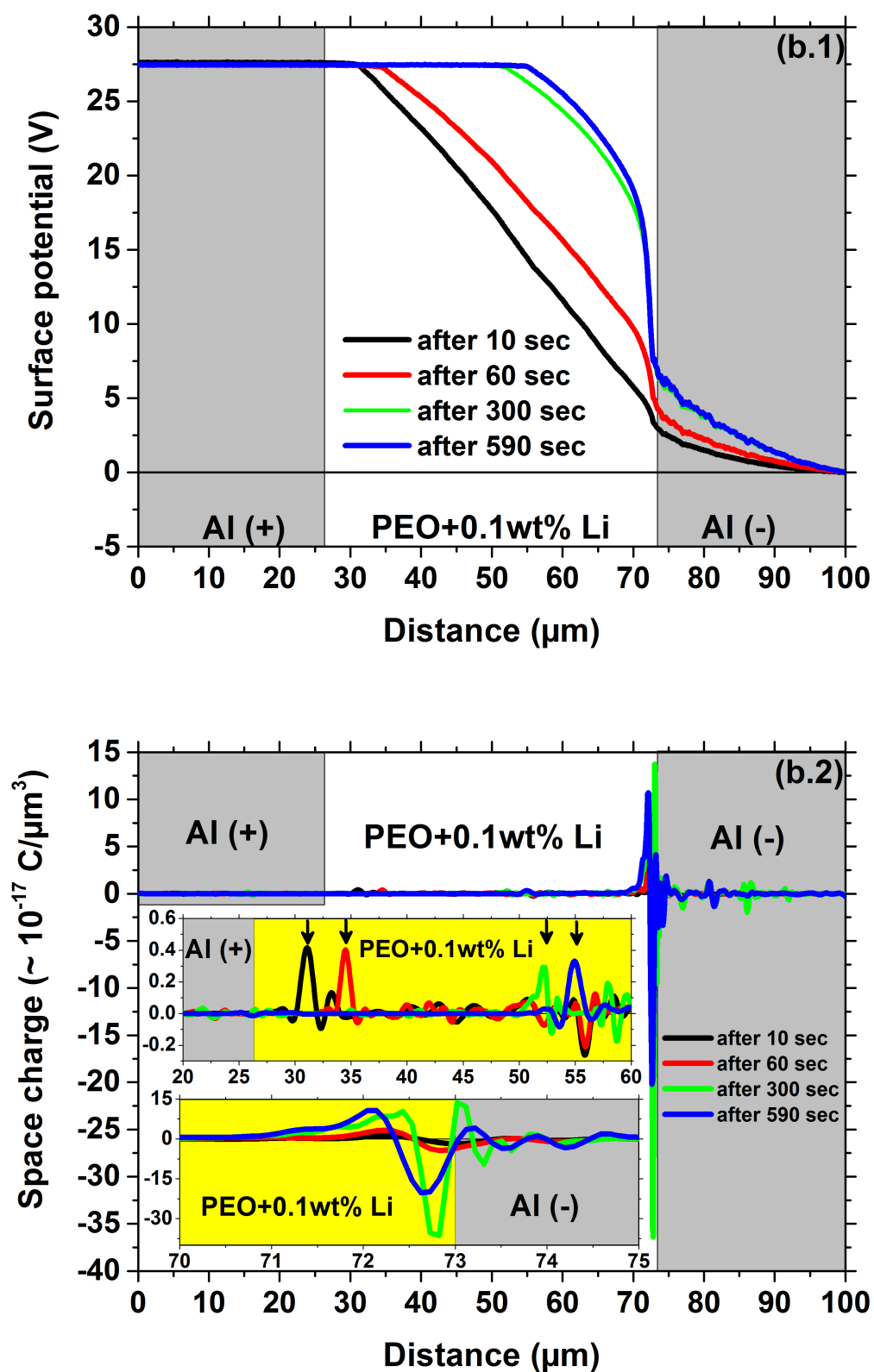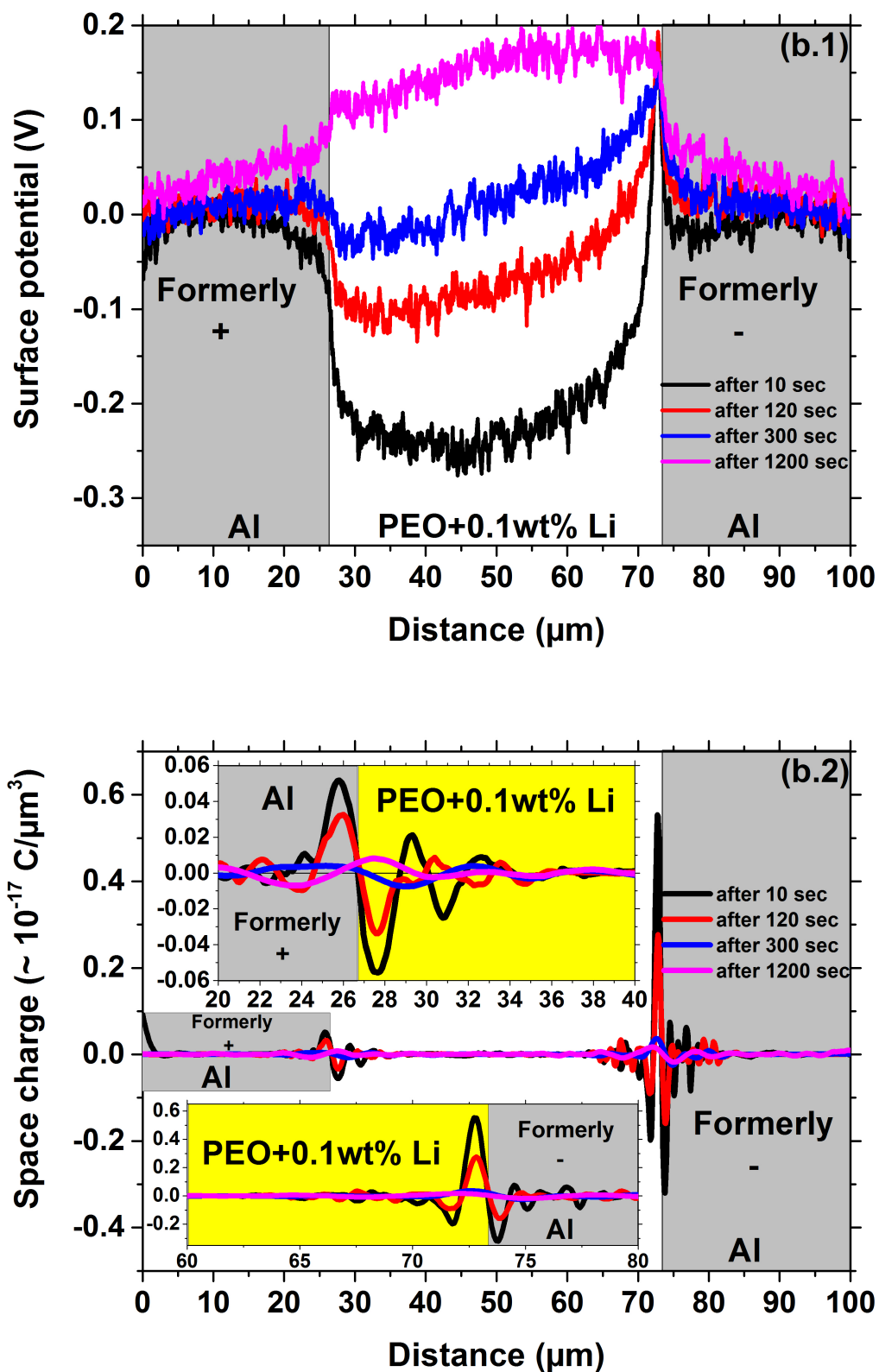
Figure 6.13: Surface potential (b.1) and space charge distribution (b.2) for the PEO samples doped with $0.1wt\%$ $LiClO_4$ after application of the external electric field of $0.6\frac{MV}{m}$.

6.4 Simulation and model consideration
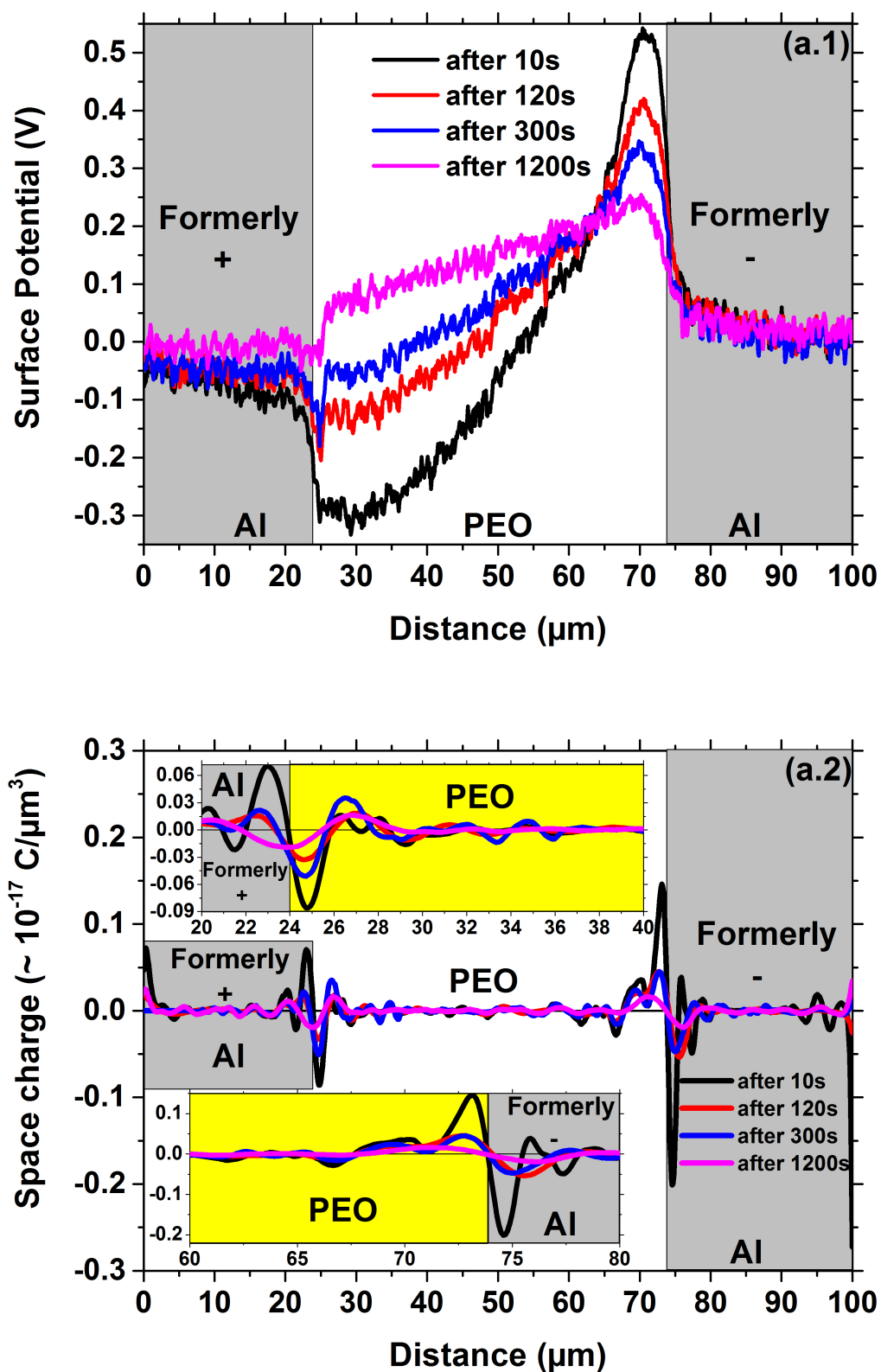
In last sections, we have seen that space charge oscillations and a positive charge packet are detected in the undoped PEO samples and the samples doped with Li-salt under both biased and unbiased conditions. These local dynamic charge oscillations and a development of a moving positive charge packet have been detected for the first time in SPEs. These new phenomena should be understood and interpreted by a mathematical model and simulation technique. This will help to understand the role of these charge oscillations and charge packets in the ion conduction process in SPEs. The ion conduction process in a SPE is complex because many factors are involved into the conduction mechanism. For example, these factors are space charge polarization of internal charges, injected charges, electrons and defect electrons, surface charges, image charges on electrodes etc.. These charges interact with each other at least by their Coulomb fields. The interaction between all these charges has a significant effect on the conduction process and also on the formation of transient and stationary internal potentials in SPEs. That is why, it is important to understand the role of these charge oscillaitons and charge packets in SPEs.

The model development and simulation work of my former colleagues gives some potential explanation of charge oscillations. They have proposed a three dimensional hopping model [13, 14]. Some of their work is presented here for comparing experimental results and simulated results of charge distribution in PEO.

This model is based on the electrostatic interaction between positive and negative charges. In this model, single charges experience the externally applied electrical field, the coulomb fields between the carriers and the fields between charges in the electrolyte and image charges in the electrodes. Charges attracted to the electrodes form with their image charges dipoles at the interface. Their field repels further movable charges into the volume of the sample. Therefore behind the charge layer at the electrodes a depletion zone builds up [13, 14]. With the help of this model, the charge distribution in the electrolyte can be calculated and shall be compared to the experimentally detected one.

The mechanism described in section 6.1 (see Fig. 6.3) is considered for the three dimensional hopping model. In this mechanism, mobile negative ions are attracted to the electrodes and at the interface they form dipoles with the positive image charges in the electrode with dipole length of atomic distances. These double layers repel with their fields further negative ions and shift them into the volume of the sample. Thus, a depletion zone of negative ions is formed close to the interface. Only positive immobile charges remain in the depletion zone. This can be seen in Fig. 6.1(a.2) and 6.2(b.2) as the first positive space charge peak which gives rise to a mid-surface potential. The double layers with atomic dimensions at the interfaces do not contribute significantly to the surface potential.

To simulate this mechanism, the three dimensional hopping model was constructed in which only negative ions can move and positive immobile background charges adjust charge neutrality. Fig. 6.14 is a one dimensional representation of the three dimensional model. The electrolyte is subdivided into cells which are separated from each other by barriers of height W_0. The cells are constructed on a cubic lattice first. Then the centers of the cells are shifted randomly with a Gaussian distribution by small amounts in x, y and z direction. The barrier heights W_0 are assumed to be proportional to the distances between the cell centers. Thus a
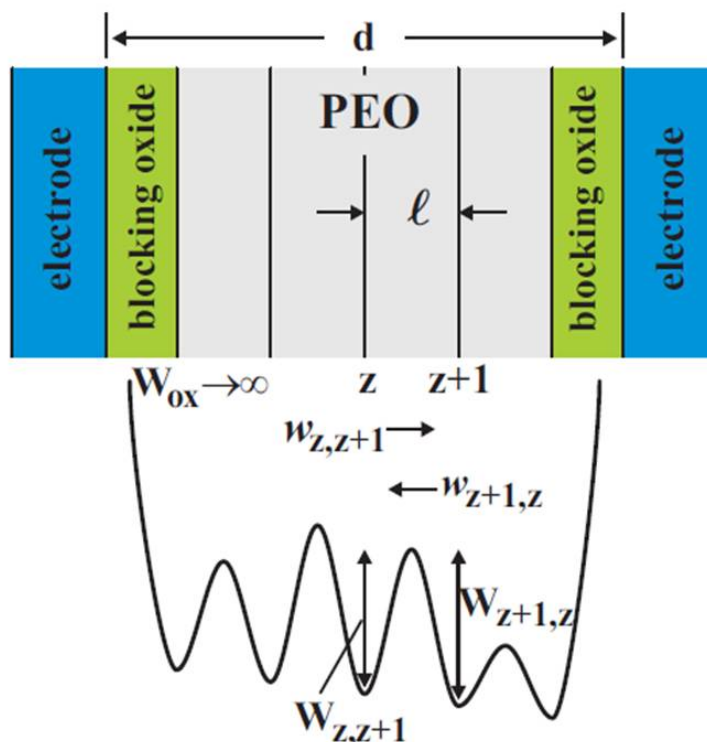
Figure 6.14: A one dimensional representation of the three dimensional model.

distribution of W_0 results. Ions can fluctuate between the cells by thermal activation. The electrolyte is separated from the electrodes by blocking layers impermeable for ions.

For a thermally activated jump from one cell to a neighbored cell, an ion has to surmount an effective barrier height W_{eff} consisting of the intrinsic part W_0, an interaction term $\dfrac{\Delta W}{2}$ and a term due to an external applied field $\dfrac{\delta W}{2}$. In the interaction term all Coulomb interactions between the ions, between the ions and the immobile background charge and between the ions and their image charges in the electrodes are considered. From the effective barrier heights the thermally activated transition rates $w_{i,j}$ are calculated for each ion i in 6 possible directions j (k Boltzmann factor, T temperature, $\nu_0 = 10^{12}\ Hz$ the vibration frequency of the charges in the wells).

$$w_{i,j} = \nu_0 \cdot exp\left\{\frac{-W_{eff}}{kT}\right\} = \nu_0 \cdot exp\left\{\frac{-W_0}{kT} \pm \frac{\Delta W}{2kT} \pm \frac{\delta W}{2kT}\right\} \qquad (6.2)$$

The main input parameter W_0 is estimated from the temperature dependent measurements as $W_0 = 0.7eV$ [13, 18].

From these deterministic hopping rates for a jump from one well to another the transition times t are calculated with a dynamic Monte Carlo step.

$$t_{i,j} = -\frac{1}{w_{i,j}} ln(x) \tag{6.3}$$

x is a random number from the interval $]0, 1]$. Thus the time for a jump is composed of a deterministic weight $w_{i,j}$ and a probabilistic weight x. Only the ion with the shortest transition time t_{min} jumps in the appropriate direction. Then, the total system time is increased by t_{min} and the algorithm restarts by calculation of the interactions for the new charge distribution. In this way the time dependent behavior of the system is computed.
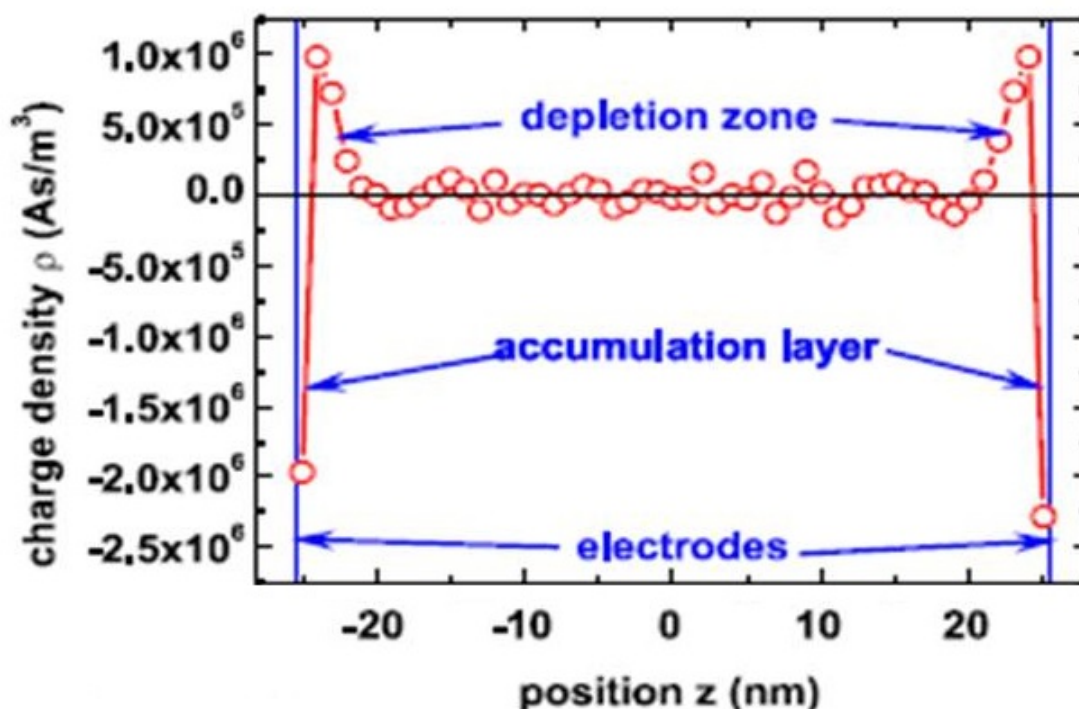
Figure 6.15: Simulated charge distribution without an external voltage applied.

According to the algorithm explained above the ions are attracted towards the electrodes and accumulate at the blocking layer. They form with their images in the electrode dipoles which reject with their fields further negative ions into the volume. A depletion zone results due to the immobile background charge. A simulated charge distribution and surface potential distribution resulting from the simulated charge distribution without an external voltage applied are shown in Fig. 6.15 and 6.16 respectively.

From Fig. 6.15, we see the negative charges attracted to the electrodes and towards the volume we find the positive background charge. The negative charge peaks at the electrodes blocking layer are produced by the movable negative ions. They repel further negative ions and the positive background charge gives rise to the positive peaks. This is analogous to the experimental results (see Fig. 6.1(a.2) and 6.2(b.2)). Integration along the depletion zone gives rise to a potential maximum in the center of the sample. That is why, the potential maximum in the center of the sample detected by the experiment (see Fig. 6.1(a.1) and 6.2(b.1)) is comparable to the potential distribution resulted from the simulated charge distribution without an external
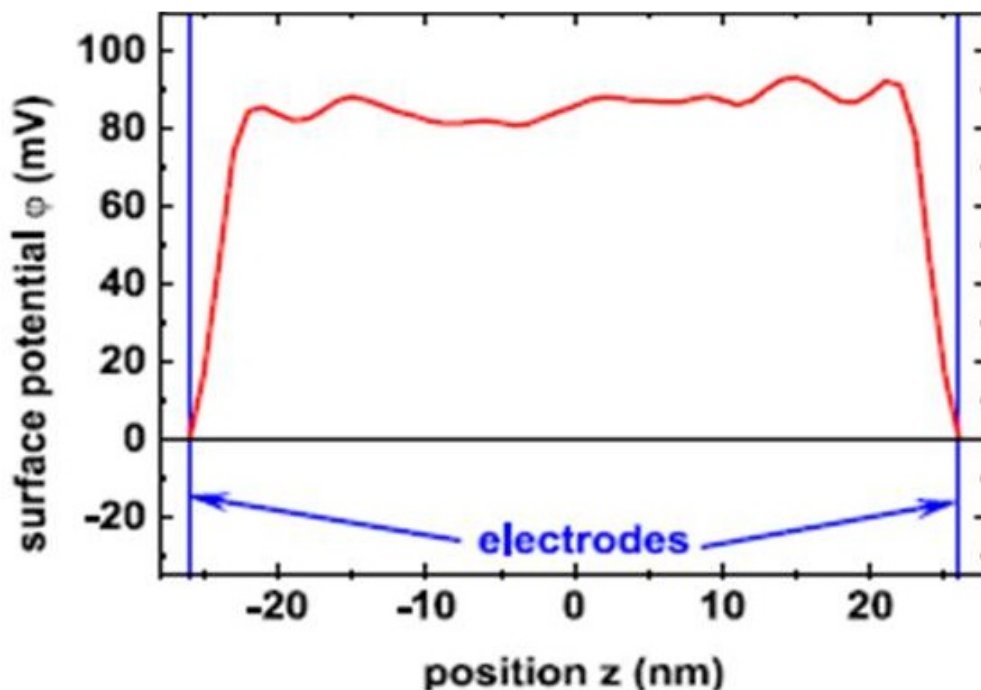
Figure 6.16: Surface potential distribution resulting from the simulated charge distribution.

voltage applied.

The simulated charge distribution seems to yield charge oscillations as it is detected in the experimental results (see Fig. 6.1(a.2) and 6.2(b.2)). However, these findings are not a complete proof of the charge oscillations but it leads us to the right direction.

To explain the charges oscillations, the charge packets as well as the electronic charge injection, the model has to be improved. Only the proposal for the improved model is described here.

Instead of only one moving species, now positive and negative ions as well as injected electrons can take part in the electrical transport process. To represent the electrolyte three cubic lattices between two electrodes are constructed with a typical size of $100 \times 100 \times 100$ knots for each grid. They are shifted against each other by a third of the lattice cell constant. Each knot represents a well or a trap for a charge. On each grid one species of charge can fluctuate. The wells are separated by barrier heights W_1 and W_2 for the ions and W_3 for the electrons. To introduce some disorder the positions of the wells are shifted with a Gaussian distribution in x, y and z direction. The barrier heights W_n (where, $n = 1, 2, 3$) are assumed to be proportional to the distances between the wells. Thus a distribution of barrier heights results. Further very high barriers, i.e. larger than $1.5eV$, or correspondingly deep wells can be introduced to represent deep traps for nearly immobile charges. At the interface between electrolyte and electrode a thin layer exists which is impermeable for ions, i.e. the barrier for ions is set infinitely high. But this barrier can be penetrated by electrons.

The former model (Fig. 6.14) is changed in the following way (Fig. 6.17): Electrons from the metal can be injected. They have to surmount a barrier W_{inj}, move inside the volume with W_3 and are extracted by surmounting W_{ext}. For positive and negative ions a blocking oxide

with an infinitely high barrier is assumed. From former simulations the lattice constant is assumed to be $1nm$ and the blocking layer thickness d_{bl} is $0.5nm$. The blocking layer thickness d_{bl} can be calculated from a capacitance measurement of a sample at low frequencies of about $1mHz$. At the low frequencies, the capacitance of the sample is found to be independent from the thickness d of the sample but it depends on the thickness d_{bl} of the blocking layer [18, 65].
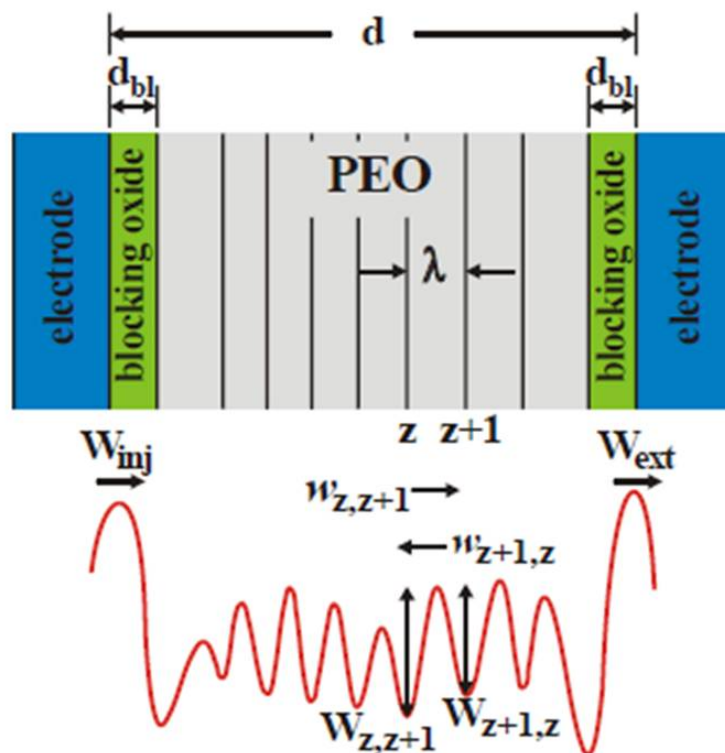
Figure 6.17: A one dimensional representation of the future three dimensional model. For electrons W_{inj}, W_{ext} are finite and for ions W_{inj}, W_{ext} are infinite.

All charges in the system interact to determine the potentials at the wells. The different barrier heights take into account different mobilities for the charges. From dielectric measurements and earlier simulations the value of $W_{1,2} = 0.7eV$ seems to be reasonable for the beginning. W_1 and W_2 can be changed if necessary. W_1 for the negative ions will be shifted towards higher values and W_2 for the assumed smaller positive ions can be shifted to lower values to get a higher mobility here. Electrons have to surmount $W_{inj} = 0.95eV$ from the electrodes for injection, their intrinsic barrier W_3 is assumed to be $0.65eV$ and the extraction barrier is $W_{ext} = 1.05eV$ for the start. These values brought about first results in previously published studies [21, 22, 23].

For the beginning, 1000 positive and 1000 negative ions are randomly distributed on the lattices. Interaction between all charges and the interaction between the charges in the electrolyte and the charges in the electrodes are considered by the method of images [14]. Deterministic hopping rates $w_{i,j}$ for a jump from one well to another can be calculated for each ion and for each injected electron counted with i in direction j.

$$w_{i,j} = \nu_0 \cdot exp \left\{ \frac{-W_n}{kT} \pm \frac{\Delta W}{2kT} \pm \frac{\delta W}{2kT} \right\} \tag{6.4}$$

The interaction term ΔW now considers electrons as well as the positive and negative movable ions. In each grid charges can hop in 6 directions and 6 transition rates for each charge are calculated. The actual transition time t again is comprised of the deterministic number $w_{i,j}$ and a random number $x \in]0, 1]$.

$$t_{i,j} = -\frac{1}{w_{i,j}} ln(x) \tag{6.5}$$

Only the charge with the shortest transition time t_{min} moves. Then the system's time is increased by t_{min}. The charge distribution is altered with this step and therefore new effective barrier heights result. The next jump can be calculated. In this way the time dependent behavior of the system is computed similarly to the algorithm described in earlier but now with 3 kinds of movable charges.

With the advanced model it should be possible to simulate the experiments described in section 6.1, 6.2 and 6.3, i.e. the appearance and movement of charge packets as well as the space charge oscillations.

Chapter 7

Charge distributions: comparison between pure PEO samples and PEO samples embedded with micro/nano-sized metal particles

For the first time, Weston and Steele [66] show that the mechanical strength of the polymer can be enhanced by incorporating electrochemically inert ceramic filler particles. After that, it has been demonstrated by several studies that the dispersal of ceramic filler particles in SPEs enhance significantly not only the mechanical strength but also the room temperature conductivity [67]. Up to now, a variety of SPEs containing filler particles have been studied. These fillers are inert oxide ceramics [68], treated SiO_2 [69], molecular sieves or zeolite [70], rare-earth ceramics [71], solid super acids [72], ferroelectric materials [73], carbon [74], cellulose nanocrystals [75] and active fillers [76]. So far, for PEO-based solid polymer electrolytes containing nano-sized inert oxide ceramic particles, the highest ionic conductivity of $3.8 \times 10^4 \frac{S}{cm}$ has been reported [67, 68]. But in this study, we have investigated PEO-based electrolytes with micro/nano-sized metal particles (i.e. Cu) with our proposed experimental approach. Because in the best of our knowledge, the SPEs with metal filler particles have not been studied yet [67, 77, 78, 79, 80]. This will be the starting point to look at the effect of metal particles on the charge distribution of SPEs during both biased and unbiased conditions.

To begin with, we have conducted some preliminary work. A sample of PEO with embedded $2.5wt\%$ Cu particles (average particle size 60 to 80nm from Chempur) was prepared. The type 1 sample structure shown in Fig. 3.3(a) is used in this experiment. To check the effect of Cu particles, we measured the surface potentials in both biased and unbiased conditions and calculated the charge distributions.

7.1 Comparison before application of an external electric field

Fig. 7.1 shows the potential profile and charge distribution in the Cu filled PEO sample. The mid-potential is lower than the one found in the undoped PEO sample (Fig. 6.1(a.1)) but nearly the same height as it is found in the Li-doped PEO sample (Fig. 6.2(b.1)). But surprisingly, the charge oscillations are significantly lower than those found in the doped and undoped samples (compare with Fig. 6.1(a.2) and 6.2(b.2)). In the Cu filled PEO sample,
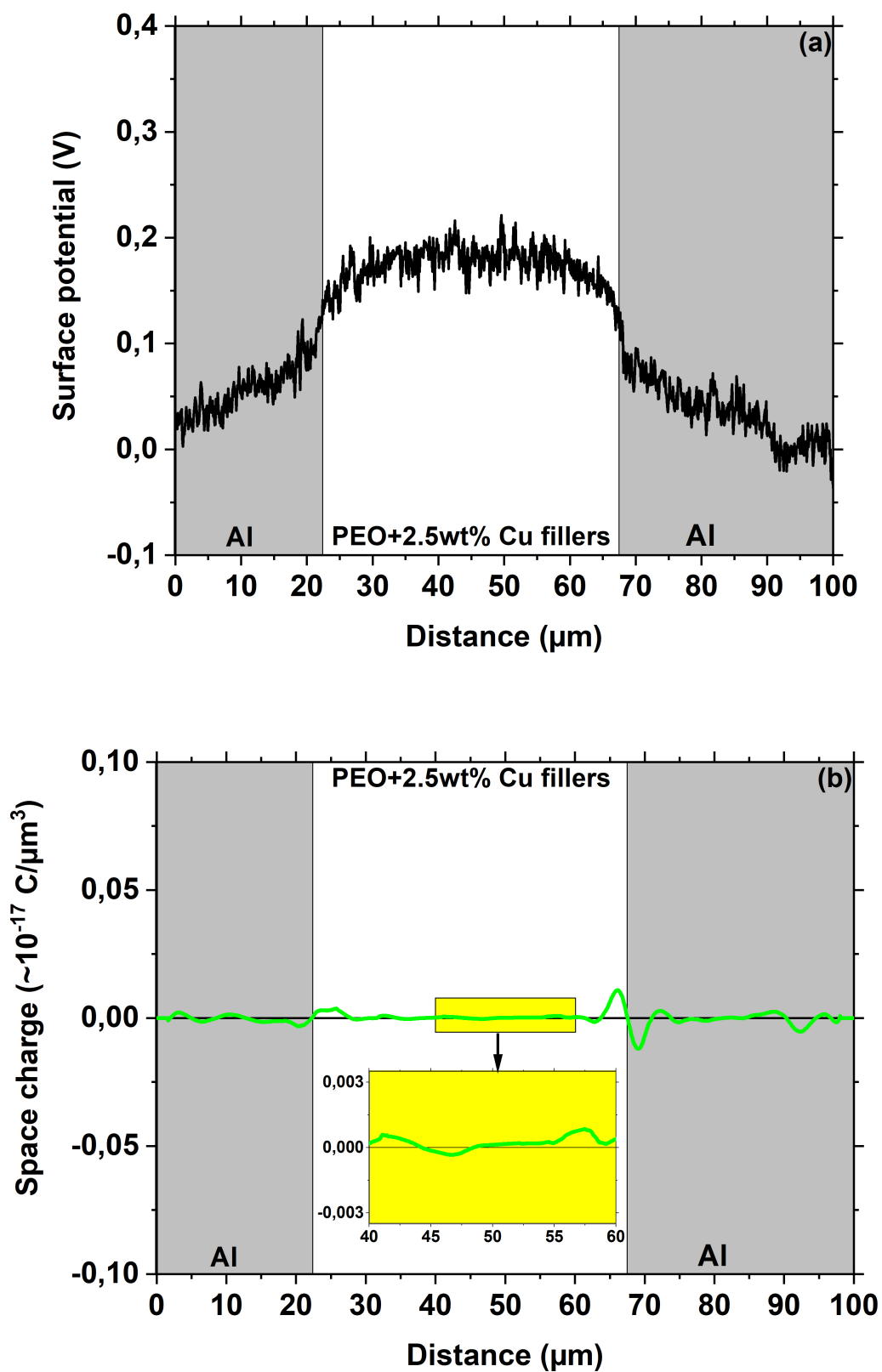
Figure 7.1: Surface potential (a) and space charge distribution (b) for the PEO sample embedded with $2.5 wt\%$ Cu particles under short-circuited condition before application of the external electric field.

positive space charges and negative induced space charges are detected respectively in the PEO and on the Al electrodes at the Al/PEO interfaces. These positive and negative charge regions are also smaller than the one found in the doped and undoped samples. This shows how Cu particles significantly influence the charge distribution in the material without any presence of an externally applied electrical field.

7.2 Comparison during application of an external electric field

To see the effect of the Cu particles under a biased condition, we have applied $28V$. $10s$ after the application of $28V$ we have recorded the surface potential profile to check the material behaviour with and without Cu particles. For the undoped PEO sample, the potential profile and the charge distribution are presented in Fig. 7.2 and for the PEO sample filled with Cu particles, the potential profile and the charge distribution are shown in Fig. 7.3.

By comparing the charge distributions of the undoped PEO sample and the PEO sample with Cu particles from Fig. 7.2 and 7.3, one can see that the formation of local charge oscillations is comparatively lower in the sample with Cu fillers. The shift of the potential's drop towards the negative electrode is also found in the Cu-filled sample as it was seen for the undoped PEO sample and the PEO sample doped with Li-salt (compare Fig. 7.3 with Fig. 7.2, 6.7 and 6.8). As seen in the doped and undoped PEO sample, the positive charge packet marked with an arrow found in the Cu filled PEO sample is traveling towards the negative electrode. The speed of the positive charge packet in the Cu filled PEO sample is found to be higher compared to the one detected in the undoped PEO sample and lower compared to the one detected in the Li-doped PEO sample.

The higher speed of the positive charge packet in the Cu filled sample indicates a higher conductivity of this sample compared to the undoped PEO sample. In order to check this, we have recorded the current flowing through the undoped and Cu filled samples. Fig. 7.4(a) and 7.4(b) show charge and discharge currents respectively flowing through the undoped and Cu filled PEO sample. From Fig. 7.4 it can be seen clearly that the current flowing through the sample with Cu fillers is higher than the current flowing through the undoped sample. This initial result shows the direct evidence of the improved conductivity of the PEO with Cu particles.
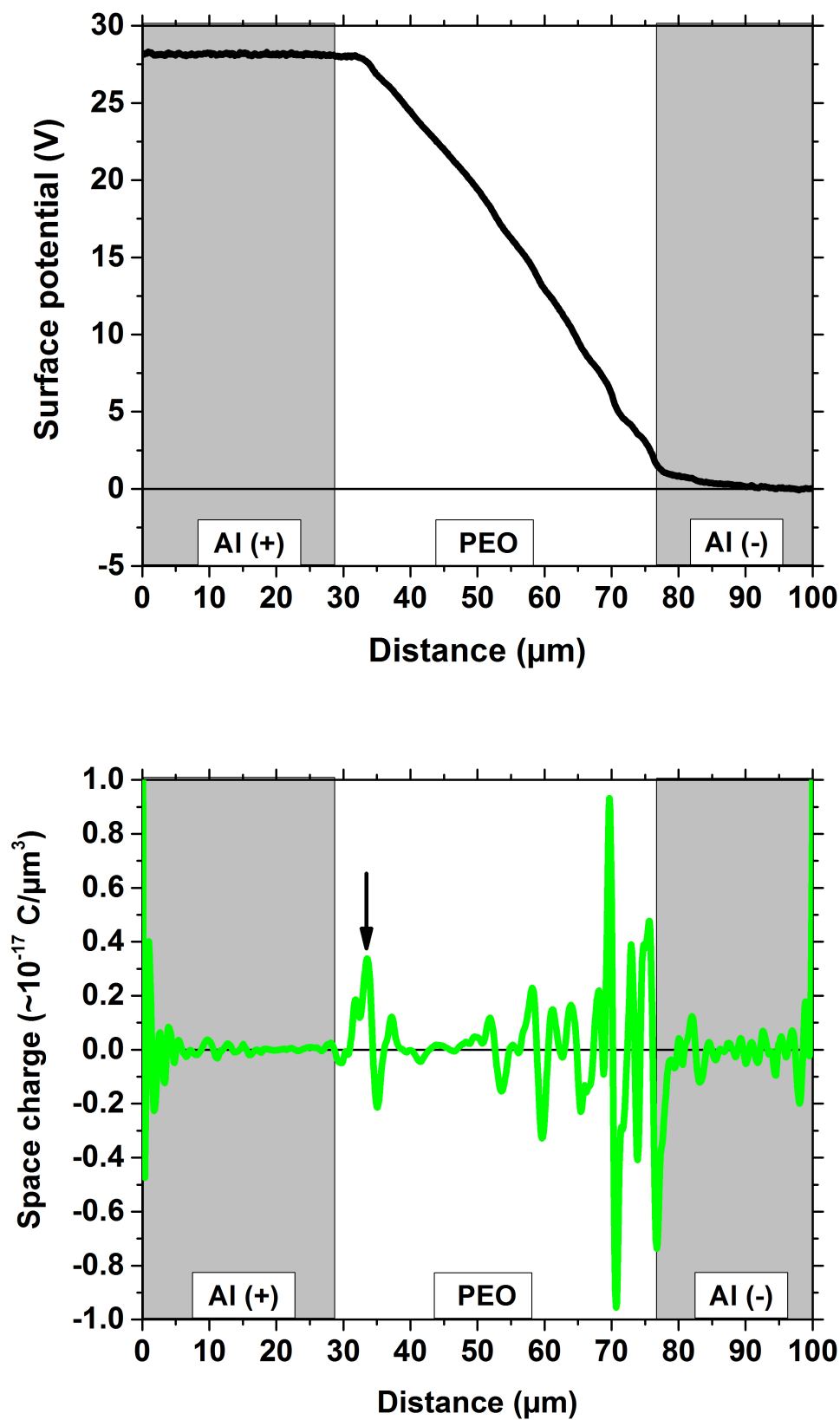
Figure 7.2: Surface potential and space charge distribution for the undoped PEO sample $10s$ after application of $28V$.
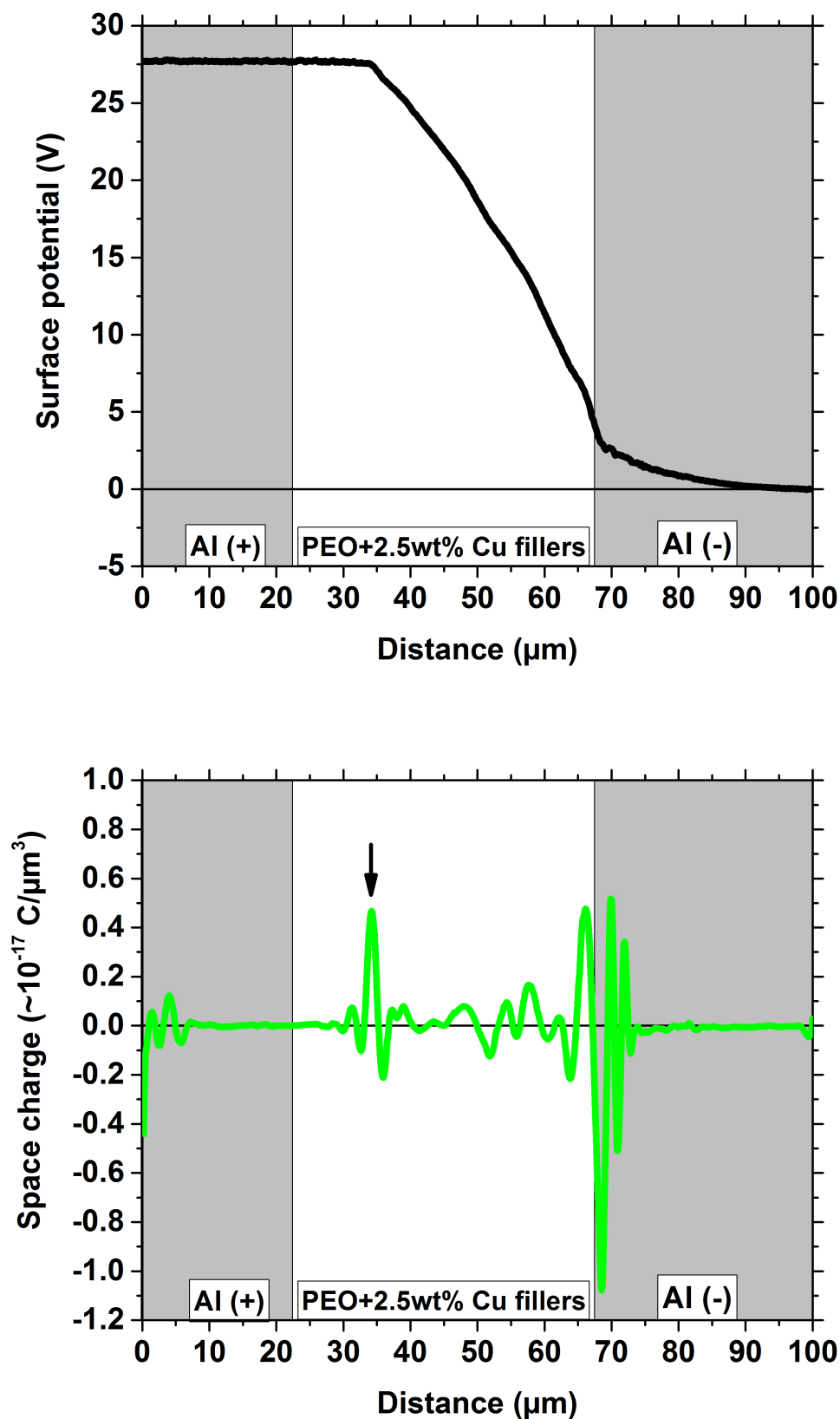
Figure 7.3: Surface potential and space charge distribution for the PEO sample embedded with $2.5wt\%$ Cu particles $10s$ after application of $28V$.
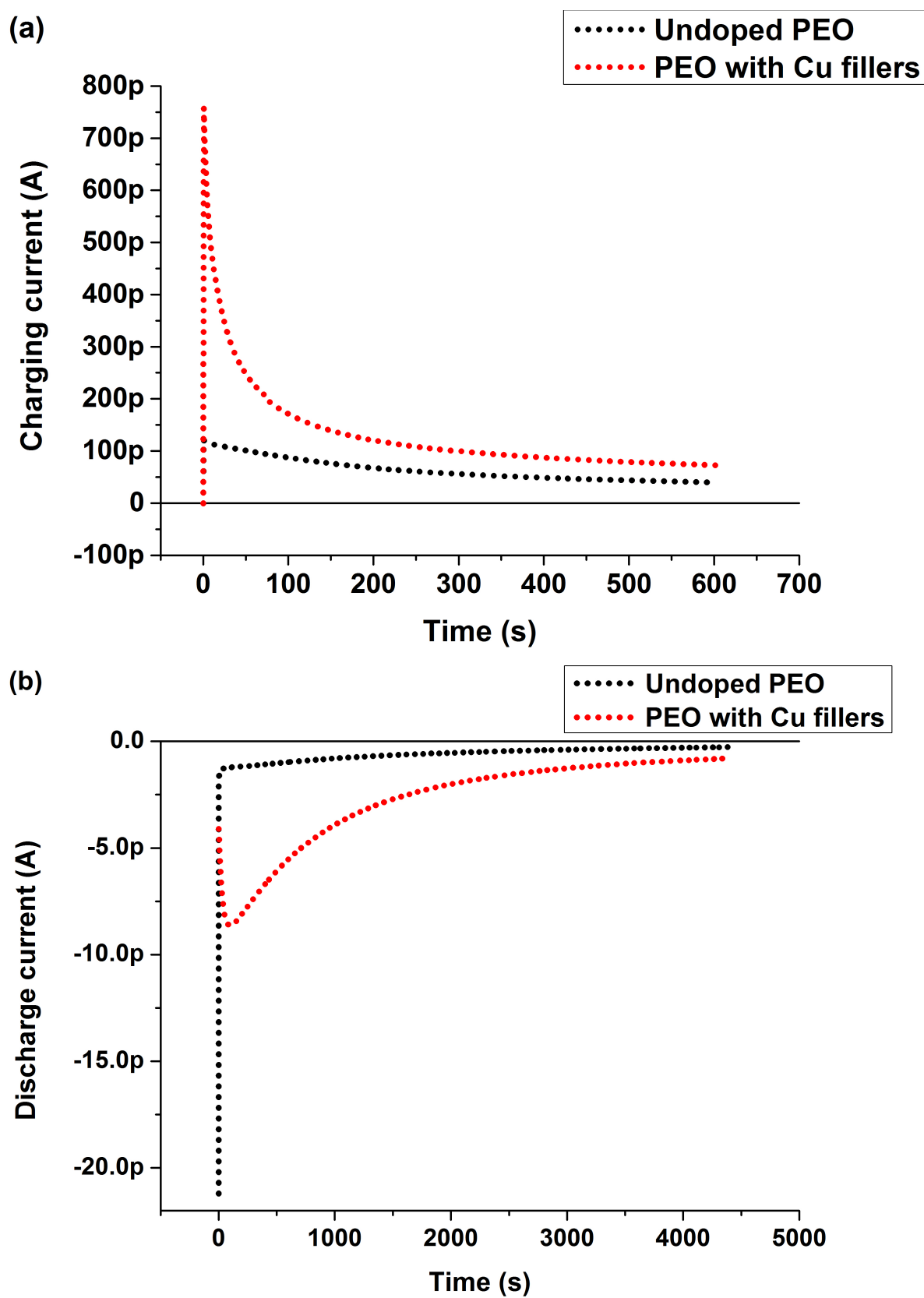
Figure 7.4: Charge and discharge current in undoped PEO and Cu filled PEO samples.

Chapter 8

Zero field point

A zero field point is a point in a space inside the material where an internal electrical field is zero. As our approach is based on the measurement of a surface potential distribution ($\phi(x)$) in a material by the KPFM, an electric field distribution ($E(x)$) can be calculated from Poisson's equation as follows.

$$E(x) = -\frac{d\phi(x)}{dx} \tag{8.1}$$

J. Lindmayer [33] suggested that when there is an injection of only one type of charge carriers (i.e. electron injection) in an insulating material during a biased condition, then it follows the relation shown in Equation 8.2. That is: an outer circuit discharge current density (J) is proportional to the charge density (ρ) at the zero field point and to the velocity of the zero field point (ν) inside the insulator.

$$J \propto \rho \cdot \nu \tag{8.2}$$

Equation 8.2 is valid for the case of an injection of only one type charge carriers because in this case the zero field point is well defined. But things get complicated when there is an injection of two types of charge carriers involved. In this case, the zero field point is not very well defined and depends on the balance between the two type of carries [33]. In our case, we used the Al-PEO-Al sample as an investigating model system. That is why, it is even more complicated because not only two type of charge carriers but also the internal charge movement is involved. One needs an exact charge distribution in order to detect the zero field point position. This can be checked with our method since it can give the exact charge distribution as well as the electric field distribution from the measured surface potential by the KPFM.

In our experiment, we used the Al-PEO-Al sample with the type 1 structure shown in Fig. 3.3. At first, we measured the surface potential distribution of the sample in its equilibrium state without any external field applied. From the measured data of the surface potential distribution, we calculated the electric field and space charge distribution using our algorithm described in Chapter 5. After that, we applied an external voltage for a certain amount of time so that the

charge injection can take place in the PEO sample. Here, one thing to be noted is that, the undoped PEO behaves as an ionic conductor. After the application of voltage, we measured again the surface potential distribution and calculated the electric field and the space charge distribution.

8.1 Condition before a voltage applied

Fig. 8.1 shows an initial equilibrium state of the PEO sample. From the surface potential (Fig. 8.1(a)), the charge distribution (Fig. 8.1(b)) and the electric field distribution (Fig. 8.1(c)) are calculated according to the Equations 5.1 and 8.1 respectively. As expected, we can see the positive charges accumulated in the PEO at the PEO/Al interface regions due to the image forces in the electrodes. Due to this positive charge accumulation, we can see also induced negative charges in the Al electrodes at the PEO/Al interface regions. Charge oscillations can be seen in the PEO. In the equilibrium state, the internal charges in the PEO are distributed in such a way that we have detected a well defined zero field point marked with a blue arrow in Fig. 8.1(c).

8.2 Condition after a voltage applied

To investigate the behaviour of the zero field point after application of an external voltage, we applied $300V$ to the sample for $10min$. The charge injection takes place during application of the voltage. We have chosen a maximum limit of $300V$ of our voltage source to apply on the sample. After application of the voltage for $10min$, we switched off the voltage and measured the transient formation of the surface potential distribution of the sample in the short-circuit condition. The surface potential profiles measured at different moments in time after removal of the applied voltage of $300V$ are shown in Fig. 8.2. Our AFM system can only measure a potential only up to $30V$. Therefore, we are unable to measure the potential profile during the application of $300V$. Fig. 8.2 shows the surface potential distribution profiles at $26s$, $36s$, $126s$, $306s$, $1006s$ and $10256s$ after the applied voltage switched off.

After switching off the applied voltage, the internal charges of the PEO and the injected charges in the PEO redistribute in order to achieve again the equilibrium state of the material. Different patterns of the surface potential at the different moments in time indicate the movement of the internal charges and the injected charges in the PEO. $10256s$ after the applied voltage switched off, we see the surface potential at the same height as it was before application of the voltage (See Fig. 8.2). This indicates that the sample has again achieved its equilibrium state.

To get a clear visualization of the movement of the internal charges and the injected charges in the PEO, the charge distributions are calculated from the surface potential data at the different moments in time. Fig. 8.3 shows the charge distribution in the PEO at the different moments in time. To analyse these charge distribution patterns in detail, we look at the results separately in three different parts: the charges near the Al/PEO interface region (on the left side) where the Al electrode was positive during application of the voltage, the charges in the PEO region (in the middle) and the charges near the Al/PEO interface region (on the right side) where the Al electrode was negative during application of the voltage. Fig. 8.4(a) shows the charge distribution at the left side around the Al/PEO interface region, Fig. 8.4(b) shows the charge

Figure 8.1: Surface potential (a), space charge (b) and electric field distribution (c) of the undoped PEO sample under short-circuited condition before voltage application.

distribution in the middle in the PEO and Fig. 8.4(c) shows the charge distribution at the right side around the Al/PEO interface region.
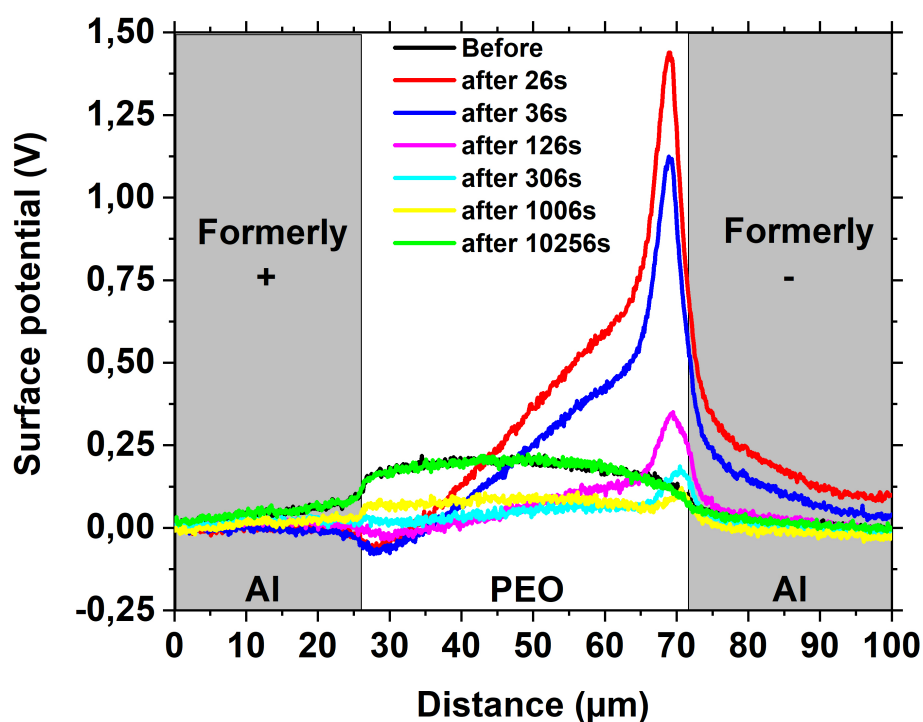
Figure 8.2: Surface potential distribution of the undoped PEO sample under short-circuited condition after application of $300V$ for $10min$.
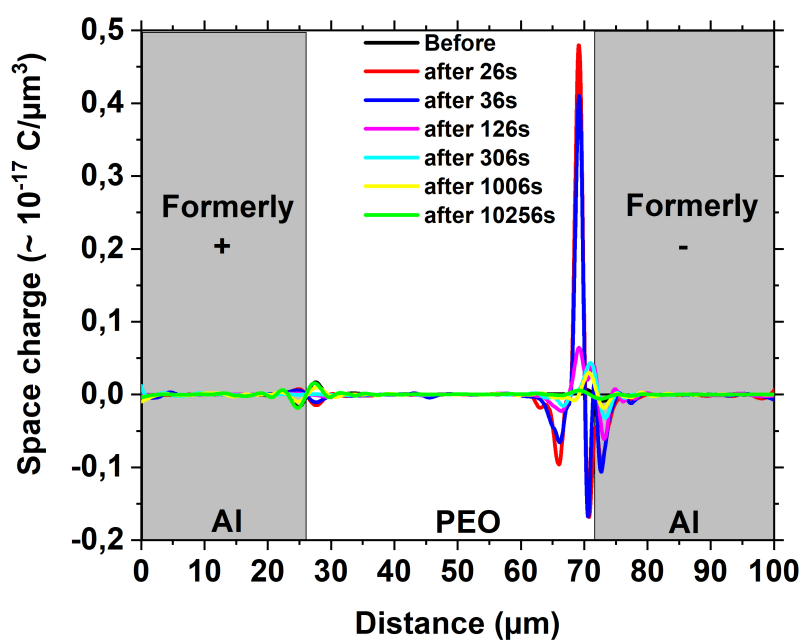
Figure 8.3: Space charge distribution in the undoped PEO sample under the short-circuited condition after application of $300V$ for $10min$.
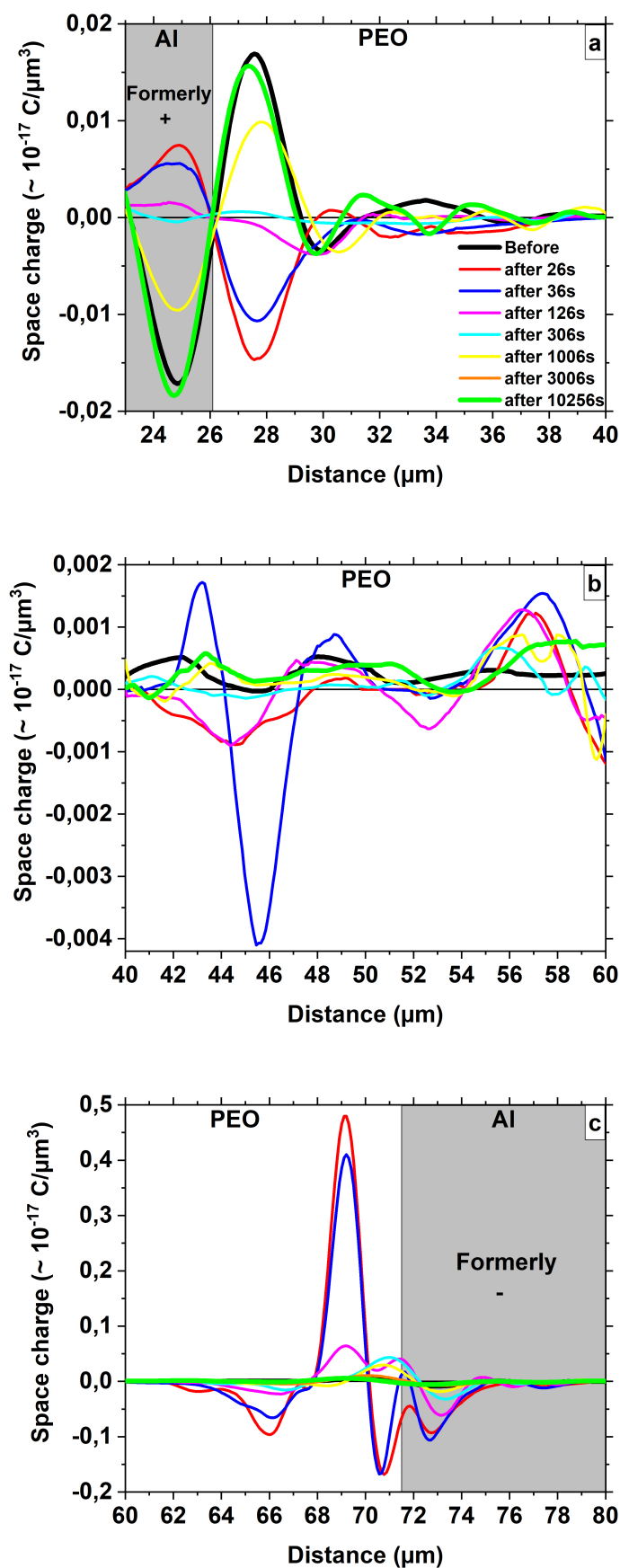
Figure 8.4: Space charge distribution at the Al/PEO interface region on the left side (a), in the middle (b) and at the Al/PEO interface region on the right side (c) in the undoped PEO sample under the short-circuited condition after application of $300V$ for $10min$.

On the right side, where the Al electrode was formerly negative during application of the voltage, we find a peak of positive charges (see Fig. 8.4(c)). These charges are decreasing in time. The positive charges accumulated at the Al/PEO interface region on the right side have traveled towards the formerly negative Al electrode during the voltage was applied. After removal of the voltage, these charges are redistributing themselves into the volume of the PEO. That is why, we see a decay of the positive peak with time at the interface region on the right side. At the same time, we have detected negative charges injected from the electrode which was negative during the voltage application (see Fig. 8.4(c)). The injected charges (i.e. electrons) have a higher mobility than the internal charges (i.e ions) in the PEO. $36s$ after the removal of the applied voltage, these injected charges have already left because of their higher mobility than the ion's mobility. On the left side of the positive peak, we have detected a negative peak which is seen to be decreasing slowly in time (see Fig. 8.4(c)). This decaying negative peak can be referred to the accumulation of the internal negative charges which are also redistributing themselves into the volume of the PEO in time after removal of the voltage.

On the left side, where the Al electrode was formerly positive during application of the voltage, we find a peak of negative charges (see Fig. 8.4(a)). These negative charges can be referred to the internal negative charges of the PEO which have traveled towards the formerly positive Al electrode during the voltage was applied. These gathered negative charges at the electrode on the left side diffuse back in the volume of the PEO in time and leave behind positive immobile charges. At the same time, one can see the induced positive image charges in the Al on the left side. They decrease in time and finally turn into negative charges. $10256s$ after switching off the applied voltage, we see that the peak of the positive immobile charges has attained nearly the same height as the height of the peak of the positive immobile charges detected before application of the voltage (see Fig. 8.4(a)). This indicates that the system has attained its equilibrium state. In the volume of the PEO sample, we see the charge oscillations (see Fig. 8.4(b)). These oscillations are reduced in time due to a transient redistribution of the internal charges and the injected charges in the volume of the PEO sample.

As we have now the exact charge distributions, we can investigate the electric field distribution and the zero field point in the material at the different moments in time. Fig. 8.5 shows the electric field distribution in the PEO at the different moments in time.

To get a clear picture about the zero field point, we look at the results separately in three parts in same way as we did for the result of charge distributions. The three parts of the result are divided as follows: the field distribution near the Al/PEO interface region (on the left side) where the Al electrode was positive during application of the voltage, the field in the PEO region (in the middle) and the electric filed near the Al/PEO interface region (on the right side) where the Al electrode was negative during application of the voltage. Fig. 8.6(a) shows the field distribution at the left side a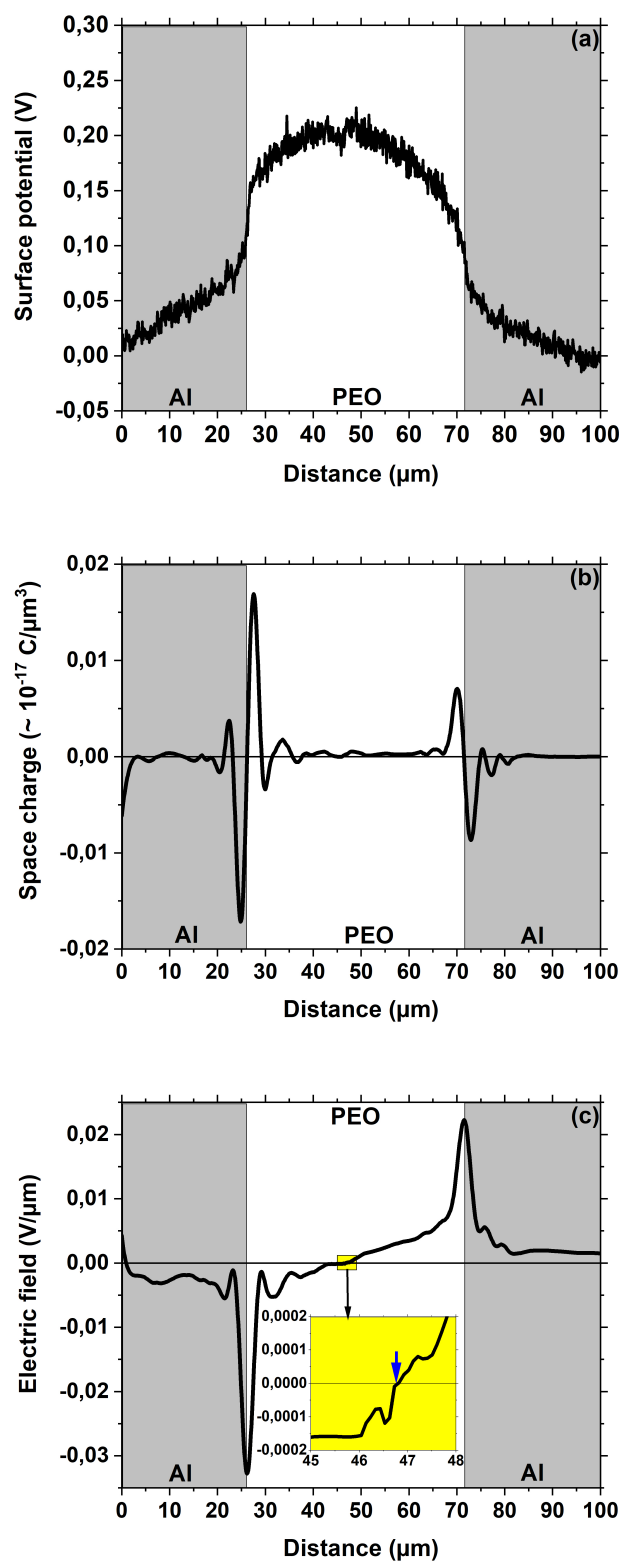round the Al/PEO interface region, Fig. 8.6(b) shows the field distribution in the middle in the PEO and Fig. 8.6(c) shows the field distribution at the right side around the Al/PEO interface region.

As mentioned earlier, there is only one well defined zero field point according to J. Lindmayer when an injection of one type of charge carriers takes place. He had also mentioned that the zero field point is not well defined when there is an injection of two types of charge carriers [33]. But in his study, he had not mentioned the effect of internal charges on the zero field point in insulators. In our experiment, we also consider that only one type of charge carriers
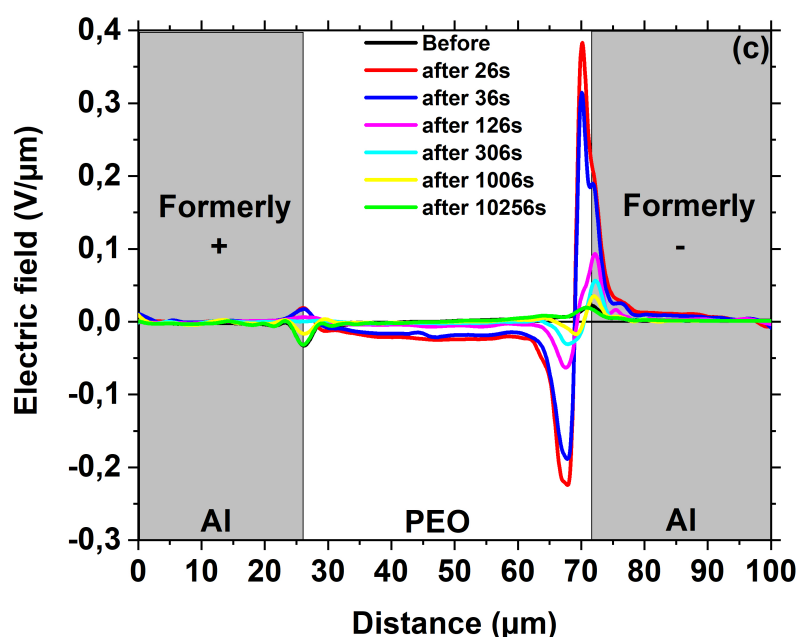
Figure 8.5: Electric field distribution in the undoped PEO sample under the short-circuited condition after application of $300V$ for $10min$.

(i.e electrons) are injected from the Al Electrode during the voltage applied. When we look at the electric field distribution after the applied voltage has been removed, we see many zero field points marked with arrows in Fig. 8.6(a), (b) and (c). These field points appear and disappear at different places in the PEO and the number of field points go up and down at the different moments in time.

Fig. 8.6(a), (b) and (c) shows the electric field distributions at $26s$ (red), $36s$ (blue), $126s$ (magenta), $360s$ (cyan), $1006s$ (yellow) and $10256s$ (green) after the applied voltage is switched off. $26s$ after the voltage switched off, we see a total two zero field points. One is at the left side near the Al/PEO interface region (see Fig. 8.6(a) (red)) and another one is at the right side near the Al/PEO interface region (see the enlarged part in Fig. 8.6(c) the red line, but it is covered by the blue line)). $36s$ after removal of the applied voltage, we still see two zero field points which we have observed at $26s$ but they are shifted a little bit to the right side (see the blue line in Fig. 8.6(a) and (c)). The shift of the zero field point observed at the region near the PEO/Al interface on the right side is not so big and that is why it is very difficult to show it in the enlarged part of Fig. 8.6(c) because of the scale. $126s$ after switching off the applied voltage, we still see two zero field points which have been observed before, at $26s$ and at $36s$. They have shifted even further on the right side (see the magenta line in Fig. 8.6(a) and (c)). Interestingly, $306s$ after the applied voltage switched off, the internal charges and the injected charges are distributed in such a way that we have detected a total of six zero field points. In Fig. 8.3(a) you can see one zero field point (see the cyan line), in Fig. 8.6(b) you see also one zero field point and in Fig. 8.6(c) you can see four zero field points. $1006s$ after removal of the applied voltage, we have detected five zero field points. In Fig. 8.6(a) one can see two zero field points (see the yellow line), in Fig. 8.6(b) one zero field point can been seen and in Fig. 8.6(c) you can see two zero field points. When the system reached to its equilibrium state $10256s$ after the applied voltage was switched off, the internal charges are distributed in such a
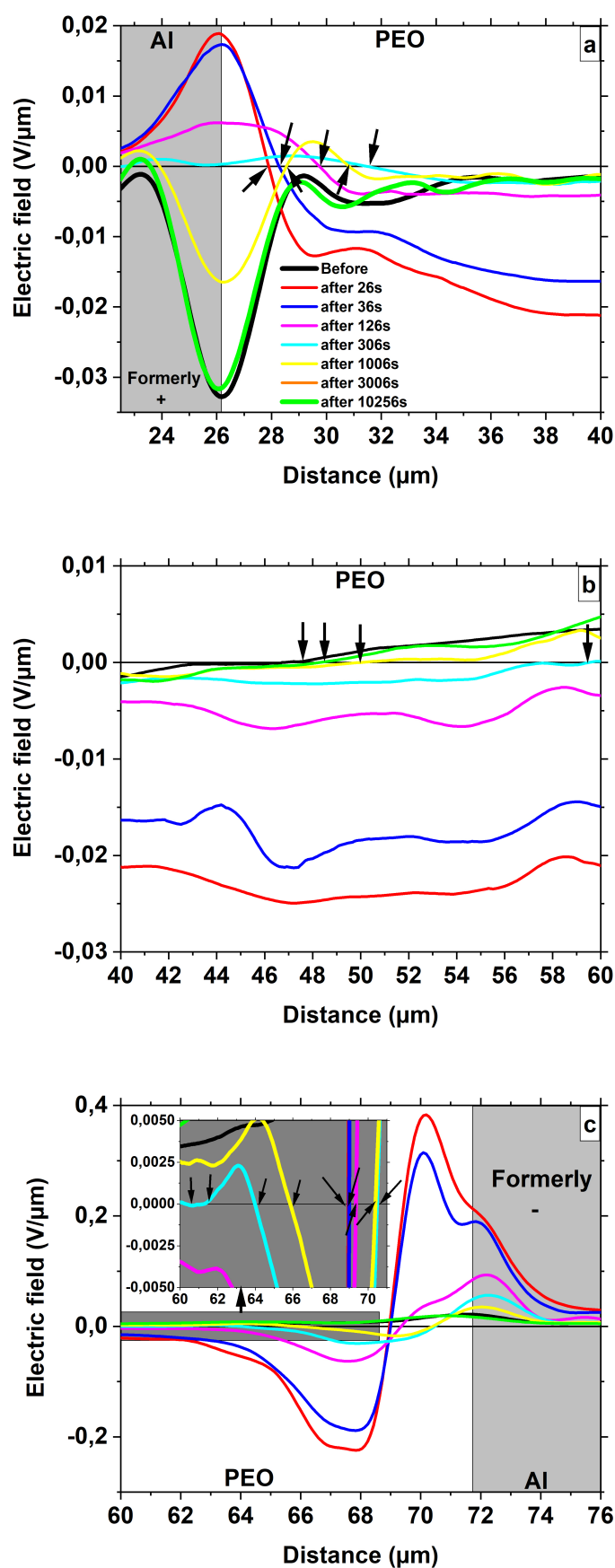
Figure 8.6: Electric field distribution at the Al/PEO interface region on the left side (a), in the middle (b) and at the Al/PEO interface region on the right side (c) in the undoped PEO sample under the short-circuited condition after application of $300V$ for $10min$.

way that we detected only one zero field point (see the gree line in Fig. 8.6(b)).

These multiple zero field points at the multiple locations in the material are resulted from the changing arrangement of internal charges and injected charges in the material. The multiple zero field points are obvious to be detected even if we consider the injection of only one type of charge carriers because the internal charges in the material can contain both types of charge carriers, positive and negative. Unfortunately, with this approach we can not differentiate between the internal charges and the injected charges by simply looking at the charge distribution patterns.

Chapter 9

Summary

9.1 Conclusion

The demand for electricity is increasing continuously, which is why more and more efforts are put in the development of highly efficient energy storage devices. Lithium-ion batteries (LIB) come first in this category. To develop efficient, cost-effective, safe and secure LIBs, one needs to understand physics of the materials used in LIBs. Out of the three basic material components of LIBs - materials for cathode, materials for anode and electrolytes materials - the role of electrolytes is more relevant than that of the other two, regarding safety issues such as leakage, flammability and stability during the use of LIBs. The use of solid polymer electrolytes (SPEs) is one of the possible solutions to resolve these safety issues. Poly(ethylene oxide) (PEO) with Li-salt complexes is intensively investigated for this purpose. As any other electrolytes, the ion conduction in SPEs (i.e. PEO+Li-salt) is the main focus point of investigation.

In this study, we have presented an approach which helps to give us a clear visualization of charge distribution in PEO with and without doping of $0.1wt\%$ lithium perchlorate ($LiClO_4$) under biased as well as unbiased conditions. This approach allows the possibility to visualize transient changes in the charge distribution under both biased and unbiased conditions. In this way, we can get more insight into the charge formation and the charge's movement inside the volume of the PEO and its salt compound. This insight ultimately helps to understand the ion conduction in SPEs. In this approach, we first measure the surface potential of undoped PEO samples as well as PEO samples doped with $LiClO_4$ under biased and unbiased conditions. To measure the surface potential we use the Kelvin probe force microscopy (KPFM) method. After that, from the measured surface potential we calculate the charge distribution in the sample by using the Poisson equation. The main problem when extracting the charge distribution from the surface potential data is the noise in the surface potential data. As the charge distribution is a second order derivative of the surface potential (see Equation 5.1) according to the Poisson equation, the calculation of the second order derivative of the noisy data increases the level of noise significantly.

For this reason, a smoothing operation on the noisy surface potential data is unavoidable. The smoothing-derivative algorithm developed in this study shows significantly better results in the calculation of the second order derivative of the noisy surface potential data. Our algorithm is based on the least square regression method. It is an extended version of the Savizky-Golay algorithm. The smoothing-derivative algorithm works in two parts. First, for the data

in a particular data point window, the algorithm finds the best polynomial fit function by using the F-test statistical approach to smooth the data. This constant data point window runs over the noisy data set and at each step the best fitting function is found. Then the second order derivative of these polynomial fit functions i.e. the space charge distribution according to Equation 5.1 is calculated. Data point windows with different lengths show different space charge distribution patterns for the given surface potential data. To choose the most reliable space charge distribution, an additional feedback loop is used in the algorithm. It recalculates the surface potentials from all different space charge distribution patterns by integrating them twice considering the boundary conditions. The minimum deviation, calculated by Equation 5.11, between the recalculated and measured surface potential is taken into consideration to choose the most reliable space charge distribution.

Due to the high resolution of the system, we are now able to detect oscillations in the surface potential. We have checked that the oscillations detected in the surface potential are not caused by the roughness of the sample surface. However, these oscillations in the surface potential lead us to observe for the first time local charge oscillations inside a solid polymer electrolyte. From the assumed charge oscillations and its calculated energy density it is concluded that local charge oscillations are propitious for the system in order to decrease the energy of the system even in equilibrium. The speed of the measurement system allows us to see the development and the motion of a positive charge packet starting at the positive electrode/electrolyte interface region during an application of voltage. The results reveal that the positive charge packet traveling towards the negative electrode has a higher speed in the PEO sample doped with $LiClO_4$ than the speed in the undoped PEO sample. This is possible because the doped PEO sample has more mobile positive charges (i.e. Li^+) compared to the undoped PEO sample. The speed of the positive charge packet in both types of samples is decreased during an application of voltage as time passes. This indicates that the electrical mobility of this positive charge packet in the both types of samples decreases during the application of voltage as time passes.

We have also seen that an increase of the applied voltage increases the charge oscillations as well as the amplitude of the positive charge packet. On the other hand, in an unbiased condition under the equilibrium state, the charge oscillations are significantly influenced by the electrodes. The results show that charge oscillations are stronger when the distance between the two electrodes is small. A charge injection phenomenon is detected at the negative electrode/electrolyte interface region where the transient formation of negative charges was observed in the biased condition. During the KPFM measurement, the lift-height of the cantilever-tip influences the potential measurement. The potential drop has been seen above the negative electrode. It becomes broader as the lift-height of the cantilever-tip is increased. The potential drop above and along the negative electrode is influenced not only by the lift-height of the cantilever-tip but also by the charges inside the material. In the doped sample, the potential drop is increasing significantly with time in the biased condition compared to the undoped sample for the same conditions.

In this study, we have also investigated for the first time the effect of micro/nano-sized metal particles in solid polymer electrolytes (SPEs). The results indicate a significant influence of metal particles on the charge distribution inside SPEs as well as the conductivity of SPEs. By looking at the charge distribution of the pure PEO samples and the PEO samples embedded with Cu particles, it is seen that the charge oscillations are significantly decreased in the PEO samples with added Cu particles in comparison to the oscillations detected in the pure PEO

samples. The speed of the positive charge packet in the Cu filled PEO samples is seen to be higher than it is in the pure PEO samples. This shows that the mobility of charges inside the PEO samples filled with Cu particles increases as compared to the mobility of charges in the pure PEO samples. This indicates an improvement in the conductivity of PEO with the help of Cu particles. The improvement in the conductivity can be concluded from the current measurement as well. The results of the current measurement shows that the flow of current is higher in the PEO with Cu fillers than in the pure PEO.

From the surface potential distribution of the PEO sample, the electric field distribution can be calculated (see Equation 8.1). With the help of this approach, we have investigated the behavior and formation of a zero field point inside the PEO sample. We found that the zero field point is influenced not only by injected charge carriers but also by internal charges inside the PEO material. In equilibrium state of the PEO, we have seen that the internal charges of the PEO are distributed in such a way that we have detected a single zero field point. After application of an external field, the injected charges and the internal charges inside the PEO redistribute themselves continuously until the system achieves the equilibrium state again. During this process of redistribution of the internal and injected charges, we have detected many zero field points. These zero field points appear and disappear in time as the redistribution process of the charges continues towards the equilibrium state.

9.2   Suggestions for future research

The ion conduction mechanism in SPEs is still not fully understood. During our study, we have detected for the first time charge oscillations and moving charge packets inside SPEs with our proposed experimental method. To advance the understanding of ion transport in SPEs and to investigate the role of charge oscillations and charge packets as well as the injection of electrons in the ion conduction process, we can consider establishing a discrete microscopic model. With the help of a discrete microscopic model, we can investigate whether charge oscillations and charge packets can be caused solely by charge interaction and thermal movement of charges without taking into account the molecular structure of the material. As a discrete microscopic model, the three-dimensional hopping model presented earlier [20] can be considered and improved. In the earlier version, the movement of ions in SPEs is illustrated by a hopping in a multiwell energy structure. In that model, only negative charges can move over the energy barriers to neighboring cells. The charge neutrality is provided by introducing immobile positive background charges. Charge oscillations and moving positive charge packets might be explained if we consider that both positive and negative ions can move with different mobility in the energy structure.

The role of micro/nano-sized metal particles for the conductivity improvement of SPEs and the formation of charge oscillations and the movement of charge packets in SPEs can be evaluated further. The evaluation can be done by comparing the results of current measurements, surface potential measurements and extraction of charge distributions of SPEs embedded with different metal particles (i.e. Cu, Ag) with different concentrations. The evaluation can be done further by comparing the results of SPE samples with different combinations, for example: pure PEO samples, PEO samples with embedded metal (i.e. Cu) and/or ceramic (i.e. SiO_2) nano/micro particles with different concentrations, PEO samples doped with different

concentration of Li-salt (i.e. $LiClO_4$) and Li-doped PEO samples with embedded metal and/or ceramic nano/micro particles with different concentrations. Additionally, the evaluation of the surface potential distribution around these micro/nano particles can also reveal some new information about the effect of these particles. Furthermore, to understand the effect of metal particles on the improvement of conductivity of SPEs, the development of a reliable and effective simulation model based on the three-dimensional hopping model can also provide an interesting topic of research.

In addition to this, the limits in terms of space and charge resolution of the technique described in this study should be explored.

References

[1] Eva Nevelius. Press release: The nobel prize in chemistry 2019. www.nobelprize.org, 09 2019.

[2] Stanley Whittingham. Electrical energy storage and intercalation chemistry. *Science*, 192(4244):1126–1127, 1976.

[3] K. Mizushima, P.C. Jones, P.J. Wiseman, and J.B. Goodenough. Lixcoo2 $(0 < x - l)$: A new cathode material for batteries of high energy density. *Materials Research Bulletin*, 15(6):783–789, 1980.

[4] Akira Yoshino, Kenichi Sanechika, and Takayuki Nakajima. Secondary battery. US patent: $4, 668, 595$, 05 1987.

[5] Zhigang Xue, Dan He, and Xiaolin Xie. Poly(ethylene oxide)-based electrolytes for lithium-ion batteries. *J. Mater. Chem. A*, 3:19218–19253, 2015.

[6] Elahe Talaie, Patrick Bonnick, Xiaoqi Sun, Quan Pang, Xiao Liang, and Linda F. Nazar. Methods and protocols for electrochemical energy storage materials research. *Chemistry of Materials*, 29(1):90–105, 2017.

[7] Peter V. Wright. Electrical conductivity in ionic complexes of poly(ethylene oxide). *British Polymer Journal*, 7(5):319–327, 1975.

[8] Michel Armand. Polymer solid electrolytes - an overview. *Solid State Ionics*, 9(Part 2):745 – 754, 1983.

[9] C. Berthier, W. Gorecki, M. Minier, M.B. Armand, J.M. Chabagno, and P. Rigaud. Microscopic investigation of ionic conductivity in alkali metal salts-poly(ethylene oxide) adducts. *Solid State Ionics*, 11:91–95, 1983.

[10] Zlatka Gadjourova, Yuri G. Andreev, David P. Tunstall, and Peter G. Bruce. Ionic conductivity in crystalline polymer electrolytes. *Nature*, 412:520–523, 2001.

[11] M. A. Ratner, P. Johansson, and D. F. Shriver. Polymer electrolytes: Ionic transport mechanisms and relaxation coupling. *MRS Bulletin*, 25(3):31–37, 2000.

[12] R C Agrawal and G P Pandey. Solid polymer electrolytes: materials designing and all-solid-state battery applications: an overview. *Journal of Physics D: Applied Physics*, 41:223001, 2008.

[13] A. Wagner and H. Kliem. Dispersive ionic space charge relaxation in solid polymer electrolytes ii: Model and simulation. *Journal of Applied Physics*, 91:6638, 2002.

[14] B. Martin and H. Kliem. Electrode effects in solid electrolyte capacitors. *Journal of Applied Physics*, 98:074102, 2005.

[15] B. Skinner, M. S. Loth, and B. I. Shklovskii. Capacitance of the double layer formed at the metal/ionic-conductor interface: How large can it be ? *JPhysics review letters*, 104:128302, 2010.

[16] J. R. Macdonald. Utility of continuum diffusion models for analyzing mobile-ion immittance data: electrode polarization, bulk and generation-recombination effects. *Journal of Physics C: Condens Matter*, 22:495101, 2010.

[17] J. R. Macdonald. Effects of various boundary conditions on the response of poisson-nernst-plank impedance spectroscopy analysis models and comparison with a continuous-time random-walk model. *Journal of Physical Chemistry A*, 115:13370, 2011.

[18] A. Wagner and H. Kliem. Dispersive ionic space charge relaxation in solid polymer electrolytes i: Experimental system polyethylene oxide. *Journal of Applied Physics*, 91:6630, 2002.

[19] Bjoern Martin and Herbert Kliem. Space charge measurements with the scanning kelvin probe. *IEEE Transactions on Dielectrics and Electrical Insulation*, 15(2):560–567, April 2008.

[20] Bjoern Martin and Herbert Kliem. Internal fields in solid electrolytes due to interface effects. *Applied Physics Letters*, 95(3), 2009.

[21] Bjoern Martin and Herbert Kliem. Space charges in solid electrolytes detected by the scanning kelvin probe. *Journal of Non-Crystalline Solids*, 356(11–17):701 – 704, 2010.

[22] Bjoern Martin and Herbert Kliem. Sample length independent conduction current in polyethylene oxide. *Journal of Applied Physics*, 113:034101, 2013.

[23] Bjoern Martin and Herbert Kliem. Strange discharge current transients in polyethylene oxide. *IEEE Transactions on Dielectrics and Electrical Insulation*, 22:509, 2015.

[24] Bjoern Martin and Herbert Kliem. Non-exponential kohlrausch polarization currents in solid electrolytes. *IEEE Transactions on Dielectrics and Electrical Insulation*, 22:503, 2015.

[25] M. Watanabe, K. Sanui, N. Ogata, T. Kobayashi, and Z. Ontaki. Ionic conductivity and mobility in network polymers from poly (propylene oxide) containing lithium perchlorate. *The Journal of Applied Physics*, 57:123, 1985.

[26] J Evans, C. A. Vincent, and P. G. Bruce. Electrochemical measurement of transference numbers in polymer electrolytes. *Polymer*, 28:2324, 1987.

[27] F. Croce, G. B. Appetecchi, L. Persi, and B. Scrosati. Nanocomposite polymer electrolytes for lithium batteries. *Nature*, 394:456–458, 1998.

[28] L. M. Bronstein, R. J. Karlinsey, K. Ritter, C. G. Joo, B. Stein, and J. W. Zwanziger. Design of organic-inorganic solid polymer electrolytes: synthesis, structure and properties. *Journal of Materials Chemistry*, 14:1812–1820, 2004.

[29] G. B. Appetecchi, S. Scaccia, and S. Passerini. Investigation on the stability of the lithium-polymer electrolyte interface. *Journal of The Electrochemical Society*, 147:4448–4452, 2000.

[30] T. Itoh, Y. Miyamura, Y. Ichikawa, T. Uno, M. Kubo, and O. J. Yamanoto. Composite polymer electrolytes of poly(ethylene oxide)/batio3/li-salt with hyperbranched polymer. *Journal of Power Sources*, 119:403–408, 2003.

[31] Z. H. Li, H. P. Zhanga, P. Zhanga, Y. P. Wua, and X. D. Zhou. Macroporous nanocomposite polymer electrolyte for lithium-ion batteries. *Journal of Power Sources*, 184:562–556, 2008.

[32] K. Karuppasamy, R. Antony, S. Alwin, S. Balakumar, and X. S. Shajan. A review on peo based solid polymer electrolytes (spes) complexed with lix (x=tf, bob) for rechargeable lithium ion batteries. *Materials Science Forum*, 807:41–63, 2015.

[33] Joseph Lindmayer. Current transients in insulators. *Journal of Applied Physics*, 36(1), 1965.

[34] CA Rezende, RF Gouveia, MA Da Silva, and F Galembeck. Detection of charge distributions in insulator surfaces. *Journal of Physics: Condensed Matter*, 21(26):263002, 2009.

[35] C. Villeneuve-Faure, L. Boudou, K. Makasheva, and G. Teyssedre. Methodology for extraction of space charge density profiles at nanoscale from kelvin probe force microscopy measurements. *Nanotechnology*, 28:505701, 2017.

[36] F Mortreuil, C Villeneuve-Faure, L Boudou, K Makasheva, and G Teyssedre. Charge injection phenomena at the metal/dielectric interface investigated by kelvin probe force microscopy. *Journal of Physics D: Applied Physics*, 50(17):175302, 2017.

[37] Ulrich Zerweck, Christian Loppacher, Tobias Otto, Stefan Grafström, and Lukas M Eng. Accuracy and resolution limits of kelvin probe force microscopy. *Physical Review B*, 71(12):125424, 2005.

[38] Liming Liu and Guangyong Li. Electrical characterization of single-walled carbon nanotubes in organic solar cells by kelvin probe force microscopy. *Applied Physics Letters*, 96(8):3302, 2010.

[39] T Hallam, C M Duffy, T Minakata, M Ando, and H Sirringhaus. A scanning kelvin probe study of charge trapping in zone-cast pentacene thin film transistors. *Nanotechnology*, 20(2):5203, 2008.

[40] H. Hoppe, T. Glatzel, M. Niggemann, A. Hinsch, M. Ch. Lux-Steiner, and N. S. Sariciftci. Kelvin probe force microscopy study on conjugated polymer/fullerene bulk heterojunction organic solar cells. *Nano Letters*, 5(2):269–274, 2005.

[41] Nathan G. Clack, Khalid Salaita, and Jay T. Groves. Electrostatic readout of dna microarrays with charged microspheres. *Nature Biotechnology*, 26:825–830, 2008.

[42] Eric Finot, Yuri Leonenko, Brad Moores, Lukas Eng, Matthias Amrein, and Zoya Leonenko. Effect of cholesterol on electrostatics in lipid-protein films of a pulmonary surfactant. *Langmuir*, 26(3):1929–1935, 2010.

[43] Lord Kelvin. Contact electricity of metals. *Philosophical Magazine series 5*, 46(278):82–120, 1898.

[44] W. A. Zisman. A new method of measuring contact potential differences in metals. *Review of Scientific Instruments*, 3:367–370, 1932.

[45] M. Nonnenmacher, M. P. O'Boley, and H. K. Wickramasinghe. Kelvin probe force microscopy. *Applied Physics Letters*, 58(25):2921–2923, 1991.

[46] *Veeco diInnova-User Manual*.

[47] Fiona Mary Gray. *Solid Polymer Electroytes: Fundamentals and Technological Applications*. Wiley-VCH, Weinheim, 1991.

[48] Rubia F Gouveia, Carlos AR Costa, and Fernando Galembeck. Water vapor adsorption effect on silica surface electrostatic patterning. *The Journal of Physical Chemistry C*, 112(44):17193–17199, 2008.

[49] K. Faliya and H. Kliem. Charge distributions in poly(ethylene oxide)-based electrolytes for lithium-ion batteries. *Electrochimica Acta*, 290:211–219, November 2018.

[50] S. Sadewasser, C. Leendertz, F. Streicher, and M. Ch. Lux-Steiner. The influence of surface topography on kelvin probe force microscopy. *Nanotechnology*, 20:505503, 2009.

[51] K. Faliya, H. Kliem, and C. J. Dias. Investigations of space charge distributions by atomic force microscope. In *2016 IEEE International Conference on Dielectrics (ICD)*, pages 219–222, July 2016.

[52] K. Faliya, H. Kliem, and C. J. Dias. Space charge measurements with kelvin probe force microscopy. *IEEE Transactions on Dielectrics and Electrical Insulation*, 24(3):1913–1922, June 2017.

[53] Abraham Savitzky and M. J. E. Golay. Smoothing and differentiation of data by simplified least squares procedures. *Analytical Chemistry*, 36(8):1627–1639, 1964.

[54] Phillip Barak. Smoothing and differentiation by an adaptive-degree polynomial filter. *Analytical Chemistry*, 67(17):2758–2762, 1995.

[55] C. G. Enke and Timothy A. Nieman. Signal-to-noise ratio enhancement by least-squares polynomial smoothing. *Analytical Chemistry*, 48(8):705A–712A, 1976.

[56] G. R. Phillips and Joel M. Harris. Polynomial filters for data sets with outlying or missing observations: application to charge-coupled-device-detected raman spectra contaminated by cosmic rays. *Analytical Chemistry*, 62(21):2351–2357, 1990.

[57] R. A. Fisher. *Statistical Methods for Research Workers*. London:Oliver and Boyd Ltd., 10th edition, 1948.

[58] Philip R. Bevington and D. Keith Robinson. *Data Reduction and Error Analysis for the Physical Sciences*, chapter 11. The McGraw-Hill Companises, Inc., New york, 1969.

[59] Emerson M. Pugh and George H. Winslow. *The ananlysis of physical measurments*, chapter 12. Addison-Wesley, 1966.

[60] J. Neyman and E. S. Pearson. The testing of statistical hypotheses in relation to probabilities a priori. *Mathematical Proc. Cambridge Philosophical Soc.*, 29(4):492–510, 1933.

[61] Maxim V. Fedorov and Alexei A. Kornyshev. Towards understanding the structure and capacitance of electrical double layer in ionic liquids. *Electrochimica Acta*, 53(23):6835 – 6840, 2008.

[62] Hongduo Lu, Sture Nordholm, Clifford E. Woodward, and Jan Forsman. Ionic liquid interface at an electrode: simulations of electrochemical properties using an asymmetric restricted primitive model. *Journal of Physics: Condensed Matter*, 30:074004, 2018.

[63] K. Faliya and H. Kliem. Dynamic space charge oscillations and charge packets in poly(ethylene oxide). In *2019 IEEE Conference on Electrical Insulation and Dielectric Phenomena (CEIDP)*, pages 789–792, October 2019.

[64] K. Faliya and H. Kliem. Space charges in metal-solid electrolyte-metal structures. In *2018 IEEE 2nd International Conference on Dielectrics (ICD)*, pages 1–4, July 2018.

[65] Bjoern Martin and Herbert Kliem. Effects of interacting ionic and electronic space charges. In *2014 IEEE Conference on Electrical Insulation and Dielectric Phenomena (CEIDP)*, pages 891–894, October 2014.

[66] J. E. Weston and B. C. H. Steele. Effects of inert fillers on the mechanical and electrochemical properties of lithium salt-poly(ethylene oxide) polymer electrolytes. *Solide State Ionics*, 7:75–79, 1982.

[67] S. Jung, D. W. Kim, S. D. Lee, M. Cheong, D. Q. Nguyen, B. W. Cho, and H. S. Kim. Fillers for solide-state polymer electrolytes: Highlight. *Bulletin of the Korean Chemical Society*, 30:2355–2361, 2009.

[68] J. W. Park, E. D. Jeong, M. S. Won, and Y. B. Shim. Effect of organic acids and nano-sized ceramic doing on peo-based solid polymer electrolytes. *Journal of Power Sources*, 160:674–680, 2006.

[69] K. S. Ji, H. S. Moon, J. W. Kim, and J.W. Park. Role of functional nano-sized inorganic fillers in poly(ethylene) oxide-based polymer electrolytes. *Journal of Power Sources*, 117:124–130, 2003.

[70] J. Xi, X. Ma, M. Cui, X. Huang, Z. Zheng, and X. Tang. Electrochemistry study on peo-licio4-zsm5 composite polymer electrolyte. *Chinese Science Bulletin*, 49:785–789, 2004.

[71] D. Shanmukaraj and R. Murugan. Characterization of peg: Licio4+srbi4ti4o15 nanocomposite polymer electrolytes for lithium secondary batteries. *Journal of Power Sources*, 149:90–95, 2005.

[72] J. Xi and X. Tang. Nanocomposite polymer electrolyte based on poly(ethylene oxide) and solid super acid for lithium polymer battery. *Chemical Physics Letters*, 393:271–276, 2004.

[73] Q. Li, N. Imanishi, Y. Takeda, A. Hirano, and O. Yamamoto. Peo-based composite lithium polymer electrolyte, peo-batio3-li(c2f5so2)2n. *Ionics*, 8:79–84, 2002.

[74] G. B. Appetecchi and S. Passerini. Peo-carbon composite lithium polymer electrolyte. *Electrochimica Acta*, 45:2139–2145, 2000.

[75] M. A. S. Azizi Samir, F. Alloin, W. Gorecki, J. Y. Sanchez, and A. Dufresne. Nanocomposite polymer electrolytes based on poly(oxyethylene) and cellulose nanocrystals. *Journal of Physical Chemistry B*, 108:10845–10852, 2004.

[76] E. Quartarone, P. Mustarelli, and A. Magistris. Peo-based composite polymer electroytes. *Solid State Ionics*, 110:1–14, 1998.

[77] A. M. Stephan and K. S. Nahm. Review on composite polymer electrolytes for lithium batteries. *Polymer*, 47:5952–5964, 2006.

[78] L. Yue, J. Ma, J. Zhang, J. Zhao, S. Dong, Z. Liu, G. Cui, and L. Chen. All solid-state polymer electrolytes for high-performance lithium ion batteries. *Energy storage materials*, 5:139–164, 2016.

[79] A. Dey, S. Karan, and S. K. De. Effect of nanoadditives on ionic conductivity of solid polymer electrolyte. *Indian Journal of Pure and Applied Physics*, 51:281–288, 2013.

[80] Penghui Yao, Haobin Yu, Zhiyu Ding, Yanchen Liu, Juan Lu, Marino Lavorgna, Junwei Wu, and Xingjun Liu. Review on polymer-based composite electrolytes for lithium batteries. *Frontiers in Chemistry*, 7:522, 2019.